

INFORMATION TO USERS

This manuscript has been reproduced from the microfilm master. UMI films the text directly from the original or copy submitted. Thus, some thesis and dissertation copies are in typewriter face, while others may be from any type of computer printer.

The quality of this reproduction is dependent upon the quality of the copy submitted. Broken or indistinct print, colored or poor quality illustrations and photographs, print bleedthrough, substandard margins, and improper alignment can adversely affect reproduction.

In the unlikely event that the author did not send UMI a complete manuscript and there are missing pages, these will be noted. Also, if unauthorized copyright material had to be removed, a note will indicate the deletion.

Oversize materials (e.g., maps, drawings, charts) are reproduced by sectioning the original, beginning at the upper left-hand corner and continuing from left to right in equal sections with small overlaps. Each original is also photographed in one exposure and is included in reduced form at the back of the book.

Photographs included in the original manuscript have been reproduced xerographically in this copy. Higher quality 6" x 9" black and white photographic prints are available for any photographs or illustrations appearing in this copy for an additional charge. Contact UMI directly to order.

UMI

A Bell & Howell Information Company
300 North Zeeb Road, Ann Arbor MI 48106-1346 USA
313/761-4700 800/521-0600

ENTROPIC ATTRACTIONS IN COLLOID-POLYMER SOLUTIONS

Ritu Verma

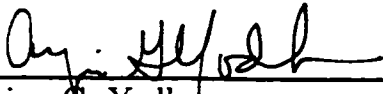
A DISSERTATION

in

PHYSICS AND ASTRONOMY

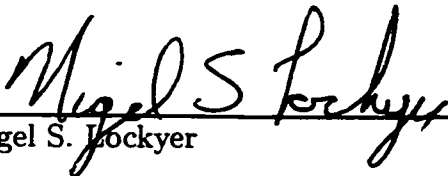
Presented to the Faculties of the University of Pennsylvania in Partial Fulfillment of
the Requirements for the Degree of Doctor of Philosophy

1999



Arjun G. Yodanis

Supervisor of Dissertation



Nigel S. Lockyer

Graduate Group Chairperson

UMI Number: 9926210

**Copyright 1999 by
Verma, Ritu**

All rights reserved.

**UMI Microform 9926210
Copyright 1999, by UMI Company. All rights reserved.**

**This microform edition is protected against unauthorized
copying under Title 17, United States Code.**

UMI
300 North Zeeb Road
Ann Arbor, MI 48103

COPYRIGHT

Ritu Verma

1999

to ma and pa

ACKNOWLEDGEMENTS

Throughout the course of my graduate career I have greatly benefitted from the people around me who have been extremely supportive in numerous ways. Most importantly I would like to thank my advisor, Arjun Yodh for the opportunity to work in this field. His encouragement and support for exploring new ideas was invaluable as was his critical review of data, manuscripts and presentations. Besides my advisor I would also like to acknowledge the support of other members of the faculty who often served in advisory roles. I had several enlightening discussions with Tom Lubensky and Randy Kamien which were invaluable for this thesis. David Weitz was also available to ask the tough questions which helped provide direction for this work. In addition I learnt a lot at his group meetings which were often a battlefield for ideas.

Perhaps I owe the most to the postdocs and the graduate students on the third floor who created a work environment that was intellectually challenging and at the same time incredibly supportive, without which most of this thesis would not have been possible. I especially want to thank John Crocker who not only provided a lot of support for this thesis but was often available as a sounding board for ideas. Veronique Trappe was always available to tell me all about polymers and other things in life! I would like to thank Peter Kaplan, Thomas Gisler and Sophie Pautot for introducing me to microbiology and teaching me a lot about it. Also, without Cecil Cheung's help I would still be battling computer problems. I would also like to thank Eric

Weeks, Keng-Hui Lin, Joe Culver, Bill Angerer, Amani Gandour, NingPing Yang, and everyone else in both the Yodh group as well as the Weitz group for their help. It was also a pleasure to work with Ben Goodrich and Zigurts Majumdar. In addition I would also like to thank everyone at the RLBL, for all their help and advice during the time I spent there, especially Mark Phillips, Gilad Haran and David Cook.

Finally, I would not have made it through graduate school without the support of family and friends. My parents encouragement convinced me to pursue graduate school and Dave's support helped me finish it. Very simply, I owe them a lot! I would also like to thank my in-laws for their patience and understanding throughout all the stressful periods of graduate school. In addition I would like to thank all my friends for their constant support through this endeavor.

ABSTRACT

ENTROPIC ATTRACTIONS IN COLLOID-POLYMER SOLUTIONS

Ritu Verma

Arjun G. Yodh

We explore the depletion attractions that arise between hard colloidal spheres immersed in a non-adsorbing polymeric solution of DNA molecules. Using a scanning optical tweezer we were able to spatially confine colloidal particles along a line and quantitatively examine the interaction potential between two $1.25\mu\text{m}$ silica spheres moving in various complex fluids. At fixed DNA concentration, we found that the range and depth of the inter-particle potentials did not change for background salt concentrations between 0.1 and 20 mM. Then we fixed the background salt concentration at 10 mM, and measured the inter-particle potentials as a function of DNA concentration. The potentials obtained display variations in depth and range that are consistent with scaling behavior expected for semi-flexible polymers near the theta point. In particular we clearly observe the crossover from a dilute solution of Gaussian coils to the weakly fluctuating semi-dilute regime dominated by two-point collisions. We also quantitatively test the Asakura- Oosawa Model for these systems and show how it can be used in both the dilute as well as the semi-dilute regime.

We also explore the dynamics of colloidal particles in background DNA solutions. We find that the Stokes-Einstein picture breaks down in these complex fluids as the

size ratio of the probe particle to the characteristic polymer length scale is decreased. We explain these deviations in terms of the changes in the microenvironment caused by the presence of the depletion cavity. The colloidal spheres were also used to probe the transition time scales from the viscoelastic regime to the purely viscous regime.

Contents

1	Introduction	1
2	Introduction to Polymer Theory	8
2.1	Isolated Polymer Coils	10
2.2	Non-Ideal Behavior	14
2.3	Many Polymer Coils	22
2.3.1	Theoretical Models for Non-Ideal Polymers	25
2.4	Semi-Flexible Polymers	40
2.5	Conclusions	48
3	Polymer Depletion	50
3.1	Introduction to Depletion	51
3.2	Polymer Depletion	57
3.3	Correlation Hole Picture	61
3.4	The Infinite Plate Model	67
3.5	Large Sphere Interactions	72

3.6	Asakura-Oosawa Model vs. Mean-Field Predictions	76
3.7	Depletion in Different Polymer Phases	78
3.8	Polydispersity Model	81
3.9	Conclusions	87
4	Experimental Techniques	88
4.1	The Microscope	88
4.2	Optical Tweezers	96
4.3	The Detection System	108
4.4	Image Analysis	111
4.5	Sample Preparation	114
4.6	DNA Preparation	118
5	Equilibrium Interactions	133
5.1	General Experimental Procedures	134
5.2	Calculation of the Potential	136
5.3	Interaction Potentials	142
5.3.1	Dilute Region	146
5.3.2	Semi-Dilute region	148
5.4	Second Virial Coefficient	152
5.5	The Effects of Monovalent Salt	156

5.6	Conclusions	160
6	Particle Dynamics in DNA solutions	162
6.1	Brownian Motion	165
6.1.1	Langevin Formalism	166
6.2	Single Particle Tracking Measurements	169
6.2.1	Particle Tracking Techniques	170
6.3	Results	178
6.3.1	Fixed Colloid Size	179
6.3.2	Fixed DNA Concentration	184
6.4	Coupled Diffusion in Polymer Solutions	191
6.5	Two-Sphere Measurements	195
6.5.1	Diffusion in an Optical Trap	196
6.5.2	Experimental Results	198
6.6	Conclusions	203
7	Conclusions and Future Work	204
A	The Second Virial Coefficient	210
B	Free Energy Minimization	212
C	List of IDL Routines	215

List of Figures

2.1	An ideal polymer coil	11
2.2	A comparison between the different size measures of a polymer coil. .	15
2.3	A typical link interaction potential. The attractive well is usually attributed to Van der Waals forces.	17
2.4	The correlation length in semi-dilute solutions.	24
2.5	The different concentration regimes of a polymer solution.	26
2.6	A phase diagram for flexible polymers	43
2.7	A phase diagram for semi-flexible polymers.	46
2.8	Phase diagram for Polystyrene in tetrahydrofuran.	48
2.9	Phase diagram for λ -DNA in TE buffer.	49
3.1	The imbalance of forces in a binary hard sphere mixture	53
3.2	The excluded volume effect	54
3.3	The depth of the AO potential at contact for different sphere size ratios	56
3.4	Polymer depletion in dilute and semi-dilute solutions.	59
3.5	The gain in entropy shown on a lattice model	63

3.6	The polymer concentration between two infinite repulsive walls	68
3.7	A plot of the function $f(z/2\xi)$ which determines the polymer concentration profile	71
3.8	A cartoon of the Derjaguin approximation	73
3.9	The mean-field interaction potential between two large spheres.	74
3.10	The interaction potential in different polymer phases	80
3.11	The distribution of the second moment for a random walk.	83
3.12	The distribution for the maximum extent of a random polymer coil.	84
3.13	The depletion potential for different polymer radii distributions.	86
4.1	The Zeiss Axiovert 135.	90
4.2	The field and aperture planes of a microscope.	92
4.3	The gradient force in an optical trap.	98
4.4	The experimental set-up.	104
4.5	The scanning technique used to create a line optical tweezer.	106
4.6	A videograph of particles trapped in the line tweezer.	107
4.7	The overlap correction technique for a simulated image.	115
4.8	A typical sample cell.	116
4.9	The helical DNA structure.	120
4.10	The action of a restriction enzyme on double-stranded DNA.	122
4.11	The different steps of the fill-in reaction used to blunt end the λ -DNA.	124

4.12	A typical picture of gel electrophoresis.	127
4.13	Absorption spectra for a DNA solution	129
4.14	Fluorescent images of DNA molecules.	132
5.1	The probability distribution for the relative separation between particles.	137
5.2	Possible shapes for the optical potential.	138
5.3	The measured line optical potential.	141
5.4	The subtraction technique used in the equilibrium measurements. . .	143
5.5	A comparison between the fits to the different models.	144
5.6	The measured potentials for the dilute regime.	147
5.7	The measured potentials for the semi-dilute regime.	150
5.8	The scaling of the range of the depletion potential with DNA concen- tration.	151
5.9	A plot of the measured osmotic pressure versus the correlation length	151
5.10	The scaling of the osmotic pressure versus correlation length.	152
5.11	The calculated DNA phase diagram showing the regime probed by our experiments	155
5.12	The depletion potential at a fixed DNA concentration with different sized colloidal spheres.	156
5.13	The range of the depletion interaction at different salt concentrations.	158
5.14	A fluorescent image of a DNA in 0.1mM Tris Buffer.	159

6.1	A micrograph showing fluorescently labelled particles in solution. . .	173
6.2	A micrograph with particle positions superimposed	174
6.3	The integrated intensity of each particles vs. the measured radius of gyration.	175
6.4	Particle tracks for $1\mu\text{m}$ spheres in buffer solution.	176
6.5	The probability distribution for the measured displacements.	177
6.6	The mean square displacements for a $1\mu\text{m}$ sphere in buffer.	178
6.7	Polymer confined in a tube formed by the surrounding entanglements.	180
6.8	Mean square displacements for a $1\mu\text{m}$ sphere at different DNA concentrations.	180
6.9	The deviations from diffusive behavior at short times.	181
6.10	The change in viscosity as the DNA concentration is changed.	183
6.11	The change in the measured diffusion coefficient as the ratio of the bead size to the correlation length is changed.	186
6.12	Cartoon showing the strengths of the flow fields around beads of different sizes.	190
6.13	Mean square displacements in the optical trap.	199
6.14	The relative diffusion coefficient for two beads.	200
6.15	The relative friction coefficient between two beads in different DNA concentrations.	201

List of Tables

2.1	Examples of common synthetic and biological polymers [1].	9
2.2	Summary of properties of phases in Flexible Polymers	42
2.3	Summary of properties of phases in Semi-Flexible Polymers	45
6.1	Measured diffusion coefficients of different sized beads at different back- ground concentrations.	185
6.2	Mobility Matrix for Two Spheres in a Solvent	194

Chapter 1

Introduction

Very often the individual properties of the components of complex mixtures are well understood, but it is the subtleties of the interactions between the different components that give rise to new and interesting behavior. This thesis aims at understanding the issues that arise when two commonly used materials - colloids and polymers are mixed together. Colloid-polymer mixtures form the basic ingredients of a wide variety of systems ranging from commercial products such as frozen desserts and motor oils to natural biological systems, such as living cells. Thus the structural and dynamical properties of these complex fluids are of industrial, physiological, and fundamental interest, and they ultimately depend on the microscopic interactions between the suspension constituents. In this thesis we will address some of these issues.

The histories of these two materials are intertwined and date back to the 19th century. The word 'colloids' was coined by Thomas Graham in the late 1800's. He was trying to determine the diffusion of particles through a membrane and used the

term 'colloid' which means glue-like, to describe particles that did not pass through the membrane. It is interesting to note that most of the materials he used which fell into this category were actually polymeric, e.g. starch, cellulose, etc. Soon the word 'colloid' was used to describe a purely physical state that was attainable to most matter, just like a liquid or a gas. The broad ambiguous term was used to encompass a variety of materials ranging from gold sols to polymers and soap solutions. However, no attention was paid to the particular forces that made colloids stable. For example, the differences between the covalent forces that hold polymers together and the variety of other forces that can hold particles together was ignored. Thus the 'colloidal state' was not necessarily a reversible one. These ambiguities in nomenclature were resolved over time, primarily due to pioneering work by Staudinger [2]. By the thirties the term polymer was used to describe covalently linked molecules with complex architecture and was distinguished from the word 'colloid'. The term 'colloid' now refers to a suspension of particles in a fluid that are between 1nm - $1\mu\text{m}$ in size and feel the effects of thermodynamic forces.

For the purposes of this thesis, the term colloid is used interchangeably with hard sphere particle suspensions that are on the micron length scale. The composition of these colloidal particles may be polymeric, though the final structure bears no resemblance to the typical concepts associated with a polymer. The primary differences between polymers and colloids lies in the complex architecture of polymer molecules

that give rise to several degrees of freedom. For colloidal particles these degrees of freedom can be ignored and traditional descriptions of hard spheres, can be used to describe these properties in suspension. However to describe polymer behavior one has to resort to a statistical mechanical approach.

In solutions that contain both colloidal particles and polymers, the bulk properties of the solution are strongly determined by the particle-polymer interaction. This alters the particle-particle interaction which ultimately affects the macroscopic phase behavior of the complex fluid. Moreover, particle-polymer interactions also lead to changes in the dynamical properties of these mixtures that affect the rheology of these materials. The potential between polymers and particles can be broadly classified into two categories – attractive and repulsive interactions. In the first case the polymers adsorb onto the surface of the colloidal sphere, creating localized regions of high polymer concentration. In the repulsive case, we find that the colloid particles are surrounded by a region of low polymer density, called a depletion region.

Within the broad categories of attractive and repulsive interactions, there are several interesting variations that can be found. These arise due to the specific nature of the interactions. For example, the polymers in solution may contain an end group which forms covalent bonds with the molecules on the surface of the colloidal bead. This scenario leads to the formation of a brush-like layer on the particle surface, and is a technique that is often used to sterically stabilize particles. In industrial

solutions of high ionic strength, colloidal particles tend to aggregate due to van der Waals interactions. A layer of polymer on the surface prevents the beads from getting close enough to feel these forces. Another interesting polymer-particle interaction results when the end group on the two ends of a linear polymer molecule can bind irreversibly to the colloid surface. This leads to bridging between different colloidal beads to form gel like networks. Often industrial materials need to exploit the elasticity of polymeric substances while maintaining a rigid shape and use such interactions to introduce colloidal particles into the interstices of polymer networks. Attractive interactions between colloidal particles need not be as specific as the ones described so far. Polymers may adsorb onto the colloidal particles anywhere along its backbone. This leads to an increase in the particle hydrodynamic radius which changes with the polymer concentration. An interesting example of binding along the backbone can be found inside cells. The cell is faced with the problem that large quantities of genomic information carried by DNA need to be efficiently packed into a small volume. It is believed that one way in which this is achieved is by wrapping the DNA around histones (globular proteins that are colloid-like). This process is thought to be driven by the electrostatic affinity between polymeric DNA and colloidal proteins.

Solutions in which the colloids and polymers repel each other, lead to attractive interactions between the colloidal particles. Colloidal aggregation can occur in non-adsorbing polymer solutions since the increase in osmotic pressure due to exclusion

of polymer from the depleted regime leads to attractive forces. These effects are discussed in detail in Chapter 3. Interesting examples of the depletion effect can be found in biological systems. Adhesion between lipid bilayer membranes has been attributed to the depletion effect. Binding between antigens and antibodies is also attributed to depletion driven aggregation effects. Technologically the depletion effect can be used to aggregate colloids in a controlled way and may prove to be useful for protein crystallization techniques.

The strength of the interactions between colloids and polymers depends on the specific nature of the attraction. The energy of interaction usually ranges from being sub- $k_B T$ in solutions where entropy is the dominant mechanism to $300k_B T$ in systems where covalent chemical binding effects are prevalent. Various instruments such as the surface force apparatus and atomic force microscope have been used to measure these particle-polymer forces. However the force resolution of most of these techniques is limited (the magnitude of the forces measured are over a piconewton), even though the spatial resolution ranges in the angstrom regime. As a result, extensive studies have been carried out on systems in which polymer-particle interactions are fairly strong, however the weaker entropy dominated interactions are still not understood (a few examples can be found in Refs.[3, 4, 5, 6, 7] . Moreover these experiments mimic colloid-polymer suspensions by replicating the material properties, but rarely the geometries. Large flat walls, or slightly curved ones, are used as model systems.

Experiments that directly probe the characteristics of the suspension include scattering techniques and visualization techniques that monitor the macroscopic changes in phase behavior when the system parameters are altered. Both these techniques, use indirect means to qualitatively determine the microscopic interactions. More recently optical techniques using tweezers and total internal reflection microscopy are being used [8, 9]

In this thesis we focus on the femtonewton forces that arise in non-adsorbing polymer colloid solutions, that have evaded many measurement techniques. As a result, interactions between colloids and polymers are poorly understood, despite the fact that each of the individual components has been extensively studied. We present direct measurements of the depletion forces in a model system consisting of polymeric DNA and silica particles [10]. In the following chapters we discuss the entropic attractions in DNA solutions. In the first chapter we discuss the details of polymer theory that are relevant to our experiments. In particular we discuss the derivation of the state diagram that is important for our analysis. In the next chapter, Chapter 3, the mechanism that drives depletion in polymer solutions is discussed. We derive a mean-field depletion potential and compare it with the phenomenological Asakura-Oosawa model. The techniques used in this thesis to study these interactions in DNA systems is described in Chapter 4. Details of the optical tweezer, video microscopy and DNA preparation techniques is presented. The results from these measurements form the

core of Chapter 5, where the subtleties of the measured potentials are discussed. The qualitative and quantitative aspects of the data are analyzed and discussed in context with the polymer depletion models. The implications of the measured energetics and structure on the dynamics of beads in polymer solutions is explored in Chapter 6. We obtain non-Stokesian diffusion behavior which highlights the importance of the correlation cavity in polymer solutions. We conclude with a summary of our findings and explore the new systems that we could study in the future.

Chapter 2

Introduction to Polymer Theory

Polymers form the building blocks of both technologically and biologically important materials. Efforts to create new polymer molecules with novel material properties are always underway [1]. In addition recent investigations into biopolymers, such as DNA, proteins, actin, etc. [11, 12, 13], promise to introduce new classes of materials with wide-ranging applications. To understand what distinguishes these materials from traditional solids and liquids we need to examine the rich variety of chemical and physical properties displayed by polymer molecules. This chapter addresses the theoretical aspects of the physical properties of polymer solutions, with an emphasis on understanding the properties of DNA.

The basic unit that makes up a polymer is called a monomer. These molecules form repeating units that are chemically linked together to form a chain [14, 15, 16, 17]. For example, polystyrene, a common ingredient in coffee cups and packing peanuts, is a chain formed out of the hydrocarbon, $C_6H_5CH = CH_2$, commonly called

Common Name	Acronym	Repeat Unit	Conformation
Polystyrene	PS	$C_6H_5CH = CH_2$	Linear
Poly(ethyl)	PMMA	$-CH_2 - CH_2 - O-$	Linear
Deoxynucleoribose	DNA	A,G,C,T	Circular,Linear
Actin	f-actin	g-actin	rod-like
Poly-Aspartic Acid	Asp	$CH_2 - COOH$	Branched
Glycine	Gly	$-CH(NH_2) - COOH-$ $C - CH(NH_2) - COOH$	Branched

Table 2.1: Examples of common synthetic and biological polymers [1].

styrene [1]. The simplest linking structure for monomers, is a linear chain, however other topological constraints can be built in. For example, bacterial plasmids are linear chains which are joined on the ends to form a macromolecular ring [18]. Chains can also tether to a central unit to form star polymers or randomly attach at different junctures to form dendrimers, or branched polymers. In either case, the multiply connected molecules give rise to structural properties which have length scales and time scales that are very different from those seen in simple liquids and solids.

In this chapter we develop the formalism to understand the solution properties of polymeric molecules. Polymers in solution are free to adopt a large number of conformations. Unlike a single point-like molecule that usually has only translational degrees of freedom in solution, a polymer molecule enjoys additional freedom because

it can rearrange by bending and twisting at its multiple joints. Understanding this increased phase space is crucial in elucidating the role of polymers in macromolecular systems. We focus on the properties that arise due to the tertiary structure of the molecule, i.e. the long range spatial structure of the polymer. For example, a DNA molecule has a primary structure that is determined by the exact sequence of base pairs and a secondary structure that is controlled by short range order such as the helical twists. But the conformation adopted by the DNA molecule is controlled by the long-range order between links [17]. These structures give rise to novel interactions in crowded macromolecular solutions.

We first develop the tools needed to describe the conformational properties of macromolecules. We then address the issues that arise as interactions between links and ultimately between different polymer coils start to dominate. Both a self consistent mean field approach and scaling arguments are used to address the problem. Finally, in last section we highlight the different physics that arises in polymer solutions as the long range order of the links is altered - a situation that often arises due to changes in the chemical environment of the macromolecule.

2.1 Isolated Polymer Coils

The shape of a polymer chain in solution is much like the trajectory of a drunk who is limited to taking a finite number of steps. The radius of the area explored is

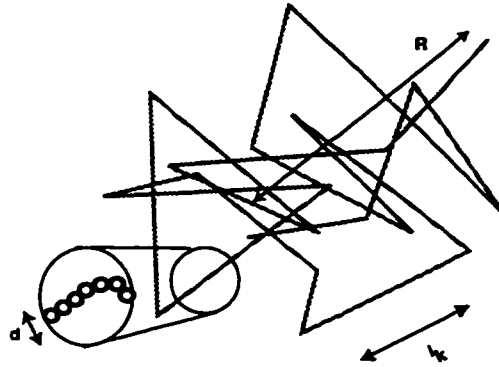


Figure 2.1: An ideal polymer coil, with a segment length, l_k and a monomer diameter d . The end-to-end distance, R is also shown.

easily calculated, even though there are numerous paths that the drunk could take. In the absence of external forces, the polymer does not extend out to its full length but it adopts a random coil configuration. The numerous configurations available to a polymer coil in solution makes a statistical description of its characteristics particularly useful.

The polymer coil can be modeled by a random walk [19]. Each repeating unit (or monomer in the simplest case) is treated as a step of length, l , and the number of steps, N is equal to the degree of polymerization. The end-to-end molecular displacement vector, \mathbf{R} is given as the vector sum of all steps, \mathbf{l}_i ,

$$\mathbf{R} = \sum_{i=1}^N \mathbf{l}_i \quad (2.1)$$

If the motions of nearby monomers are uncorrelated, $\langle \mathbf{l}_i \cdot \mathbf{l}_j \rangle = 0$; ($i \neq j$), the mean square end-to-end distance which describes the characteristic size of the molecule is

given by

$$\langle \mathbf{R}^2 \rangle = Nl^2. \quad (2.2)$$

A polymer that can be described by this simple picture is usually referred to as an ideal polymer or a Gaussian coil. The latter name arises because the distribution function, $\Phi(\mathbf{R}, N)$ that describes the probability that a polymer of N links has an end-to-end vector, \mathbf{R} , is Gaussian, i.e.,

$$\Phi(\mathbf{R}, N) = \left(\frac{3}{2\pi Nl^2} \right)^{3/2} e^{-\frac{3\mathbf{R}^2}{2Nl^2}}. \quad (2.3)$$

The random walk model provides a powerful tool for describing polymer behavior in solutions. However it also implies that the polymer links are capable of exploring all space. This assumption rests on the fact that the chemical joints between links are such that the links are free to rotate through arbitrary angles (N.B.: this gives rise to another commonly used name - the *freely jointed model*). This is usually not true for typical joints between monomers. Correlations between angular motions of the monomers vanish exponentially on a length scale called the persistence length, l_p . Physically the persistence length, is the length along the chain over which the memory of the chain direction is maintained. Since this correlation 'persists' in two directions from any point on the chain, the Kuhn length, l_k is introduced and defined as:

$$l_k = 2l_p. \quad (2.4)$$

The Kuhn length is used as the new random walk step length. It also plays an important role in determining the flexibility of the polymer, which in turn leads to significant changes in the bulk behavior of the polymer as will be described later.

The real polymer is now readily described as a random walk with renormalized segment lengths and effective links. For a given polymer of length L and persistence length l_p , the number of links is

$$N_{\text{eff}} = L/2l_p \quad (2.5)$$

and the mean end-to-end distance is

$$\langle R^2 \rangle = 4N_{\text{eff}}l_p^2 = 2Ll_p = Ll_k. \quad (2.6)$$

An alternative and equivalent way to describe the polymer is the bead model [17]. In this model the polymer is taken to consist of finite sized beads at representative points along its length, separated by massless filaments. The points are chosen far enough apart so that the correlations between them are Gaussian. In other words they have to be further apart than a Kuhn length. The number of such beads is found by dividing the total length of the polymer by the length of the connecting filaments. Once again the mean square end-to-end distance is given by $\approx N_{\text{bead}}a^2$, where a is the distance between the beads.

Experimental probes have verified the validity of these theoretical models. Scattering techniques, using both light [20, 21, 22] and neutrons [23, 24, 25] have probed

the radius of gyration, R_G of the polymer coil. Viscometric measurements[20, 26] have also been used to determine the effective size of the polymer coil however these techniques usually probe the hydrodynamic radius of the coil. Both the radius of gyration and the hydrodynamic radius, R_H , are probes of the second moment of the probability distribution given in Eq. 2.3. They can be related to the mean square end-to-end distance $\langle \mathbf{R}^2 \rangle$ through constants which are given by

$$R_G^2 = \frac{1}{6} \langle \mathbf{R}^2 \rangle; \quad (2.7)$$

$$R_H^2 = \sqrt{\frac{3\pi}{128}} \langle \mathbf{R}^2 \rangle. \quad (2.8)$$

The differences between these two measurement techniques are highlighted in Fig. 2.2. We see that any measurement involving liquid flow effectively penetrates further into the polymer coil whereas measurements sensitive to steric configurations probe the radius of gyration.

2.2 Non-Ideal Behavior

In a real polymer solution it is often difficult to find an ideal polymer coil. Interactions between the links cause significant deviations from the Gaussian nature of the chain statistics. In this section we explore the fine balance between the different interactions - steric, chemical, and electrostatic, that determine how the polymer coil swells or collapses into a globule. We include the Flory results that are traditionally used to describe the change in polymer size due to link interactions and discuss the different

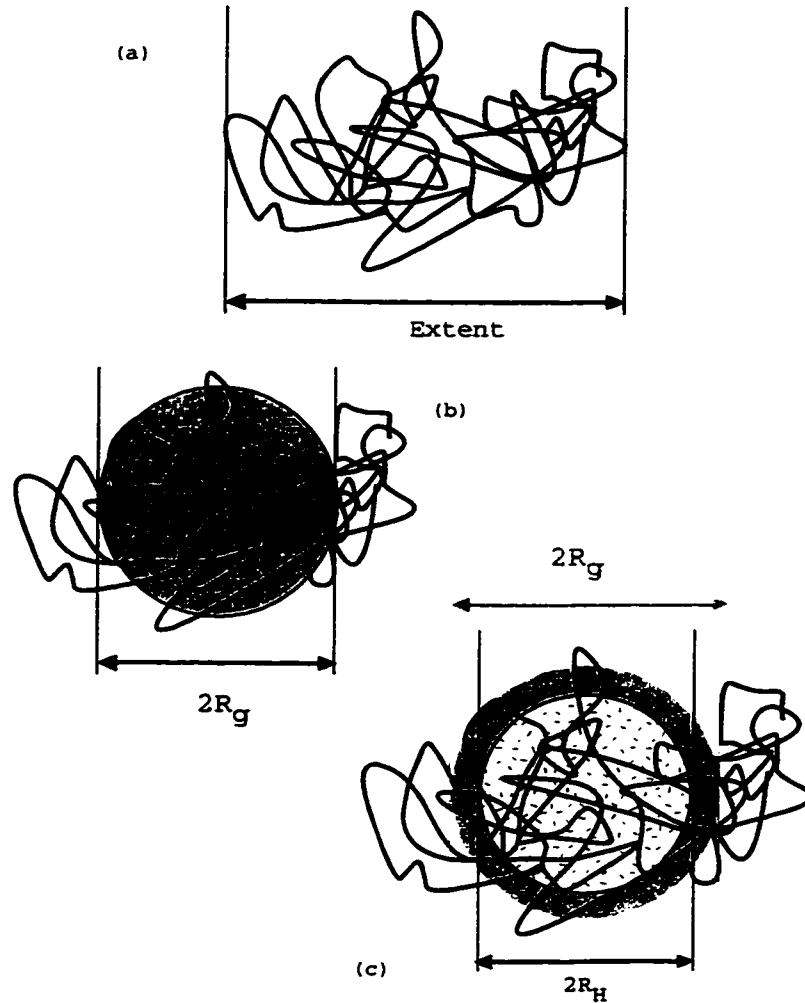


Figure 2.2: A comparison between the different sizes that can be measured for a polymer coil. In figure (a) we see the extent of the polymer coil which measures the maximum displacements between links. However scattering techniques probe a smaller size given by the second moment of the probability distribution $P(R)$ (see Eq. 2.3), i.e. the radius of gyration which is shown in (b). Viscosity measurements probe the hydrodynamic radius (c) which is smaller than R_g , since the solvent penetrates further into the polymer coil, feeling a smaller effective radius.

methods that are used to characterize these effects in polymer solutions.

Link-link interactions are usually described as repulsive on short length scales and attractive on longer length scales. The repulsion arises from steric effects; the primary consideration being the fact that each link occupies a finite geometric volume, and thus excludes other links from this region. The link attraction typically results from Van der Waals forces. The competition between these two effects leads to an effective interaction potential between links such as the one shown qualitatively in Fig. 2.3. These interactions primarily reduce the available volume for the polymers and as a result are usually called excluded volume effects. A modified random walk calculation, called a self avoiding random walk model (SAW) [16] in which links are not allowed to cross or overlap, is used to describe such polymers. This serves as an important model for computer simulations on polymer configurations.

The most obvious effect of self avoidance is to change the scaling behavior of the coil with respect to N . In the ideal case we found that the size of the coil scaled with link number as $N^{1/2}$. When excluded volume interactions are included we find that the size scaling goes to $N^{3/5}$. This was first shown by Flory [14, 15], using simple energy arguments. He showed that the free energy of a Gaussian coil is directly proportional to the mean-square end-to-end distance, $\langle \mathbf{R}^2 \rangle$ (this can be derived from Eq. 2.3 by using the fact that the free energy is related to the entropy through $F_{el} \propto -k_B T \ln \Phi \propto \frac{3R^2}{2Nl^2}$). Thus any increase in size produces an inhibiting elastic

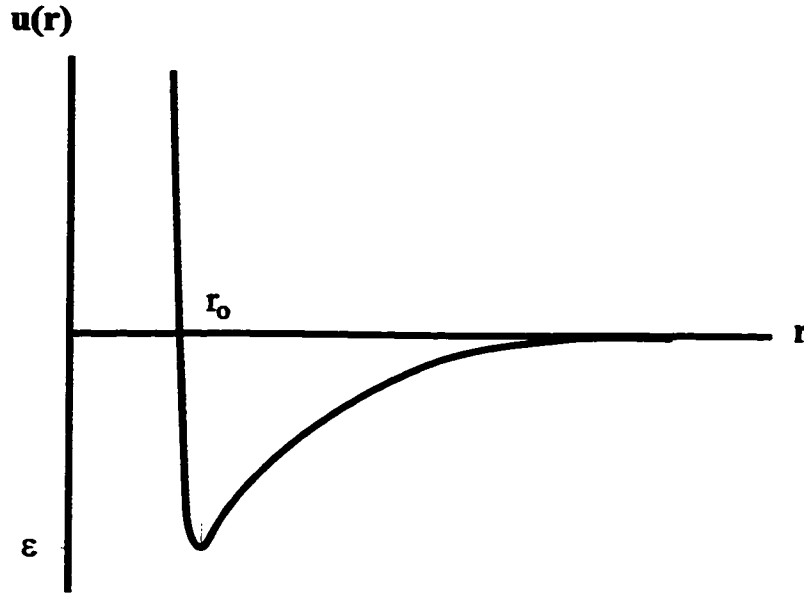


Figure 2.3: A typical link interaction potential. The attractive well is usually attributed to Van der Waals forces.

force. The effects due to interactions were included through a virial expansion of the free energy. The interaction energy in the volume occupied by the coil is given by, $F_{int} \sim k_B T v \bar{c}^2 R^3 = k_B T v N^2 / R^3$, where \bar{c} is the average polymer concentration and v characterizes the excluded volume effect and is weighted by the polymer density, N/R^3 . The combination of the entropic effects from coil expansion and the excluded volume interactions give the total free energy, F as

$$F/k_B T = \frac{3R^2}{2Nl^2} + \frac{vN^2}{R^3} \quad (2.9)$$

Minimization of the free energy with respect to R yields a Flory radius, R_F , which is given by

$$R_F \propto v^{1/5} l^{2/5} N^{3/5}. \quad (2.10)$$

Though not exact, the model comes close to describing a swollen polymer coil. More sophisticated renormalization group theory predictions calculate the exponent of N to be 0.588 [27, 28].

Let us elaborate further on the contributions to the free energy that result from the excluded volume effects. Just as corrections to the ideal gas model are expressed in terms of virial coefficients which account for molecular interactions, similarly, excluded volume interactions between links in a coil can be incorporated into polymer theory. The free energy of a polymer coil can be expanded in a concentration series to include the effects of interactions. The virial expansion is usually written as

$$F/k_B T = (c/N)\ln(c/Ne) + Bc^2 + Cc^3 + \dots \quad (2.11)$$

where B and C are second and third order virial coefficients, respectively and c is the monomer concentration. The corresponding osmotic pressure is given by $\Pi/k_B T = c/N + Bc^2 + 2Cc^3 + \dots$. The second virial coefficient is defined by the usual binary cluster integral (see Appendix A) which is given by

$$B(T) = (1/2) \int d\mathbf{r} (1 - e^{-u(\mathbf{r})/k_B T}) \quad (2.12)$$

where $u(\mathbf{r})$ is the interaction potential between links and \mathbf{r} is the relative separation between links. A typical interaction potential is shown in Fig. 2.3. We see that at short distances the potential is dominated by a large repulsive barrier that arises due to steric considerations. As the inter-link distance is increased this gives way to an attractive region which results from Van der Waals forces.

We can calculate the second virial coefficient by decomposing the interaction potential into two parts [29]. The well defined minimum at r_o , can be used to define two regimes. At distances under r_o the potential is primarily repulsive, i.e $u(r) \rightarrow \infty$, but at larger separations the potential is attractive. This attractive regime can be modeled by the r^6 dependence shown by Van der Waals potentials. We can rewrite the integral in Eq. 2.12 as

$$2B(T) = 4\pi \int_0^{r_o} dr r^2 + 4\pi \int_{r_o}^{\infty} dr r^2 [1 - e^{\frac{\epsilon}{k_B T} (\frac{r_o}{r})^6}] \quad (2.13)$$

where ϵ represents the depth of the potential at equilibrium. A straightforward integration shows that the first term yields the volume of a link, $(4\pi r_o^3/3)$. The second term is evaluated in the limit in which $T \gg \epsilon$, in which case the exponential can be expanded as, $1 + \frac{\epsilon}{k_B T} (\frac{r_o}{r})^6 + ..$ to yield, $\sim -\frac{4\pi\epsilon}{3k_B T} r_o^3$. Thus we see that the second virial coefficient goes from being a positive number to a negative number, as different regimes of the interaction potential become important. This often leads to instabilities which in polymer solutions might drive the coil-globule phase transition.

In a polymer solution, temperature changes control the interaction between the links. Not only can these changes be brought about by adding heat to the solution but also by changing the chemical environment through the background solution. The temperature at which the second virial coefficient is zero is termed the Θ -temperature. At this temperature the excluded volume effects are effectively canceled by the link interactions since B is identically zero. Deviations from this temperature are charac-

terized by the parameter, τ [17], which is defined as

$$\tau \equiv \frac{(T - \Theta)}{\Theta}. \quad (2.14)$$

At temperatures where $T \gg \epsilon/k_B$, the second virial coefficient is positive, and is dominated by the first term in Eq. 2.13, i.e. $B = v$, where v is the excluded volume of the polymer link, $v = (4/3)\pi r_o^3$. The polymer molecule never feels the attractive well and interactions are controlled by the repulsive barrier. As the temperature is decreased it approaches, the Θ -temperature where the second virial coefficient is zero. Around this region Eq. 2.12 can be expanded and B is found to increase linearly with τ , i.e. $B \sim v\tau$. However as the temperature continues to fall the polymer molecule lies close to the equilibrium position, r_o in Fig. 2.3 and the attractive region in the interaction potential starts to dominate leading to the formation of globules. The second virial coefficient is found to be proportional to $-\epsilon v/k_B T$ in this case.

The interaction between the links arises due to solution mediated forces. In solutions where the interactions are purely repulsive, i.e. when $B \gg 0$, it is easy to suspend a polymer molecule, giving rise to the name ‘good solvents’. On the other hand solutions in which, attractive interactions dominate are called ‘poor solvents’ since the polymers are likely to form globules and condense out of solution. The intermediate solution in which there are no link interactions are called Θ -solvents.

For a polymer solution, the implications of the changes in the second virial coefficient can be seen in the coil size. If repulsion dominates, then the coil size appears

larger. If attraction dominates, then the coil can appear condensed. Thus one way to determine the solvent quality is to look at the ratio of the measured size and the calculated ideal (Gaussian) size. This ratio is called the swelling parameter [17] and is given by

$$\alpha^2 = \frac{\langle R_{actual}^2 \rangle}{\langle R_{ideal}^2 \rangle} \quad (2.15)$$

Thus if $\alpha^2 > 1$, the polymer coil is swollen, if $\alpha^2 = 1$ then it is ideal and if $\alpha^2 < 1$ it is a globule.

If the excluded volume parameter is small then the mean end-to-end distance can be expanded in terms of B [17]. This results in

$$\langle R^2 \rangle = Nl^2(1 + (4/3)z + \dots) \quad (2.16)$$

where z is defined in terms of the microscopic variables, N , l , and B as

$$z \equiv 2 \frac{3^{3/2}}{2\pi} N^{1/2} \frac{B}{l^3} \quad (2.17)$$

Physically, the z parameter can be understood as the number of binary collisions, ($\sim N \times vol.fraction$), in the coil with B as the weighting factor for these collisions. We discuss the role of the second virial coefficient in describing macromolecular solutions in the next section.

2.3 Many Polymer Coils

In the previous sections we discussed the models used to describe an isolated polymer coil in solution. However real polymer solutions contain many polymer coils, and interactions between these coils have to be considered in order to describe the properties of the polymer solution. We discuss the different theoretical approaches used to describe such polymer solutions, in particular we focus on the self-consistent field theoretic methods. We also compare the mean field arguments with scaling arguments that are traditionally used to describe polymers. These results form the basis for discussing and developing depletion models in the chapters to follow.

In order to determine the effect of interactions between coils we need to quantify the number of coils present in the solution. This is usually done by measuring a polymer density or volume fraction. The density of polymers in solution is described equivalently by the number density of monomers, c , or the polymer coil density, n . The two quantities are related through the degree of polymerization, N , by

$$c = Nn. \quad (2.18)$$

Another useful dimensionless variable is the volume fraction which is defined as

$$\Phi = cv = nNv \quad (2.19)$$

where v is the volume occupied by a link, $(4\pi l^3/3)$. Experimentally most polymer weights are expressed in terms of a weight per unit volume, or $\rho = \frac{N_A}{M_w}n$, where M_w

is the molecular weight and N_A is Avogadro's number.

Polymer solutions can be divided into three regimes depending upon the number of coils that are present in solution. In a dilute solution, the polymer coil concentration is small, and we can still use the characteristics of an isolated coil such as the size and osmotic pressure it exerts, to describe the solution. However as more polymer is added to the solution the chains begin to overlap and the polymer solution enters the so-called semi-dilute regime. The overlap concentration, c^* marks the cross-over concentration. It is defined as

$$c^* = N / \left(\frac{4\pi}{3} R^3 \right), \quad (2.20)$$

where R is the effective size of the polymer coil. For example in a solution containing Gaussian coils, $R = R_g$, but in a solution where the coils are swollen the size would be determined by the Flory radius, R_F . In either case the crossover concentration describes a system of close-packed spheres, whose effective diameter is given by the characteristic size of the polymer. Beyond c^* , the physics of the solution changes as entanglement effects come into play. Collisions with other polymers lead to the origin of a new length scale, the correlation length, ξ , which describes the average spatial distance between entanglement points (see Fig. 2.4). On length scales under ξ the polymer can still be modeled as a random (or in the case of a non-ideal polymer a self-avoiding) walk, but on larger length scales the presence of the surrounding polymers must be taken into account.

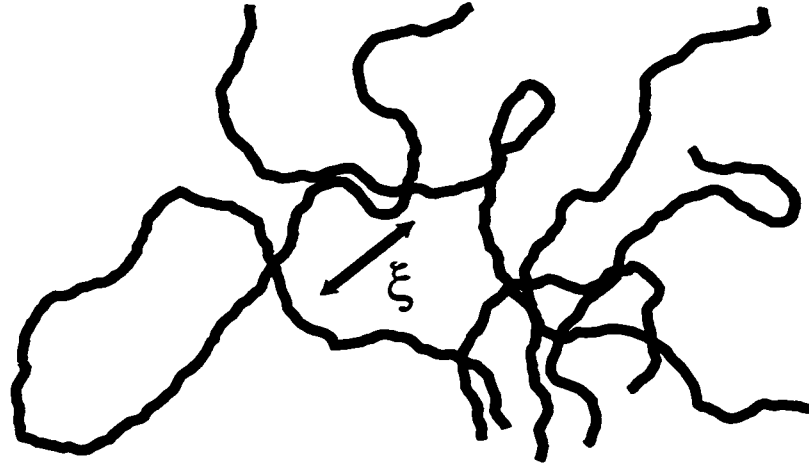


Figure 2.4: The correlation length in a semi-dilute polymer solution. It describes the mean distance between entanglement points.

Equivalently a semi-dilute polymer solution can be described as a close packed system of ‘blobs’, the mean size of which is given by the correlation length [16, 17, 30]. Within a ‘blob’ the polymer still behaves as an independent coil. Moreover since there are no correlations beyond the length scale, ξ , the blobs are statistically independent. This apparent dichotomy between a close packed system and an ideal gas like behavior is an important concept in polymer theory which we will revisit many times through this thesis.

The polymer volume fraction in the semi-dilute regime is still very small. At c^* , which scales as $N^{-4/5}$ in a good solvent and $\propto N^{-1/2}$ in a Θ -solvent, the volume fraction, is only $\approx 10^{-3}$ and $\approx 10^{-5}$, respectively, for a polymer with a high degree of polymerization, i.e. $N \approx 10^6$. As this volume fraction is increased and approaches unity, the polymer becomes heavily entangled, and the solution becomes

concentrated. Polymer solution properties can now once again be described by Gaussian statistics since crowding overcomes the excluded volume effects. This is counter intuitive but a detailed examination of the link interactions (see Ref. [16]) shows that the repulsive and attractive components exactly cancel each other as the monomer concentration is increased. Fig. 2.5 summarizes these three different regimes along with the corresponding density fluctuations that are typical in each regime.

We concentrate in this thesis on theoretical descriptions of the dilute and semi-dilute regions. In each of these regions we discuss the scaling properties of the osmotic pressure, and the correlation length. However we first briefly review the different theoretical approaches that have been used to describe polymer solutions.

2.3.1 Theoretical Models for Non-Ideal Polymers

Historically, polymers in solution were first described by Flory via a mean field theory [14, 15]. The theory was further developed and brought to its present state by S.F. Edwards [31]. However an alternative approach called scaling theory, was put forth by DeCloiseaux [32] and DeGennes[16] to account for the discrepancies that arose between experiments and mean-field predictions. More recently, renormalization group ideas[16] have been applied to polymers to obtain a greater degree of accuracy. We briefly discuss these approaches and their range of applicability.

The self-consistent mean field approach assumes that there is a single macroscopic

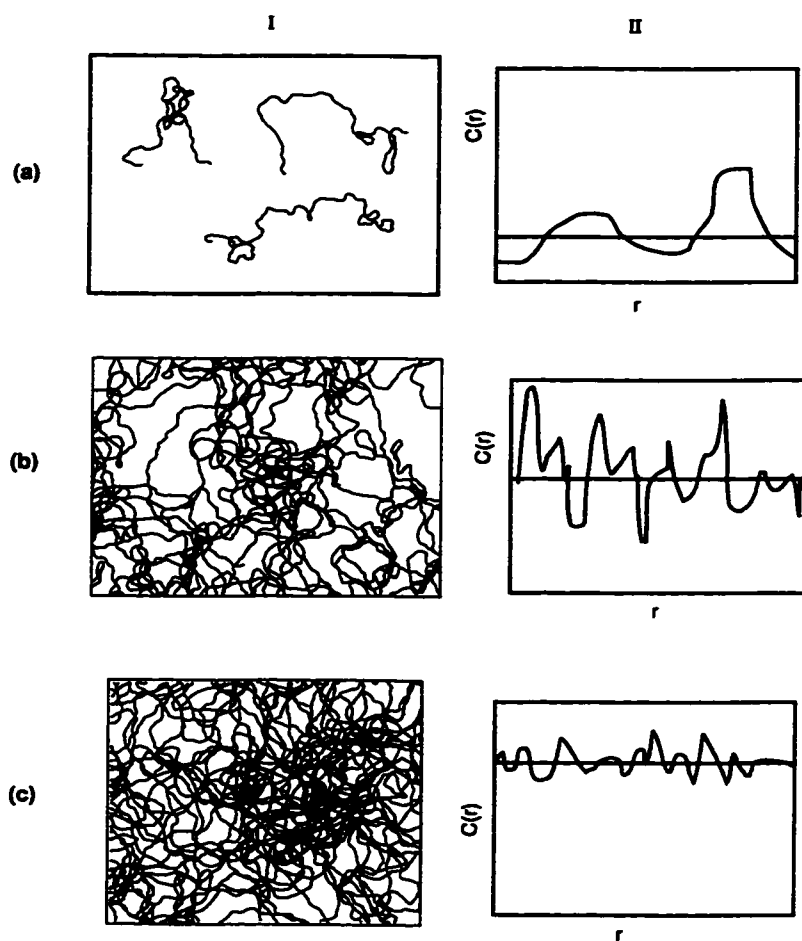


Figure 2.5: The different concentration regimes of a polymer solution. The cartoons in column I represent snapshots of polymer coils in solution. In Column II we see the concentration profile along a slice through the solution. The solid black line in Column II depicts the average monomer concentration of the bulk solution. In (a) we see a dilute solution which has large fluctuations around its mean concentration value. The fluctuations are reduced in the semi-dilute solution, (b), but can still produce large effects on polymer properties. In the concentrated solution, (c), the fluctuations around the mean concentration are very small.

state that is more favorable than others. The system finds this state and does not fluctuate. This state can be found by variational methods applied to the free energy of the system. For example the excluded volume effect discussed in the previous section can be modeled as a self-consistent field, $U(\mathbf{r})$ [16] (N.B.: There is no physical external field, like a magnetic field, however the interactions play a similar role in the free energy of the system). The repulsive interactions between links can be written as

$$U(\mathbf{r})/k_B T = v c(\mathbf{r}) \quad (2.21)$$

where $c(\mathbf{r})$ is the monomer concentration distribution and v is the excluded volume parameter (N.B.: The above equation is equivalent to Eq. 2.11 in the athermal limit.) Minimization of the free energy with respect to the concentration yields an equilibrium distribution of monomers which can be used to recalculate a new effective field and a subsequent new equilibrium concentration distribution. This iterative procedure eventually converges to a self-consistent potential. The fact that this is usually carried out under the assumption that the system can be modeled by an average concentration (even though it may not be the case, as was shown in Fig. 2.5), makes it a mean field calculation.

The mean field calculation ignores correlations between monomers and this limits its range of applicability to fairly dense polymer solutions. For example, a mean field description of a dilute system ignores density fluctuations; the approach includes

effects due to $\langle c \rangle^2$ but not due to $\langle c^2 \rangle$. The scaling approach [16] attempts to include effects that arise due to correlations between density fluctuations. It is based on arguments generally used to describe fluctuations near a second-order phase transition such as those that arise in magnetization in ferromagnets near the Curie point. The macroscopic properties of the polymer system are found to exhibit power law behaviors in which the critical exponent does not depend on the microscopic characteristics of the system. Reasonably simple arguments based on this approach give remarkably accurate descriptions of polymers in regimes where fluctuations are important.

However the primary drawback of scaling theory is that it fails to predict prefactors and constants measured in experiments. More recently, renormalization group methods [16] have been used to provide a rigorous, quantitative description of polymer behavior. These methods rely on the fact that the polymer can be divided into multiple blocks, which are used to calculate polymer properties. The size of these subdivisions are increased, and after each increment the polymer properties are recalculated, until the properties converge to a stationary point. A detailed description of these theoretical methods can be found in Ref.[16].

The Self-Consistent Mean Field Approach

In this section we elaborate on the methods used in the self-consistent mean field approach, since it can be used to describe most of our experimental observations. The mean field approach is commonly employed to describe the free energy of a polymer system, which in turn is the starting point for calculating various macroscopic properties exhibited by the solution. We use a Green's function approach to describe the different configurations that can be adopted by a polymer coil and find that the function conveniently satisfies a Schrödinger-like equation. This enables us to utilize the well known techniques of quantum mechanics to calculate the free energy and other properties of the polymer solution.

For an ideal polymer the spatial correlation between two points, \mathbf{r}_i and \mathbf{r}_j , located on a chain is Gaussian, i.e $g_{\text{gauss}}(\mathbf{r}_i, \mathbf{r}_j) \sim \exp[-3(\mathbf{r}_i - \mathbf{r}_j)^2/2l^2]$. However, in the presence of excluded volume effects, which can be modeled as an effective potential (Eq. 2.21) in the self-consistent mean field picture, the probability distribution is modified by the Boltzmann factor, $e^{\frac{U(\mathbf{r})}{k_B T}}$. We denote this new probability distribution as, $g(\mathbf{r}_i, \mathbf{r}_j) \sim e^{\frac{U(\mathbf{r}_i)}{k_B T}} g_{\text{gauss}}(\mathbf{r}_i, \mathbf{r}_j)$, where, i and j are two points on the polymer chain. In order to calculate the partition function for a coil with fixed ends, we need to sum over all the co-ordinates of the intermediate points, $d^3\mathbf{r}_i$. This function is a Green's function, and it represents the statistical weight attached to a chain of N links that

starts at \mathbf{r} and ends at \mathbf{r}_N . It is given by

$$G_N(\mathbf{r}_N, \mathbf{r}) = \int g(\mathbf{r}_N, \mathbf{r}_1)g(\mathbf{r}_1, \mathbf{r}_2)\dots g(\mathbf{r}_{N-1}, \mathbf{r})d\mathbf{r}_1\dots d\mathbf{r}_{N-1} \quad (2.22)$$

The Green's function satisfies the differential equation

$$\frac{\partial G_N(\mathbf{r}_N, \mathbf{r})}{\partial N} = -\frac{U(\mathbf{r})}{k_B T}G_N(\mathbf{r}_N, \mathbf{r}) + \frac{l^2}{6}\nabla^2 G_N(\mathbf{r}_N, \mathbf{r}) \quad (2.23)$$

where l is the link length, and N is the number of links in the polymer chain. A detailed derivation of this can be found in several texts [16, 19].

We see that Eq. 2.23 closely resembles the Schrödinger equation from quantum mechanics. A direct analogy can be drawn between N , the number of links in a polymer and the time variable in quantum mechanics. The Green's function, $G_N(\mathbf{r}_N, \mathbf{r})$ and wavefunction Ψ , are the coherent superposition of the amplitudes of the different paths followed by polymer links and particle wavefunctions respectively. This analogy allows us to draw from the numerous concepts and solutions that are well known from quantum mechanics. For example it is possible to write the right hand side of Eq. 2.23 as an operator, \mathcal{H} , with a set of eigenfunctions, u_k , such that

$$\mathcal{H}u_k = \epsilon_k u_k \quad (2.24)$$

where the operator is defined as

$$\mathcal{H} = -(l^2/6)\nabla^2 + U(\mathbf{r})/k_B T \quad (2.25)$$

Here ϵ_k is the eigenvalue of the operator, \mathcal{H} . Thus the Green's function can be expanded in terms of these eigenfunctions to yield

$$G_N(\mathbf{r}_N, \mathbf{r}) = \int dk u_k^*(\mathbf{r}_N) u_k(\mathbf{r}) e^{-N\epsilon_k} \quad (2.26)$$

We see that this sum is dominated by the lowest value of ϵ_k or the ground state, ϵ_0 . This is usually referred to as ground state dominance, and the eigenfunction u_0 is usually renamed $\psi(r)$. In the self-consistent mean field approach, it is assumed that the polymer always finds this state.

Just as in quantum mechanics, one can now use this result to calculate physical observables. For example, to calculate the link concentration in a polymer solution, $c(\mathbf{r})$, we calculate the sum of all paths from \mathbf{r} to \mathbf{r}' in M steps, and from \mathbf{r}' to \mathbf{r}_N in $N-M$ steps. Finally we sum over all possible intermediate steps, M . This can be written in terms of the Green's function as

$$c(\mathbf{r}) = \sum_M \int d\mathbf{r}' \int d\mathbf{r}'' G(\mathbf{r}', \mathbf{r})_M G(\mathbf{r}, \mathbf{r}'')_{N-M} \quad (2.27)$$

Assuming ground state dominance, i.e. $G_N(\mathbf{r}, \mathbf{r}') \sim u_0^*(\mathbf{r}) u_0(\mathbf{r}') e^{-N\epsilon_0}$, the above equation can be rewritten as

$$\begin{aligned} c(\mathbf{r}) &= \sum_M \int d\mathbf{r}' \int d\mathbf{r}'' u_0^*(\mathbf{r}') u_0(\mathbf{r}) u_0^*(\mathbf{r}) u_0(\mathbf{r}'') e^{-N\epsilon_0} \\ &= \text{const.} u_0(\mathbf{r}) u_0^*(\mathbf{r}) \\ &\propto |u_0(\mathbf{r})|^2 = |\psi(r)|^2 \end{aligned} \quad (2.28)$$

Conceptually, if we look at the point \mathbf{r} the concentration is determined by both the number of chains that are coming to the point as well as those that are leaving. This leads to the $|\psi(\mathbf{r})|^2$ dependence since we need a Green's function to get the chain to \mathbf{r} and another one for the chain to proceed from that point onwards.

We now return to calculating the free energy of the system. We first do this for the simple case when there are no interactions between the monomers, i.e. $U(\mathbf{r}) = 0$. The contributions to the free energy in this case arises solely from the conformational entropy of the system. The free energy can then be written as

$$\begin{aligned} F/k_B T &= \int d\mathbf{r} \psi^*(\mathbf{r}) \mathcal{H}_0 \psi(\mathbf{r}) \\ &= \frac{l^2}{6} \int d\mathbf{r} \psi(\mathbf{r}) (\nabla^2 \psi(\mathbf{r})) \\ &= \text{const} - \frac{l^2}{6} \int d\mathbf{r} (\nabla \psi(\mathbf{r}))^2 \end{aligned} \tag{2.29}$$

We see that in the absence of interactions the free energy is dominated by the conformational entropy of the coil and reproduces the ideal coil result.

The effects of the interactions can be included by adding the self-consistent potential $U(\mathbf{r})$ to Eq. 2.29. In addition the total free energy of the polymer coils also contains entropic contributions from the translational free energy of the monomers. Including both these effects allows us to write the total free energy as

$$F/k_B T = U(\mathbf{r})/k_B T - \frac{l^2}{6} \int d\mathbf{r} (\nabla c(\mathbf{r})^{1/2})^2 + \frac{c(\mathbf{r})}{N} \ln\left(\frac{c(\mathbf{r})}{Ne}\right) \tag{2.30}$$

where we have utilized Eq. 2.28 to replace the ground state eigenfunction, $\psi(\mathbf{r})$.

The first term represents the internal energy of the system and includes excluded volume interactions (N.B.: it can also include effects due to external constraints, like a repulsive wall); the second term is the entropy loss due to the connectivity of the links and the third term represents the translational entropy of the polymers. We will use this development of the free energy extensively to derive physical parameters for polymers within this approximation.

Physical Properties of Polymer Solutions

In this subsection we will calculate the osmotic pressure and the characteristic size of the polymers in solution. We divide our discussion into two parts; the dilute regime and the semi-dilute regime. The semi-dilute regime is described by both field theoretic methods and scaling theory.

I. Dilute Solution

In a dilute solution the polymer chains are far apart and their statistics can be modeled after the properties of an isolated coil as discussed above. In addition to the spatial dimensions of the polymer coil one can look at the osmotic pressure that is exerted by a chain. As in the case of an ideal gas the osmotic pressure for a Gaussian coil is given by

$$\Pi = \frac{c}{N} k_B T \quad (2.31)$$

If interactions are to be taken into account a virial expansion can be used, and the

osmotic pressure is written as

$$\Pi/k_B T = c/N + Bc^2 + 2Cc^3 + \dots \quad (2.32)$$

where B and C are the second and third virial coefficients, respectively.

II. Semi-Dilute Solution

The semi-dilute region can be described by both the self-consistent field method and the scaling approach. Both theories predict qualitatively similar behavior, but the exponents with which physical properties scale, do not agree. The self-consistent mean field approach does not account for fluctuations, but is a valid theory for polymers in which density fluctuations are not important, such as semi-flexible polymers. This will be discussed in detail in the last section. Most experimental deviations from the mean-field theoretic predictions are accounted for by the scaling method.

Self Consistent Field approach

We calculate the osmotic pressure of the polymer solution using a Flory Huggins approach wherein the concentration distribution is assumed to be a constant, i.e. $c(r) \rightarrow c$. This approximation ignores the connectivity of the links, and assumes that each monomer behaves like a free gas molecule. This implies that there are no contributions to the entropy due to the connectivity of the chain, i.e the $(\nabla c^{1/2})^2$ term in Eq. 2.30. In the Flory-Huggins model link connectivity is included by calculating the free energy on a lattice which restricts the positions of the links to a handful of sites. However the entropy of the system does contain contributions from the

translational entropy of the polymer molecules and the translational entropy of the solvent molecules. The total entropy of mixing, S_{mix} can be written in terms of the polymer volume fraction Φ as

$$\begin{aligned} S_{total}^{mix} &= k_B \frac{\phi}{N} \ln \phi + k_B \phi_{solvent} \ln \phi_{solvent} \\ &= k_B \frac{(cv)}{N} \ln(cv) + k_B (1 - cv) \ln(1 - cv) \end{aligned} \quad (2.33)$$

The internal energy contribution to the free energy contains monomer-monomer interactions, monomer-solvent interactions and the solvent-solvent interactions. It is given by

$$E^{mix} = k_B T (\chi_{mm}(cv)^2 + \chi_{ms}cv(1 - cv) + \chi_{ss}(1 - cv)^2) \quad (2.34)$$

where, χ_{mm} represents the monomer-monomer interaction strength, χ_{ms} describes the monomer-solvent interaction and χ_{ss} represents the solvent-solvent interactions. Each is weighted by the appropriate concentration of the species involved in the interaction.

These different interaction strengths can be combined together and written as

$$\chi = \chi_{ms} - (1/2)(\chi_{mm} + \chi_{ss}) \quad (2.35)$$

which is called the Flory parameter. It is related to the excluded volume parameter, v , discussed earlier through

$$v = (\chi - 1/2)l^3 \quad (2.36)$$

The entropy, (Eq. 2.33), and the internal energy, (Eq. 2.34) can be combined to give the total free energy, through the thermodynamic relationship, $F = E - TS$. Since

the concentration of monomers is very small even in the semi-dilute region, we can expand the free energy in small volume fraction, cv to give

$$F \sim k_B T \frac{cv}{N} \ln(cv) + k_B T \frac{1}{2} (cv)^2 (1 - 2\chi) + k_B T \frac{1}{6} (cv)^3 + \dots \quad (2.37)$$

The osmotic pressure, Π , can be calculated from the free energy by using the thermodynamic relationship, $\Pi = (\phi) \frac{\partial F}{\partial \phi} - F$, which yields

$$\Pi = k_B T \frac{cv}{N} - k_B T \frac{1}{2} (1 - 2\chi) (cv)^2 + \dots \quad (2.38)$$

We see that as the volume fraction approaches zero we retrieve the ideal gas law, $\Pi/k_B T = c/N$, and as the concentration is increased the effects of the second order terms start to dominate.

The free energy given in Eq. 2.30 can also be used to calculate the correlation length of the entangled polymer solution in the semi-dilute regime. This is usually done by examining the correlations between concentration fluctuations that are induced due to small perturbations. The effect of the fluctuations can be calculated by expanding the concentration fluctuations around the equilibrium concentration value. This can be understood by looking at a harmonic oscillator system. In the mean field approach the average polymer concentration corresponds to the equilibrium position for a particle in a harmonic well. Small forces acting on the particle would lead to excursions around the mean value and can be modeled by inclusion of quadratic terms in the particle's potential. Similarly an expansion of the polymer concentration

around the mean value allows us to characterize its response to the perturbation. The application of mean field calculations to correlation predictions is called the random phase approximation.

We return to Eq. 2.30 and examine the results in the random phase approximation to calculate the effects of fluctuations. The polymer concentration, $c(\mathbf{r})$, is expanded around its mean value by setting $c(\mathbf{r}) \rightarrow c + \delta c(\mathbf{r})$, and assuming that the mean concentration, c is uniform throughout the solution. Substituting this expansion in Eq. 2.30 yields,

$$F = \int \mathbf{r} E(\mathbf{r}) - \frac{Tl^2}{6} (\nabla(c + \delta c(\mathbf{r}))^{1/2})^2 + T \frac{(c + \delta c(\mathbf{r}))}{N} \ln \frac{(c + \delta c(\mathbf{r}))}{Ne} \quad (2.39)$$

Since the deviations from the mean are small we can Taylor expand the concentration and rewrite Eq. 2.39 as,

$$F = F_0(c) + \int d\mathbf{r} \frac{(\delta c(\mathbf{r}))^2}{2c} \left(\frac{\partial \Pi}{\partial c} \right) + \frac{Tl^2}{24c} (\nabla \delta c(\mathbf{r}))^2 \quad (2.40)$$

where only terms of order δc have been retained and $F_0(c)$ represents the unperturbed free energy. We have also used the fact that $\frac{\partial \Pi}{\partial c} \propto \frac{\partial E(\mathbf{r})}{\partial c} + 1/N$. The expression can be simplified by grouping the first two terms and redefining the coefficient as

$$\xi^2 \equiv \frac{l^2}{12} \left(\frac{\partial \Pi}{\partial c} \right) \quad (2.41)$$

which allows us to write down a simplified version of Eq. 2.40 as

$$F = F(c) + \frac{Tl^2}{24c} \int d^3r \frac{(\delta c(\mathbf{r}))^2}{\xi^2} + (\nabla \delta c(\mathbf{r}))^2 \quad (2.42)$$

From the above equation it is easy to see that in order to minimize the free energy the last two terms should equal zero. With a little bit of rearrangement and integration by parts (see Appendix B) this minimization yields an Ornstein-Zernicke like equation for $\delta c(r)$,

$$\nabla^2 \delta c - (1/\xi^2) \delta c = 0. \quad (2.43)$$

The above equation is similar to the Debye-Hückel equation in electrostatics, and the inherent length scale, ξ plays a similar role as its electrostatic counterpart. We can use the Flory-Huggins approximation in which the osmotic pressure at low concentrations is given by Eq. 2.32, to explicitly write the correlation length as

$$\xi^2 = (l^2)/12(2Bc + 6Cc^2 + 1/N)^{-1} \quad (2.44)$$

where, B and C are the virial co-efficients discussed in Section 2.2 and l is the link length. This mean field description of the screening length was first quantitatively calculated by S.F. Edwards [30]. Once again this is a useful description for entangled polymer solutions in which the concentration fluctuations are small, i.e $\delta c \ll c$, allowing the use of a perturbative treatment.

Scaling Approach

We can repeat the analysis for the predictions above by using a scaling argument. In this approach it is assumed that the ratio of the concentration to the critical overlap concentration, i.e. c/c^* is a fundamental parameter that defines the scaling

properties of the polymer solution. All polymer properties can be expressed as a power law of this fundamental parameter. The exponent that determines the scaling of the different polymer properties are determined by imposing two conditions - the results should smoothly approach the dilute solution predictions and they should be independent of the degree of polymerization, N , since the memory of the original chain is lost in the semi-dilute regime.

To calculate the osmotic pressure, we assume that Π is related to the ratio c/c^* through a critical exponent, m , and is given by

$$\Pi \propto (c/c^*)^m \quad (2.45)$$

When used in conjunction with, $c^* \propto N^{-4/5}$, the above equation can be written as

$$\Pi \propto c^m N^{4m/5-1} \quad (2.46)$$

By requiring the osmotic pressure to be independent of N , we calculate $m = 5/4$.

This yields

$$\Pi = Kc^{9/4}. \quad (2.47)$$

where K is an undetermined multiplicative constant. The osmotic pressure scales with concentration as $9/4$ which is different from the mean field result obtained earlier (Eq.2.38), where $\Pi \sim c^2$. The difference arises from the inclusion of correlation effects.

An entanglement length for the semi-dilute solution can be calculated in a similar manner. By constraining the expression to be independent of N , as well as requiring

the value to approach a Flory radius, R_F , at c^* , gives

$$\xi = R_F(c/c^*)^{-3/4} \quad (2.48)$$

Once again the concentration dependence deviates from mean-field predictions of $-1/2$.

We have presented a description of polymer solutions using both the self-consistent mean field description as well as scaling approach. We see that predictions for the osmotic pressure and correlation length scale differently in these two theories. The differences arise primarily due to concentration fluctuations that are seen in polymer solutions. The excluded volume interactions lie at the core of these fluctuations. Thus solutions which have strong repulsive link interactions are more likely to follow scaling theory predictions. On the other hand if the interactions between links is zero the solution can be well described by a mean field theory. This theory is also applicable to a group of polymers that are known as semi-flexible polymers. We explore these polymer solutions in further detail in the next section.

2.4 Semi-Flexible Polymers

Our initial discussions on polymer solutions, assumed that the polymer could be treated as a freely jointed chain of monomers. However we refined this definition by the inclusion of the persistence length. This accounted for the fact that each monomer was not free to rotate, but on length scales larger than l_p , the motion of the

monomers was uncorrelated. In this section we explore the different bulk properties that arise in polymer solutions due to this increased stiffness. These differences in polymer properties are also seen in our experimental observations.

The introduction of the persistence length creates a ‘stiffness’ in the polymers. These stiffer or semi-flexible polymers are characterized by a rigidity parameter, p , which is defined as $p \equiv 2l_p/d$ where d is the diameter of the polymer (N.B.: for a truly freely jointed chain, d is the monomer diameter). For low values of p , a chain is described as flexible, while for $p \gg 1$ the chains are termed semi-flexible. As the rigidity of the polymer increases it finally approaches a rod-like configuration. A good example of a flexible polymer is Polystyrene ($p=2$) whereas DNA ($p=50$) is more rigid and is described as semi-flexible. This introduction of rigidity leads to a renormalization of the number of links, N , to an effective link number, (see Eq. 2.5), and to a modified second virial coefficient, $\bar{B} = dl_p^2\tau$. Thus we see that a stiff rod like monomer, sweeps out a disk like volume that excludes other monomers.

The properties of polymer solutions can be compactly summarized in a phase diagram in which the solvent quality, τ of the solution is plotted against the polymer volume fraction, $\Phi = cd^3$. A simple picture for flexible polymers is presented in Fig. 2.6. For example, in dilute polymer solutions that lie near the Θ -temperature (Region I), the polymer behaves like a Gaussian coil with radii, R_I which is given by Eq. 2.7. However, far from the Θ -point, the coils appear swollen with a radius,

Region	Osmotic Pressure, Π_p	Correlation Length, ξ / R_g
I	c	$N^{1/2}$
II	c	$N^{3/5}\tau^{1/5}$
IV	$c^{9/4}\tau^{3/4}$	$c^{-3/4}\tau^{-1/4}$
V	c^3	c^{-1}

Table 2.2: The concentration and τ dependence for the different phases of flexible polymer solutions.

$R_{II} \sim v^{1/5}\tau^{1/5}N^{3/5}$. The transition boundary between ideal behavior and swollen coils is defined when the parameter, $z \equiv 2(3/2\pi)^{3/2}N^{1/2}B/d^3 \sim 1$ and this is achieved when $R_I = R_{II}$

As the concentration of links, is increased the polymer enters the semi-dilute regime. Depending on the solvent quality several different regimes emerge. The different phases of the semi-dilute solution, Region IV and V can once again be represented on the phase diagram shown in Fig. 2.6. Concentration increases near the theta point leads to a transition from Region I to Region V. In this weakly fluctuating regime triple collisions dominate and mean field treatments can be used to describe polymer properties. The correlation length and osmotic pressure, scale with concentration as $\xi_V \sim d(cd^3)^{-1}$ and $\Pi_V \sim d^6c^3$ respectively. On the other hand if the polymer solution lies far from the Θ -point, then concentration increases will lead to a transition from Region II to Region IV. At these increased temperatures, scaling

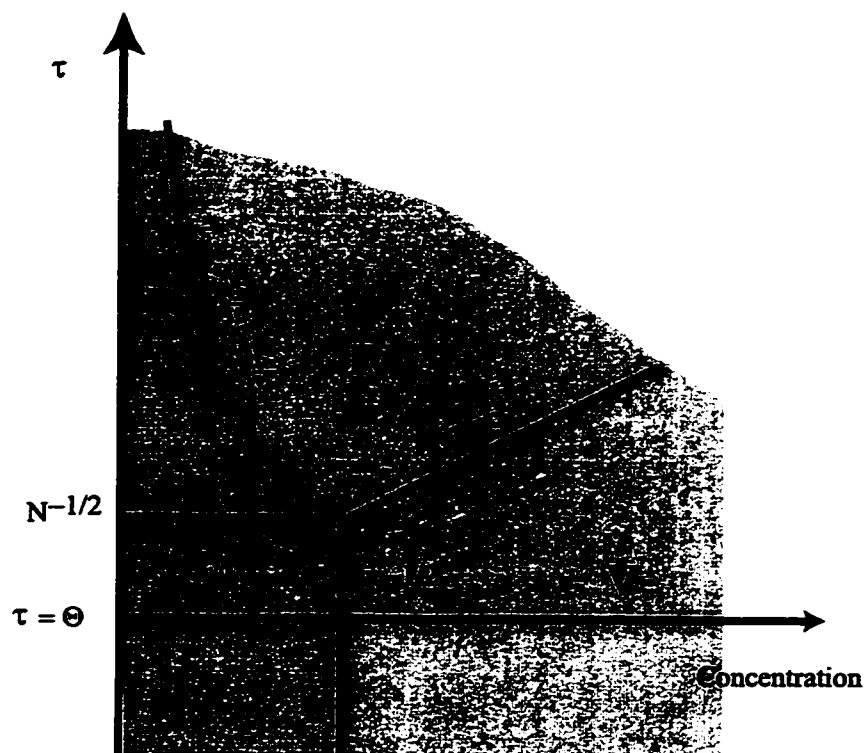


Figure 2.6: A qualitative phase diagram for flexible polymers showing the different solution phases. The horizontal axis represents polymer concentration and the vertical axis represents deviations from the Θ -temperature, τ . The labelled regions are described in detail in the text and tabulated in Table 2.2.

statistics are needed to account for the large concentration fluctuations that arise due to strong repulsion between links. The boundary that delineates the dilute region from the semi-dilute phase is determined by the overlap concentration, $c^* \sim N/R_{II}^3$ which in turn depends strongly on size of the swollen coil. In this phase (Region IV), the correlation length ξ_{IV} scales as $d(cd)^{-3/4}\tau^{-1/4}$ and the the pressure is given by $\Pi_{IV} \sim \tau^{3/4}c(cd^3)^{5/4}$. With further increases in concentration the importance of fluctuations diminishes and the solution properties return to those exhibited in Region V. The crossover is defined by the line, $\Phi = \tau$ which is easily obtained by equating ξ_V and ξ_{IV} or Π_V and Π_{IV} . Table 2.2 provides a summary of the polymer characteristics in these different regimes.

The phase diagram presented in Fig. 2.6 is rarely realizable since polymers are never truly freely jointed. In semi-flexible polymers the inclusion of the rigidity parameter, p , leads to the emergence of additional regimes in the diagram of state [17, 33, 34]. These have been summarized in Table 2.3. Most importantly it leads to the existence of two new semi-dilute regions in the phase diagram (shown in Fig. 2.7), Region VI and VII. In region VII, which lies near the theta point, the polymer can still be described by Gaussian statistics, even though it is entangled. However the number of links is rescaled by the persistence length so, the size is given by, $R_{VII} \sim N^{1/2}p^{1/2}$. Once again it is the overlap concentration that defines the boundary between the

Region	Osmotic Pressure	Correlation Length/ R_g
I	c	$N^{1/2}p^{1/2}d$
II	c	$N^{3/5}\tau^{1/5}p^{1/5}$
IV	$c^{9/4}\tau^{3/4}p^{3/4}$	$c^{-3/4}\tau^{-1/4}p^{-1/4}$
V	c^3	$c^{-1}p^{1/2}$
VI	$c^2\tau$	$c^{-1/2}\tau^{-1/2}p^{1/2}$
VII	c	$N^{1/2}p^{1/2}$

Table 2.3: The concentration and τ dependence for the different phases of semi-flexible polymer solutions.

dilute region, I and the semi-flexible region VII and can be written as

$$c = N^{-1/2}p^{-3/2}. \quad (2.49)$$

The second new region, VI, emerges at the expense of region, IV. Semi-flexibility leads to the narrowing of the region in which fluctuations are important and a dominance of pair wise contacts in the solution. In this new phase the polymer osmotic pressure and the correlation length can be described by mean-field theory[17, 33] and are given by numerically accurate expressions $\Pi_p/k_B T = BN_{\text{eff}}^2 n_p^2$ and $\xi = l_p(6BN_{\text{eff}}n_p)^{-1/2}$ where n_p is the polymer coil concentration given by $n_p = c/(N)$. This regime is bounded by region IV on the low concentration side with the boundary being defined by

$$\tau_{IV \rightarrow VI} \sim cp^3 \quad (2.50)$$

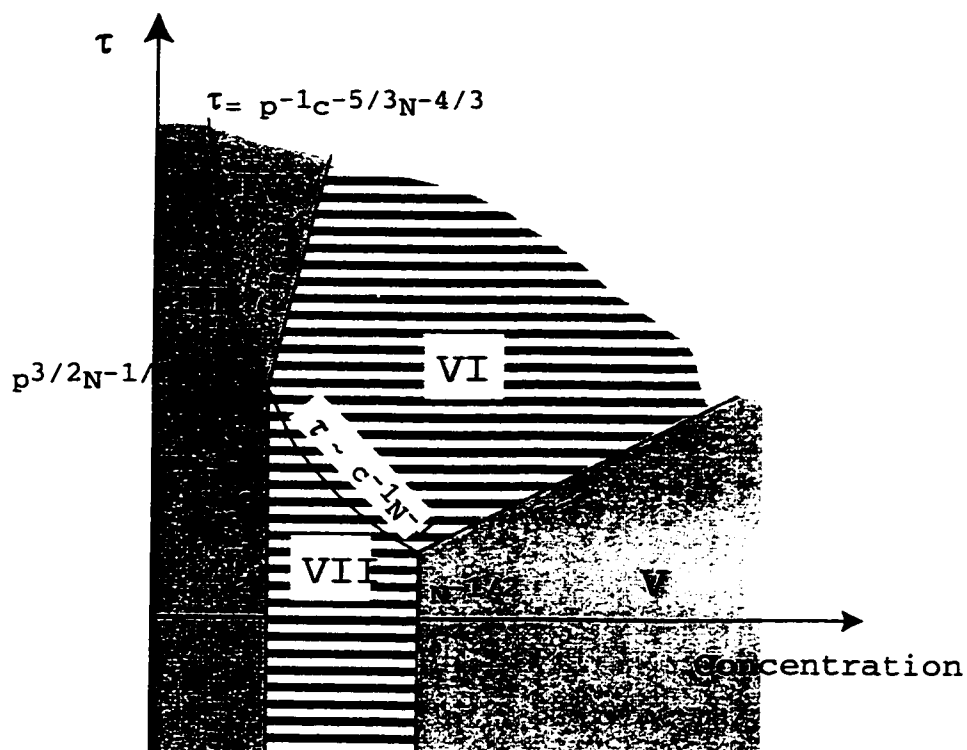


Figure 2.7: A qualitative phase diagram for semi-flexible polymers showing the different solution phases. Once again the horizontal axis represents polymer concentration and the vertical axis represents deviations from the Θ - temperature. The labelled regions are described in detail in the text and tabulated in Table 2.3. The hatched regions represent the new regions that appear in semi-flexible polymer solutions.

On the high concentration end the transition to region III occurs at $c = \tau$. The weakly fluctuating regime (VI), is of particular interest to us since our measurements on DNA, a semi-flexible polymer with $p \sim 50$, indicates that our solution lies in this regime.

The origins of these new regimes can be understood conceptually by looking at the excluded volume interactions. Since the rigidity parameter depends on the link interactions, v through, $p^{-3/2} \sim v/d^3$, we see that any decrease in excluded volume effects ($v \rightarrow 0$) leads to an increase in stiffness. For a stiff polymer the links rarely cross each other and excluded volume interactions are negligible. Increases in concentration that would normally increase chances of link interactions, can be accounted for by a virial expansion. In contrast, for flexible polymers the link interactions increase dramatically with increasing concentration (unless the solution happens to lie near the θ -point) and is not well described by the virial expansion. Thus semi-flexible polymers are always close to ideal.

In Fig. 2.9 we calculate the phase diagram for λ -DNA. We see that Region VI is greatly enhanced, whereas Region IV is reduced to a minimum. In contrast we also plot the phase diagram for a flexible polymer, Polystyrene (see Fig. 2.8). We see that even for polystyrene which is highly flexible, $p \sim 2$, there is an appreciable region in which pairwise interactions are dominant. However the phase space spanned by this region is much smaller than the equivalent region in Fig. 2.9. Our experimental

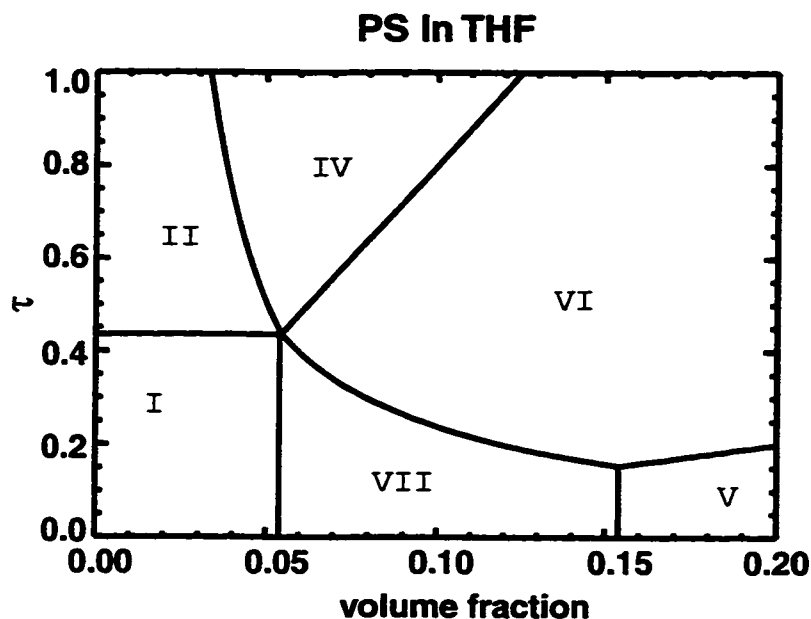


Figure 2.8: The calculated phase diagram for PS in THF(tetrahydrofuran), which has a rigidity parameter, $p=2$. We see that even in polymers that are considered ‘flexible’ there is a significant region (VI) where mean-field predictions can be applied.

observations, presented in the subsequent chapters, confirm the existence as well as the extent of the mean field region which is dominated by pairwise contacts.

2.5 Conclusions

In this chapter we have attempted to define the basics of polymer theory that will be useful in developing polymer depletion models as well as understanding the properties of DNA in solution. The simple random walk model that can be used to describe ideal polymers, was expanded to include the effects of interactions between links. The

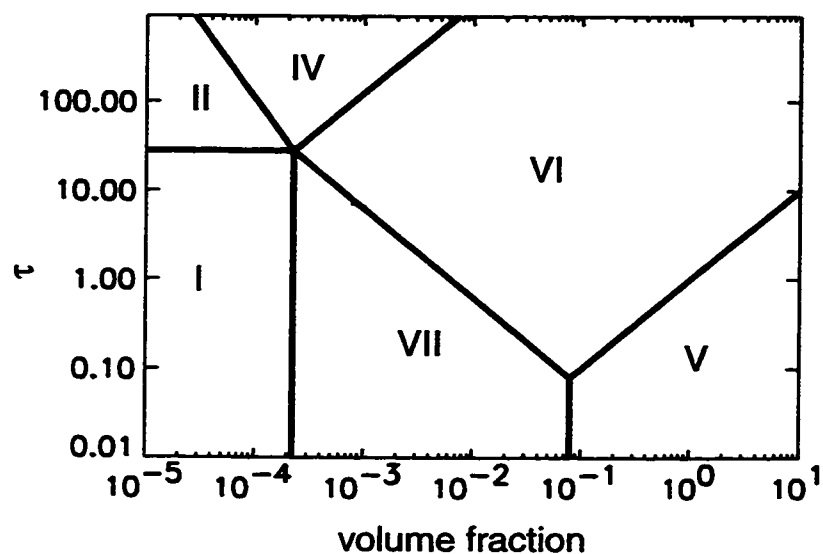


Figure 2.9: The calculated phase diagram for DNA from our measurements. We see that the mean-field region is greatly enhanced. The details are presented in Chapter 5.

next section discussed polymer solutions which contain many polymer coils. Different theories, such as the self-consistent mean field approach and the scaling theory were used to derive the physical observables of such solutions. Finally the effects of chain rigidity in polymer solutions was discussed and compared with properties of completely flexible polymers. In the subsequent chapters we utilize these mathematical formulations to understand our experimental observations.

Chapter 3

Polymer Depletion

Entropic effects play an important role in the physics of colloidal mixtures. Important effects arise when two colloidal species of different sizes interact primarily through hard sphere repulsions. In this case we find that maximizing of entropy of the smaller species in the suspension drives the other towards greater order. The tendency for the larger particle to aggregate is called the depletion effect. The consequences of depletion are of both fundamental as well as industrial interest. For example, depletion effects must be minimized in the production of paint [35, 36, 37], but can be exploited for controlled separation of mixtures [35]. Often these processes involve colloid-polymer mixtures in which the depletion effect is not well understood. In this chapter we explore the entropic attraction that arises between colloidal spheres in the presence of non-adsorbing polymers.

We will review the traditional theory of hard sphere depletion, commonly called the Asakura-Oosawa (AO) model[38, 39]. We also discuss polymer depletion models

derived from a mean-field theoretical approach [40]. The polymer depletion problem has analytical solutions in two different regimes. One regime assumes the colloidal particles can be approximated as point spheres, and the other regime assumes the colloidal particles are represented as infinite walls. We also present a comparison between the mean field approach and the AO Model. Finally we explore the consequences of a distribution of binary mixtures containing a polydisperse distribution of particles and their effect on the depletion model.

3.1 Introduction to Depletion

Mixtures containing hard spheres with different diameters, but without chemical or electrostatic affinity for each other, exhibit a surprisingly rich phase behavior as a result of the size ratio of the two species and their volume fractions. The formation of crystallites, gel-like aggregates and fluid phases is often observed [41, 42, 43]. The underlying physics behind these phase transitions can be understood by considering the forces exerted by the particles on one another. Even though there is no chemical ‘bridging’ between particles, the attractive force between large particles can be accounted for by steric considerations. Particles tend to congregate by what is called entropically driven ‘attraction through repulsion’[44], or more commonly, depletion.

The depletion attraction can be described equivalently by two simple arguments. The first focuses on the kinematics of the collisions [44] between the particles while the

other involves system entropy [38]. A close examination of a binary mixture, in which one species is larger than the other shows that particles are constantly colliding with each other. A sphere that belongs to the larger colloid family, undergoes frequent collisions with the smaller species which produces a fluctuating force on the large particle. However there is no net force on the particle since the forces are balanced in all directions. The physics gets interesting when two of the larger particles are brought close together so that the smaller species cannot penetrate the gap between them. In this case the collisions on the 'outside' of the two large spheres are no longer balanced and this leads to a net attraction between them, as shown in Fig. 3.1.

The depletion attraction can also be understood through an entropy argument [38]. The center of mass of the small spheres cannot get within a small ball radius of the larger particle due to steric considerations. Thus each large sphere is surrounded by a region that is depleted of the smaller species and the size of the region is determined by the radius of the small species. This is shown in Fig. 3.2(a). The small species experience a loss of accessible volume which is equal to the sum of the volume occupied by the large spheres and the depleted region that surrounds them. Once again if two of the larger species are brought within a small particle diameter, the two depleted regions start to overlap as shown in Fig. 3.2(b). The increase in entropy for the smaller species due to the overlapped volume results in an entropic attraction. A similar depletion attraction arises due to the overlap of depleted regions between

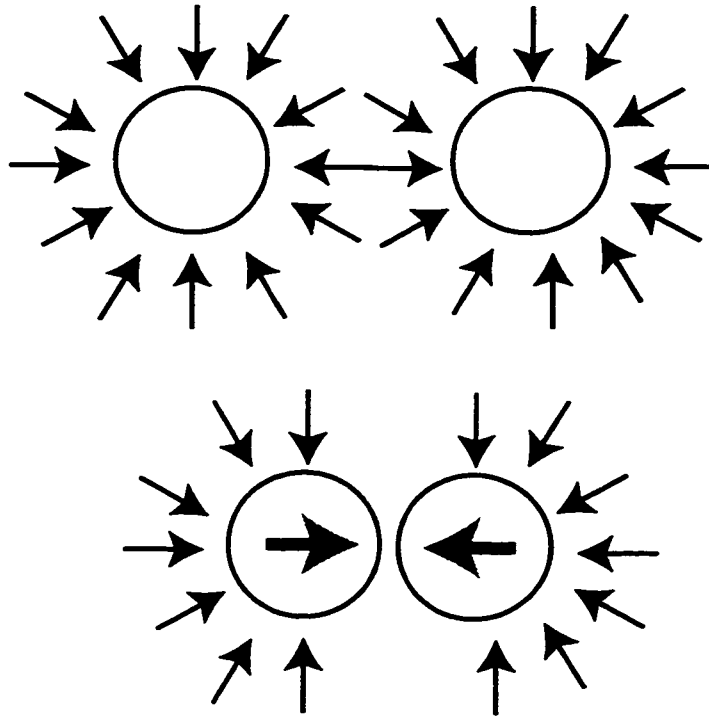


Figure 3.1: Collisions balance out forces on the large sphere when they are far apart however when the mean separation is reduced this leads to a force imbalance which results in a net attractive force.

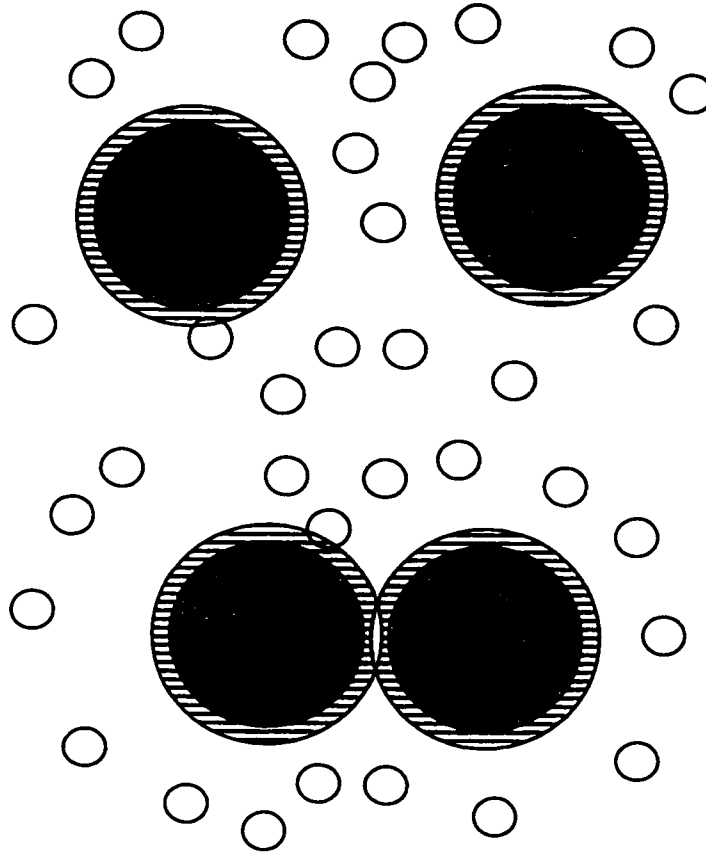


Figure 3.2: Depletion in a binary mixture of colloidal spheres. The hatched region around the larger spheres indicates the depleted region. When the two large spheres are brought close together these regions overlap, thus increasing the volume accessible to the smaller spheres. This leads to a decrease in free energy.

spherical particles and walls, or between two walls [36] .

A quantitative picture of the depletion attraction between two spheres was first realized by Asakura and Oosawa in the late 50's [38, 39, 44]. By simple geometric arguments they were able to calculate a functional form for the interaction energy between two large spheres in a suspension of smaller spheres. The energy is given by

$$U(r) = -\Pi V_{\text{overlap}} \quad (3.1)$$

where Π is the osmotic pressure of the small spheres and V_{overlap} is the overlap volume of the depleted regions shown in Fig. 3.2. This can be easily seen if one adopts an ideal gas picture for the smaller spheres in which their entropy is given by $S = k_B \ln(V_{\text{accessible}})$ where $V_{\text{accessible}}$ is the volume available to the smaller spheres. Then the change in entropy of the small beads, when the larger two particles are brought in contact is given by

$$\partial S = k_B N_s \ln(V_{\text{accessible}} + V_{\text{overlap}}) - k_B N_s \ln(V_{\text{accessible}}) \approx k_B N_s (V_{\text{overlap}}) \quad (3.2)$$

Thus the change in free energy due to the increase in entropy is given by

$$\delta F = -T\delta S = -k_B T N_s (V_{\text{overlap}}). \quad (3.3)$$

For the two sphere geometry the overlap volume is given by the lens like geometry produced where the depleted regions overlap. This then gives an interaction energy which is given by

$$U(r) = -\Pi_s \frac{4\pi}{3} R_s^3 \left(\frac{\lambda}{\lambda-1}\right)^3 \left[1 - \frac{3}{2} \frac{r}{\sigma\lambda} + \frac{1}{2} \left(\frac{r}{\sigma\lambda}\right)^3\right], \quad (3.4)$$

$$\sigma \leq r \leq \sigma + 2R_s,$$

where Π_s is the osmotic pressure of the small beads, R_s is the hard-sphere radius of the small spheres, σ is the diameter of the large sphere and $\lambda \equiv 1 + 2R_s/\sigma$. This expression results from purely geometrical considerations and can foreseeably be applied to all $2R_s/\sigma$, with appropriate changes to the multiplicative osmotic pressure.

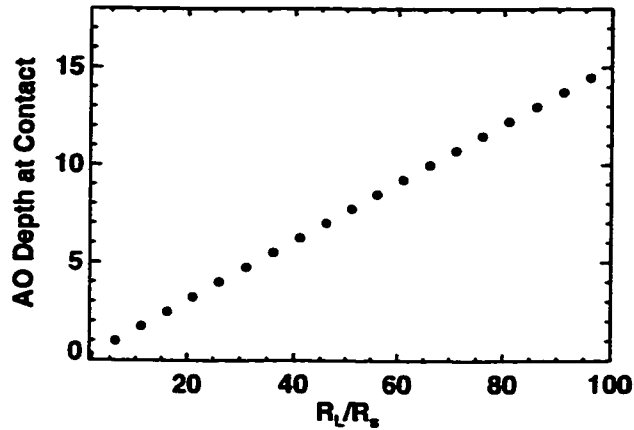


Figure 3.3: The depth of the AO interaction at contact vs. the size ratio of large particle to the small particle, $\sigma/2R_s$.

What is the magnitude of the depletion effect? Can it be measured? The first question can be addressed by looking at the magnitude of the interaction for common colloidal particle sizes. For example, the strength of the contact depletion attraction between $10\mu\text{m}$ and $1\mu\text{m}$ particles, in a suspension where the small sphere volume fraction is 0.1, can be calculated to be $-1.5k_B T$. This is a sizable effect that can be experimentally measured. The magnitude of this interaction can be controlled by varying the size ratio and volume fraction. Fig. 3.3 shows the calculated strength of the AO model (at contact) for different size ratios varying from $\frac{\sigma}{2R_s} = 1$ to $\frac{\sigma}{2R_s} = 100$, at a constant small sphere volume fraction of 0.1. We see that the strength of the interaction increases linearly from $0.15k_B T$ to $15k_B T$, making it a rather sizable effect.

The simplicity of the AO model is appealing, however there are limitations since the model is based on an ideal gas approximation. Effects such as liquid structure that

typically arise in solutions are not accounted for by the AO model. These arise due to neglect of volume interactions that occur amidst the smaller species. This leads to rearrangements and ordering of the small spheres that ultimately influence the interaction of the larger spheres. Measurements [45] and calculations [46] show that liquid structure effects can lead to repulsive barriers and oscillations in the depletion attraction.

3.2 Polymer Depletion

So far we have focused on the depletion effect caused by a binary mixture of hard spheres. How does this change if we replace one of the components with polymer coils? From our discussions in Chapter 2 it is obvious that a polymer coil is very different from a hard sphere. Is it possible to adapt the considerations discussed in the previous section to explain polymer depletion? This is an important question, since attempting to understand polymer depletion is not only of fundamental interest but of technological interest as well. Polymers are widely prevalent in industrial processes as well as in biological systems. Paint [36], oil recovery [25, 47] and paper manufacturing all use depletion (and primarily polymer depletion) to achieve their end products. The new phases recently observed in colloid-polymer mixtures [41, 42] promise to give rise to new novel processing techniques and materials. In biological systems, red blood cell aggregation is believed to be induced through depletion forces

that result from increases in protein concentration [48]. In addition depletion forces are believed to play an important role in altering shapes of vesicles [49, 50] and lipid membrane adhesion. Thus an understanding of the fundamental issues regarding this interaction is of utmost importance.

The depletion model discussed in the previous section was first proposed by Asakura and Oosawa [38] for a hard sphere-polymer system. The result relies on the fact that a polymer coil can be modeled as an effective hard sphere, whose radius is approximately given by the radius of gyration, (Eq. 2.7). This argument ignores the conformational degrees of freedom of the polymer coil. For example, the AO model ignores the ability of the polymer to penetrate the gap between the two large colloids, even when the depleted regions overlap. This could lead to an overestimation of the depletion effect. Moreover it ignores the polymer-polymer interactions leading to further exaggerations of the depletion force [51]. Thus the validity of the Asakura-Oosawa case is limited to the regime in which the polymeric solution is very dilute and it is possible to model the polymer as an ideal gas of hard spheres. Increasing the polymer-polymer interactions or increasing the polymer concentration into the semi-dilute region where polymer coils are entangled leads to a breakdown of the hard-sphere model. These shortcomings have been the focus of many theoretical works.

Theories attempting to overcome the limitations of the AO model usually include

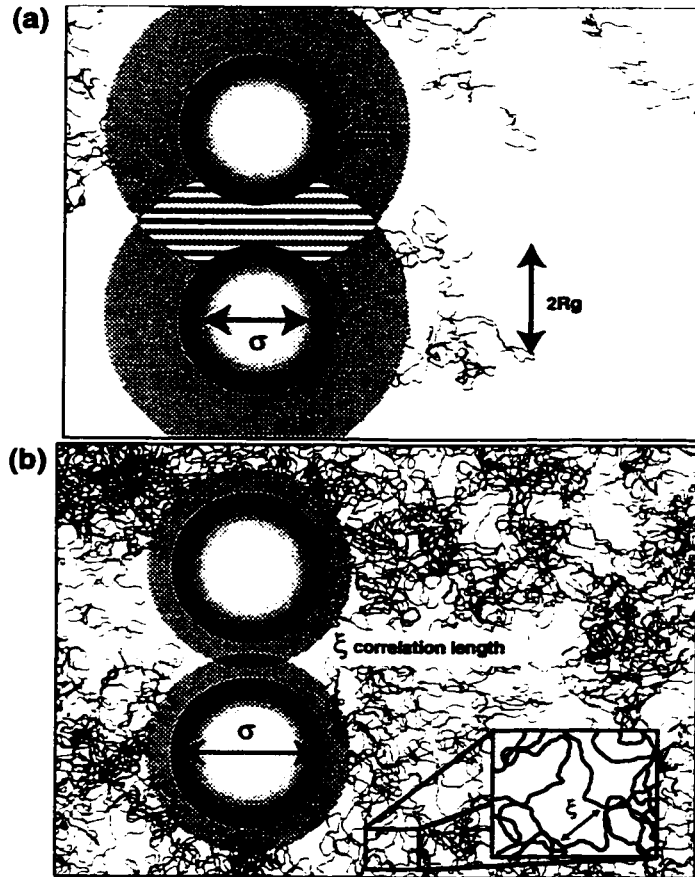


Figure 3.4: Polymer depletion in the (a) dilute and (b) semi-dilute regime. The depletion region is shaded in grey and the hatched region corresponds to the increase in volume accessible to the polymers.

refinements by attacking the problem from a mean-field self-consistent approach [40, 52, 53]. The initial mean field approach was first put forth by Joanny *et. al.* [40] for depletion in a flat plate geometry. The results were then cast onto a pseudo-scaling theory to calculate interaction energies. We present the details of this calculation in Section 3.4, but adapt it to derive results solely in the mean-field limit. Recent studies have expanded on this result by including polymer-polymer interaction terms and accounting for the deformability of the polymer. Schaink and Smit [54] include polymer configurations, excluded volume interactions between polymer links as well as hard-sphere correlations through the Carnahan-Starling approximation, in their depletion force calculations. Eisenriegler *et. al.* [55] also explore mean-field theoretic descriptions of polymer depletion with colloids that have cylindrical geometry. Odjik [52, 53] and DeGennes [56] explored a pseudo-scaling theory calculation similar to the original Joanny treatment with particles that are a lot smaller than the polymers. The last two studies address issues that might arise in semi-dilute solutions [57, 58] whereas the first few [54, 55] calculate depletion effects in dilute polymer solutions.

Other attempts to solve the depletion interaction in polymer solutions have used a variety of techniques ranging from scaled particle theory to computer simulations. Integral equation methods have been employed to show that excluded volume effects between polymer links lead to a reduction in the depletion interaction [51, 59]. Sophisticated computer simulations [60] have been used to compare and contrast the results

predicted by these different approaches and calculate the importance of the different parameters involved in polymer depletion. In addition, the depletion interaction has been studied for polymer molecules that can be approximated as long rigid rods [61]. More recently the effects of anisotropic polymer link distributions have been explored in detail [62]. In this chapter we focus on two simple approaches that enable us to interpret the qualitative features for the data presented in this thesis.

3.3 Correlation Hole Picture

A physical picture of the depletion attraction can be obtained by looking at two point particles immersed in a polymer solution [17]. Since the non-adsorbing polymers are repelled by the particles, insertion of a single particle leads to the formation of a depleted polymer cavity around it. This region is often called a correlation cavity. Insertion of the second particle also leads to the formation of a similar correlation cavity. The second particle is attracted to the region of low polymer concentration that surrounds the first particle. Thus the presence of a depletion cavity around each particle produces an effective attraction.

DeGennes [16] presents a simple qualitative argument for this attraction through a toy lattice-model picture. This is illustrated in Fig. 3.5. In (a) the black dots represent the immersed particles which, when far apart, allow the polymer to occupy all four available lattice sites surrounding the particle. At each one of these sites, a

dimer is restricted to position itself in three different orientations. The entropy of the system is given by the total entropy minus the loss in entropy at these restricted sites. Thus the loss is proportional to eight, since there are eight available sites. On bringing the particles closer than the polymer coil size, the number of available sites is reduced to six. This leads to an increase in entropy, as there is a loss in entropy only at six sites. This causes a subsequent decrease in free energy of the system.

An analytical solution for the potential of mean force between these two particles can be obtained in the limit that the two particles are infinitely small spheres, i.e. they can be mathematically represented by delta functions [17]. The increase in free energy of the system due to the addition of the two particles, can be written as

$$F_{add} = u(r_1 - r_2) + \int (c_0 + \delta c(x))u(x - r_1)d^3x + \int (c_0 + \delta c(x))u(x - r_2)d^3x. \quad (3.5)$$

The first term represents the bare interaction between the spheres and only depends on the inter-particle spacing, $r = (r_1 - r_2)$. This could be just a hard core repulsion or it could also include electrostatic components. The second and third terms represent the polymer interaction with the i th sphere i.e., $u(x - r_i)$, and is weighted by the local polymer concentration, $c(x) = c_0 + \delta c(x)$. The cost in energy associated with inserting one particle into the suspension is given by $c(x)u(x - r_i)$. The additional energy cost, $\delta c(x)u(x - r_i)$, results from perturbations in the concentration which are introduced by the presence of the second sphere. Since we are interested in free energy changes due to these perturbations we can simply subtract off the single particle energies,

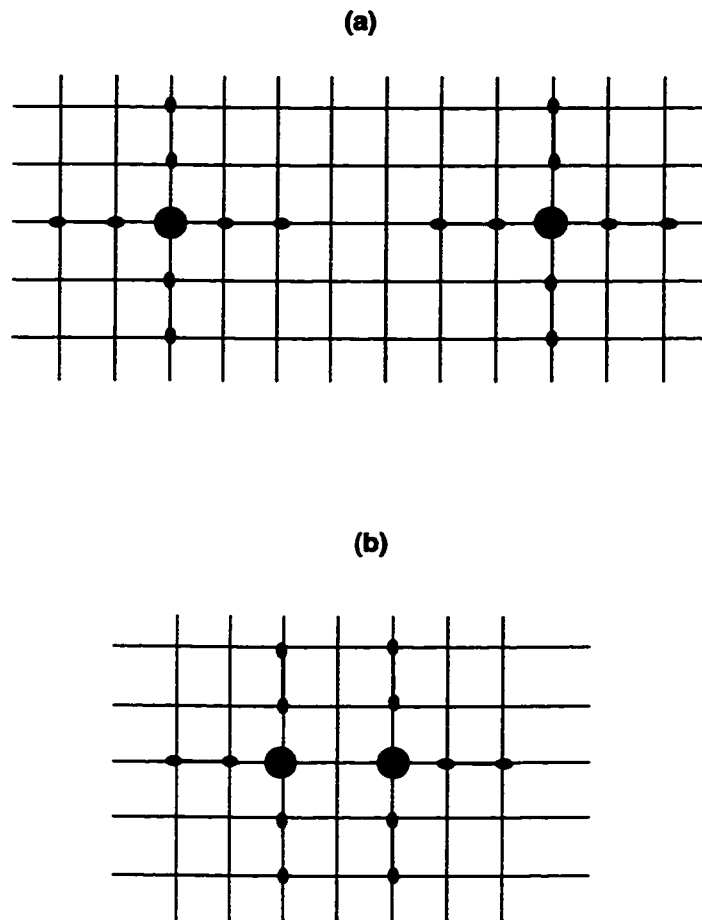


Figure 3.5: The lattice model explaining the increase in entropy. In (a) we see that the conformation of the dimer (shown in grey) is restricted at 8 sites by the presence of the two particles. However, when the particles are closely spaced (b), there are only six sites that restrict the dimer configuration, thus leading to an overall increase in entropy. [16]

which gives the free energy of interaction as

$$F_{int} = u(r_1 - r_2) + \underbrace{\int \delta c(x) u(x - r_1) d^3x}_{F_1} + \underbrace{\int \delta c(x) u(x - r_2) d^3x}_{F_2} \quad (3.6)$$

The free energy can be minimized (see Appendix B), to once again yield an Ornstein-Zernicke like equation, except that now there are two source terms due to the presence of the two particles. The resulting differential equation for polymer concentration fluctuations is,

$$\nabla^2 \delta c - \frac{\delta c}{\xi^2} = \frac{12c_0}{k_B T l^2} [u(x - r_1) + u(x - r_2)] \quad (3.7)$$

where ξ is the correlation length and l is the length of a polymer link. This closely resembles the electrostatic analog that can be found for calculating Debye screening lengths. We can adopt similar techniques and solve for $\delta c(x)$, using the Green's function that was calculated in Eq. 2.22. This is done easily in momentum space where

$$\delta c(k) = G(k) \rho(k). \quad (3.8)$$

Here $G(k)$ is the momentum space Green's function and $\rho(k)$ is the Fourier transform of the source term, i.e. the right hand side of Eq. 3.7. The momentum space Green's function, $G(k)$ is given by

$$G(k) = \frac{\xi^2}{1 + \xi^2 k^2}. \quad (3.9)$$

and the Fourier transform of the source term is given by

$$\rho(k) = \frac{12c_0}{k_B T l^2} \int \frac{d^3 x'}{(2\pi)^3} e^{-ikx'} [u(x' - r_1) + u(x' - r_2)] \quad (3.10)$$

We can combine Eq. 3.9 and Eq. 3.10 to find an expression for the concentration fluctuation in real space as

$$\begin{aligned} \delta c(x) &= \int \frac{d^3 k}{(2\pi)^3} e^{ikx} \delta c(k) \\ &= \frac{12c_0 \xi^2}{k_B T l^2} \int \frac{d^3 k}{(2\pi)^3} e^{ikx} \int \frac{d^3 x'}{(2\pi)^3} e^{-ikx'} \frac{[u(x' - r_1) + u(x' - r_2)]}{1 + \xi^2 k^2} \end{aligned} \quad (3.11)$$

If we rewrite the interaction energy term as $e^{-ik(x'-r_i)} e^{-ikr_i} u(x' - r_i)$ and redefine the Fourier transform of the polymer-sphere interaction potential

$$u_k \equiv \frac{1}{k_B T} \int \frac{d^3 x'}{(2\pi)^3} e^{-ik(x'-r_i)} u(x' - r_i) \quad (3.12)$$

then we can rewrite Eq. 3.11 compactly as

$$\delta c(x) = \frac{12c_0 \xi^2}{l^2} \int d^3 k e^{ikx} \frac{[u_k e^{-ikr_1} + u_k e^{-ikr_2}]}{1 + \xi^2 k^2}. \quad (3.13)$$

In the above equation we have assumed that the particles are identical and thus have the same interaction potential, i.e. $u(x' - r_1) = u(x' - r_2)$.

Having solved for the perturbations in the concentration we now return our attention to calculating the interaction free energy, F_{int} . Inserting the above expression into the interaction free energy expression Eq. 3.6, and looking closely at just one of the polymer-particle interaction energy terms, F_1 , gives us

$$F_1 = -\frac{12c_0 \xi^2}{l^2} \int d^3 x \int d^3 k e^{ikx} \frac{[u_k e^{-ikr_1} + u_k e^{-ikr_2}]}{1 + \xi^2 k^2} \times \quad (3.14)$$

$$k_B T \int \frac{d^3 k'}{(2\pi)^3} e^{i k' (x - r_1)} u_{k'}$$

Rearranging the terms and using the identity $\int d^3 x e^{i(k+k')x} = (2\pi)^3 \delta(k+k')$ we can rewrite the above equation as

$$F_1 = -\frac{12c\xi^2 k_B T}{(2\pi)^3 l^2} \int d^3 k \frac{1 + e^{i k (r_1 - r_2)}}{1 + k^2 \xi^2} |u_K|^2 \quad (3.15)$$

We see that as the inter-particle separation goes to infinity the second term rapidly oscillates and its integral approaches zero. However, the first term contributes to the free energy and must be subtracted off to ensure that at large separations there is no free energy of interaction. Physically, this term represents the free energy required to insert two independent particles far away from each other. Finally by including interaction terms due to both spheres, i.e. F_1 and F_2 , as well as the bare hard-sphere interaction term the total free energy of interaction can be written as

$$F_{int} = u(r) - 2 \times \left(\frac{12c_0 \xi^2 k_B T}{(2\pi)^3 l^2} \right) \int d^3 k \frac{e^{i k (r)}}{1 + k^2 \xi^2} |u_K|^2 \quad (3.16)$$

where r has been used as the inter particle spacing, $r_1 - r_2$. The change in the bare interaction energy manifests itself as a negative term indicating that the interaction is attractive.

To calculate the functional form for F_{int} , we need to insert an explicit polymer-sphere interaction potential. This can be done for a few simple cases. If we assume that the polymer-particle interaction is short range, i.e. a constant in k space, then

the integral is easy to perform and the resulting free energy is given as

$$F = u(r) - \frac{6c_0 k_B T}{\pi l^2} \frac{e^{-r/\xi}}{r} \quad (3.17)$$

We see that free energy of interaction has a Yukawa-like form with a range that is determined by the correlation length ξ .

3.4 The Infinite Plate Model

The depletion problem in concentrated polymer solutions has been approached from the other limit as well, i.e. the limit in which the particles are replaced by two walls. Determining the concentration distribution in this geometry through a mean field theoretic approach allows for the calculation of the depletion potential. This approach was first put forth by Joanny *et. al.* [40] who calculated a monomer density profile and adopted the results to include scaling predictions. Here we present a complete mean field description that is extended to account for spherical geometries.

The problem of calculating a density profile is analogous in many ways to solving for the wavefunction of a particle in an infinite well. The coherent superposition of amplitudes of the different paths followed by polymer links is given by, $\psi(r)$ in the limit of ground state dominance. The polymer link wavefunction satisfies the Schrödinger-like equation discussed in Chapter 2, Section 2.4. Since the infinite wall geometry reduces the problem to a single dimension we can rewrite Eq. 2.25 as

$$-\frac{l^2}{6} \frac{d^2 \psi}{dz^2} + v|\psi|^2 \psi = \epsilon \psi \quad (3.18)$$

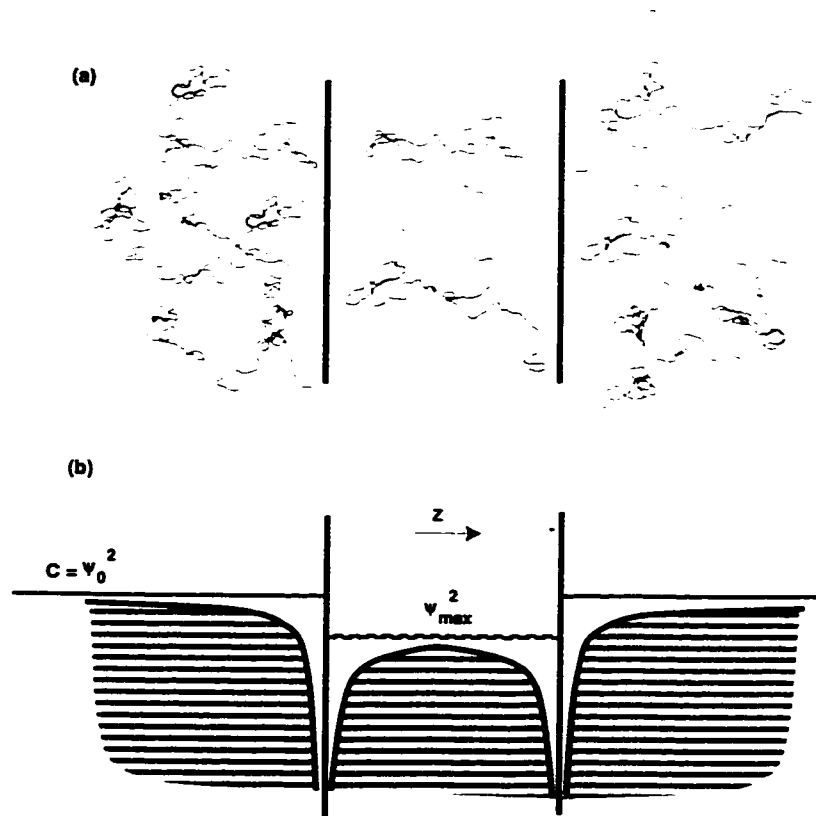


Figure 3.6: The schematic of the wall geometry used to calculate the depletion interaction. The bottom picture shows the concentration profiles calculated in the different regions [40].

where l is the polymer link length, v is the excluded volume parameter that parameterizes link interactions, and ϵ is the eigenvalue of the ground state wavefunction. We have also used the fact that the mean field interaction potential $U(r) = v\epsilon(r) = v\psi^2$ (Eq. 2.21). The geometry can be further exploited by recognizing that the concentration distribution should be symmetric around the center plane. This implies that the $\partial\psi/\partial z = 0$ at $z = D/2$. In addition the wavefunction, ψ , has to go to zero at the walls. Eq. 3.18 can be solved by multiplying through by $\partial\psi/\partial z$ and integrating by parts. For example,

$$\int_0^{D/2} dz \left(\frac{\partial\psi}{\partial z} \right) \frac{d^2\psi}{dz^2} = \left(\frac{\partial\psi}{\partial z} \right)^2 \Big|_0^{D/2} - \int dz \left(\frac{\partial\psi}{\partial z} \right) \frac{d^2\psi}{dz^2} \quad (3.19)$$

$$\int dz \left(\frac{\partial\psi}{\partial z} \right) \frac{d^2\psi}{dz^2} = -\frac{1}{2} \left(\frac{\partial\psi}{\partial z} \right)^2$$

Similarly, we see that $\int_0^{D/2} dz \frac{\partial\psi}{\partial z} \psi^3 = \frac{1}{4} \psi^4 \Big|_0^{D/2}$ and $\int_0^{D/2} dz \frac{\partial\psi}{\partial z} \psi = \frac{1}{2} \psi^2 \Big|_0^{D/2}$. Assuming a value of ψ_{max} at $z = D/2$, and using the fact that far from the wall, $\epsilon = v\epsilon_0 = v\psi_0^2$ (ϵ_0 is the bulk concentration), yields

$$\frac{l^2}{6} \left(\frac{\partial\psi}{\partial z} \right)^2 + v \left(\frac{\psi_{max}^4}{4} - \frac{\psi^4}{4} \right) = v\psi_0^2 (\psi_{max}^2 - \psi^2) \quad (3.20)$$

The value of the maximum concentration between the walls, ψ_{max}^2 is lower than the bulk value, ϵ_0 , and its value changes as the spacing between the walls is changed. The geometry, along with the expected concentration profiles is shown in Fig. 3.6. The full solution to the above equation is given in terms of elliptical integrals and can be

found in Ref.[40]. However for small z , $\psi \rightarrow 0$, and Eq. 3.20 reduces to

$$\left(\frac{\partial\psi}{\partial z}\right) = \psi_0^2 \sqrt{\frac{6v}{l^2} \left(\frac{\psi_{max}^4}{2\psi_0^4} - \frac{\psi_{max}^2}{\psi_0^2}\right)} \quad (3.21)$$

allowing us to obtain an explicit expression for the density profile. Integration of the above equation yields

$$\psi^2 = z^2 \frac{2c}{\xi^2} (\eta^2 - \eta^4), \quad 0 \leq z \leq D/2 \quad (3.22)$$

where $\eta \equiv \psi_{max}^2/2\psi_0^2$ and $\xi^2 = l^2/6vc_0$.

The polymer concentration distribution, $\psi(r)$ can be used to calculate the free energy of the system which is given by Eq. 2.29. We can look at the change in free energy per unit area which can be written as [40]

$$\mathcal{F} = \int [F(\psi) - F(\psi_0)] dz = \int dz \left[\frac{l^2}{6} \left(\frac{d\psi}{dz}\right)^2 + \frac{1}{2}v\psi^4 - \frac{1}{2}v\psi_0^2\psi^2 \right] \quad (3.23)$$

where $F(\psi_0) = \frac{1}{2}v\psi_0^2\psi^2$ is the unperturbed free energy (N.B.: we have ignored the translational entropy associated with the links). The change in free energy can be calculated by utilizing the full solution to Eq. 3.20, the details of which can be found in Ref.[40]. The change in free energy can be written as

$$\mathcal{F} = \frac{k_B T c_0 l^2}{6\xi} f(z/2\xi) \quad (3.24)$$

where the function $f(z/2\xi)$ is found by integrating the full solution to Eq. 3.20[40].

The graphical solution is reproduced in Fig. 3.7.

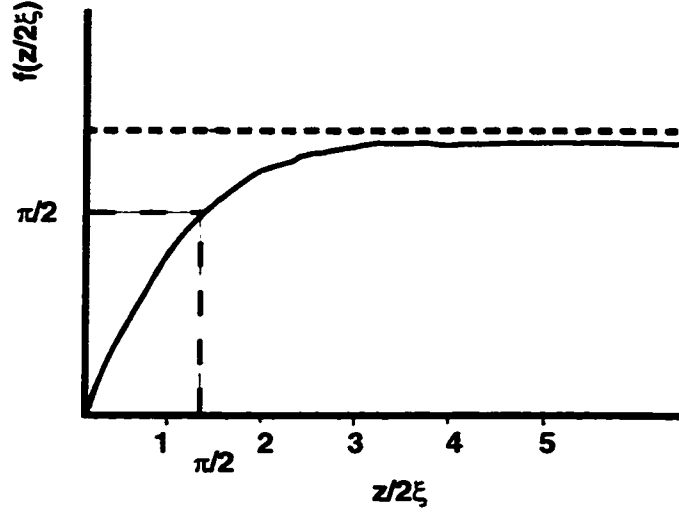


Figure 3.7: The function $f(z/2\xi)$ as the distance between the plates is changed.

We explore two regimes of the free energy change that are of interest. When the plate spacing is smaller than the correlation length ($z \leq \pi\xi$) the function approaches a linear form as is indicated in Fig. 3.7. The free energy, \mathcal{F} , can be written as,

$$\mathcal{F} = \frac{k_B T c_0 l^2}{6\xi} \frac{z}{2\xi} \quad z \leq \pi\xi \quad (3.25)$$

On the other hand when the plates are moved far apart, \mathcal{F} approaches a constant value which can be calculated to be

$$\mathcal{F} = \frac{1.89 c_0 l^2}{6\xi}. \quad z \geq \pi\xi \quad (3.26)$$

Thus we see that at distances which are less than the correlation length, the force is a constant but as the separation between the plates exceed $\pi\xi$ they do not feel each other, since the free energy is a constant. This is an important result for two reasons. It gives us a length scale that determines the free energy of interaction and it gives

us a quantitative description of the depletion forces we would expect to see in these kind of systems.

3.5 Large Sphere Interactions

The above analysis provides us with a mean field picture of depletion layers near a wall in the presence of non-adsorbing polymers. However our interest lies in determining the free energy of interaction when the walls are replaced by colloidal spheres. It is possible to adapt the solution of the wall geometry to that of two large spheres via the Derjaguin approximation [63]. In this approximation the sphere is divided into slices, and it is assumed that a slice from one sphere interacts with a slice on the second sphere in much the same way as two infinite planes. This leads to the condition that the spheres should be large when compared to the characteristic size of the polymers in the background fluid. The total interaction energy between the spheres can be calculated by summing up the contributions from the different slices. This is depicted in Fig. 3.8.

Within this approximation, the free energy calculated in the previous section can be used to calculate the two sphere interaction in concentrated polymer solutions. We ignore any effects of *slices* that are separated by more than $\pi\xi$ and use Eq. 3.25 to write down the surface free energy as

$$\mathcal{F} = \frac{k_B T c_0 l^2}{12\xi^2} (\pi\xi - \sigma - r) \quad (3.27)$$

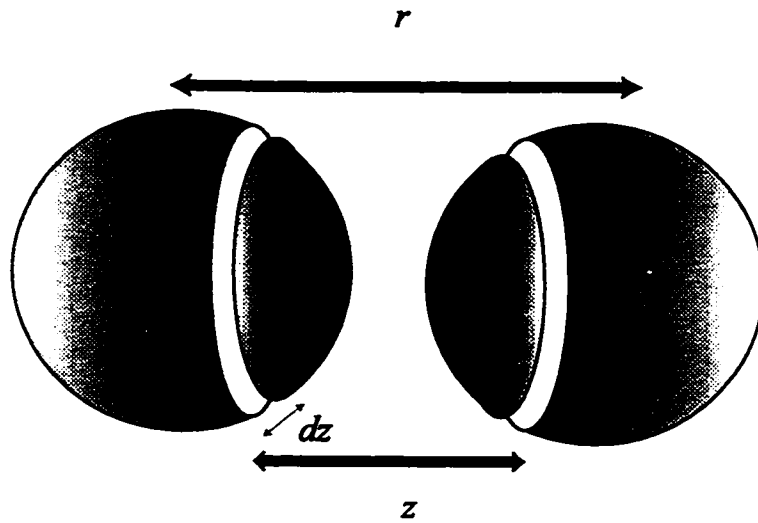


Figure 3.8: The Derjaguin approximation. Two slices separated by z interact with each other. The contributions from all the slices can be added up to calculate the free energy. This relies on the fact that the characteristic polymer size is much smaller than the diameter of the beads.

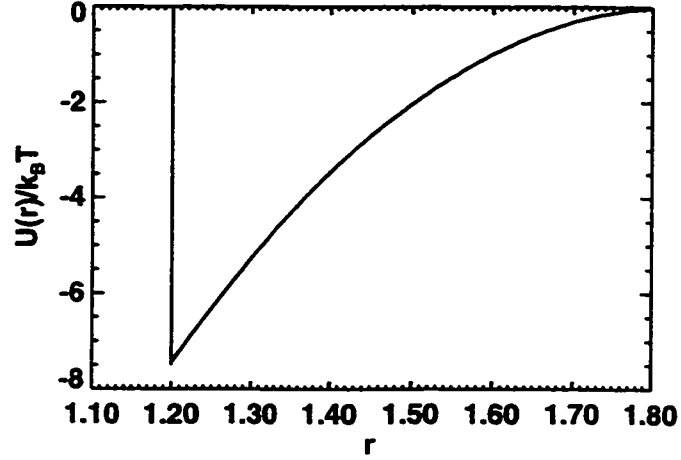


Figure 3.9: The free energy of interaction predicted by Eq. 3.28. A large sphere diameter of $\sigma = 1.2$ units is used along with a correlation length, $\xi = 0.2$ units.

The energy dependence is still linear in separation, however by adding a constant, $k_B T c_0 \frac{l^2}{12\xi^2} (\pi\xi - \sigma)$ it is ensured that there are no contributions when $r \geq \pi\xi$. Here r represents the center-center separation of the two spheres, and σ is the diameter of the large spheres. We can calculate the total free energy by simply integrating over each contributing slice,

$$\begin{aligned}
 F &= k_B T c_0 \int dr \frac{l^2 \sigma}{24\xi^2} \pi (\pi\xi - \sigma - r) \\
 &= k_B T c_0 \frac{l^2}{24\xi^2} \pi \frac{\sigma}{2} (\pi\xi - \sigma - r)^2
 \end{aligned} \tag{3.28}$$

The free energy is valid from contact, where $r = \sigma$ to the point when the two spheres are separated by $\pi\xi + \sigma$. A plot of the free energy vs. inter-particle spacing is shown in Fig. 3.9.

The multiplicative prefactor in Eq. 3.28 can be rewritten by recalling that in

the mean field theory approximation, the osmotic pressure, Π_p , of the polymer is related to its correlation length through, $\Pi_p = k_B T / \xi^4$ (see Section. 2.5). Using this relationship along with the fact that the background concentration, $c_0 \propto 1/\xi^2$, allows us to rewrite Eq. 3.28 as

$$F = \Pi_p \left(\pi \frac{\sigma}{2} (\pi \xi - \sigma - r)^2 \right) \quad (3.29)$$

The free energy is once again proportional to an osmotic pressure times a geometric factor.

We have presented two approaches that can be used to solve the problem of depletion forces between two particles in a semi-dilute polymer system. One of the approaches assumes point-like particles with short range polymer-particle interactions which results in a free energy of interaction which has a Yukawa-like form. This can be extended to include longer range electrostatic interactions between the polymer and the particle. The second method approaches the problem from the opposite end. An infinite plate geometry is reduced to a large sphere approximation. Both these approaches provide a quantitative description of depletion in polymer solutions within the mean-field framework.

Our experimental observations lie in a regime where the characteristic size of the polymer and the colloidal particle are comparable. Both the theoretical approaches discussed here do not provide precise predictions for this regime, even though they do give us a qualitative feel for the depletion interaction. Further theoretical treatments

are needed in order to understand the differences that might arise in this regime. In the next section we discuss the possibility of using the heuristic Asakura-Oosawa model to predict depletion effects in this regime.

3.6 Asakura-Oosawa Model vs. Mean-Field Predictions

The widely accepted Asakura-Oosawa model successfully accounts for depletion in dilute polymer-colloid mixtures but what happens as the polymer concentration is increased? Do we have to abandon that picture once we move into a crowded macromolecular environment? The answer is no. The field theoretic picture presented in Section 3.5, can be shown to be equivalent to the AO model in the limit of large spheres, $\frac{\sigma}{\xi} \gg 1$. We find that we can extend the use of the simple minded picture that is easy to grasp into the semi-dilute polymer solution. The extent of the depletion layer is now determined by the correlation length of the polymer in solution as opposed to its radius of gyration.

The equivalence can be seen by expanding the AO model around $\sigma\lambda$, which is the sum of the diameters of the two species. At this point the potential approaches zero and Taylor expanding yields only second and third order terms. This allows us to rewrite Eq. 3.4 as

$$F_{AO} = -\Pi_p \frac{\pi}{4} \sigma \lambda \left[(r - \sigma\lambda)^2 + \frac{1}{3\sigma\lambda} (r - \sigma\lambda)^3 \right] \quad (3.30)$$

Comparing Eq. 3.29 and Eq. 3.30, in the limit that $\sigma \gg 2R_p$ shows that the two

models are identical to second order provided we identify R_p with $\pi\xi/2$. The importance of the third order term in Eq. 3.30 diminishes as the particle-polymer size ratio increases since R_p/σ approaches zero as does the ratio of the third order term to the second order term, i.e $(r - \sigma\lambda)/3\sigma\lambda \rightarrow 0$. The multiplicative prefactor, $\sigma\lambda$ is also reduced to σ since in the large sphere limit $\lambda \rightarrow 1$.

In addition to confirming the validity of the AO Model in concentrated polymer solutions, the above comparison also provides useful insight into depletion in the semi-dilute regime. In the semi-dilute region the depletion cavity is determined by the correlation length and not the radius of gyration. The polymer solution can be viewed as a close packed system of ideal spheres of size ξ , that give rise to the depletion effect. However, unlike concentrated hard sphere solutions, liquid structural effects are not important since polymeric volume fractions are still very low.

The mean-field treatment of polymer solutions, is valid in the limit in which the colloidal particles are much larger than the polymer coils. As the size of the two species becomes comparable this description breaks down. By comparing the AO model with the mean-field picture we can explore the differences between the two models when we get to ratios in which $\sigma \sim \pi\xi$. Since the Asakura-Oosawa model relies on a geometrical overlap factor the form of the potential should remain unchanged even when the colloidal spheres are smaller than the correlation length. As the size of the bead approaches ξ we expect that the third order term in Eq. 3.30 will become

important and the functional form of the potential will reflect this change. This would imply that the depletion attraction can no longer be described by the quadratic dependence seen in Eq. 3.29 and higher order terms would be needed. However the Asakura-Oosawa model is phenomenological and first principal derivations as well as experiments are needed to confirm its validity in this regime.

3.7 Depletion in Different Polymer Phases

We have seen that the depletion potential depends on two polymeric parameters; the osmotic pressure exerted by the polymer coils and either the radius of gyration or the correlation length of the polymer coils. Both these parameters in turn depend upon the concentration of the polymer solution. In this section we expand the predictive powers of the depletion model to encompass the wide variety of phases that arise in the polymer solutions as the flexibility parameter, solvent quality and the polymer concentration is varied (see Section 2.5). These different regimes also lead to differences in the scaling of the osmotic pressure and the characteristic size of the polymer as the polymer density is varied. This in turn affects the strength of the depletion attraction. We include these different scaling behaviors in the AO model to predict differences that would arise in the depletion interaction.

In the dilute regime the range of the depletion interaction is determined by the radius of gyration of the polymer coil. However from our discussions in Section 2.5

we saw that the radius of gyration of an isolated coil varied with solvent quality. For ideal coils the depletion range would depend on the $R_g^2 \sim Nl^2$ of the ideal polymer chain, but as repulsive link interactions became important the swollen coil size, (Eq. 2.10), would determine the interaction range. The osmotic pressure would depend linearly on the polymer coil density and in regions where interactions were strong higher order virial terms would have to be included.

In the semi-dilute regime the characteristic size, ξ , changes as the concentration is varied. For the region in semi-flexible polymers where pair contacts dominate (Region VI), the concentration dependence for the correlation length is given by $\xi \sim c^{-1/2}$, and the osmotic pressure is related to the concentration through, $\Pi \sim c^2$. This leads to modifications in the concentration dependence of the AO model. We can express the AO model in terms of polymer concentration as,

$$\frac{U(r)}{k_B T} = -\frac{\pi}{36} \left(\frac{c}{6B}\right)^{1/2} (\lambda_{MF}^3 - \frac{3}{2} r \sqrt{6Bc} \lambda_{MF}^2 + \frac{1}{2} \sqrt{6Bc} r^3) \quad (3.31)$$

where c is the monomer concentration, B is the second virial coefficient and λ_{MF} is defined as $\lambda_{MF} \equiv (\sigma \sqrt{6Bc} + l)$. Equation 3.31 enables the depletion interaction to be calculated as a function of polymer concentration and the resulting potential is shown in Fig. 3.10 (solid line).

Similar expressions for the depletion potential can be obtained for other polymer phases discussed in Section 2.5. The differences in the interaction energies that would arise in these regimes are illustrated in Fig. 3.10. We see for a fixed concentration,

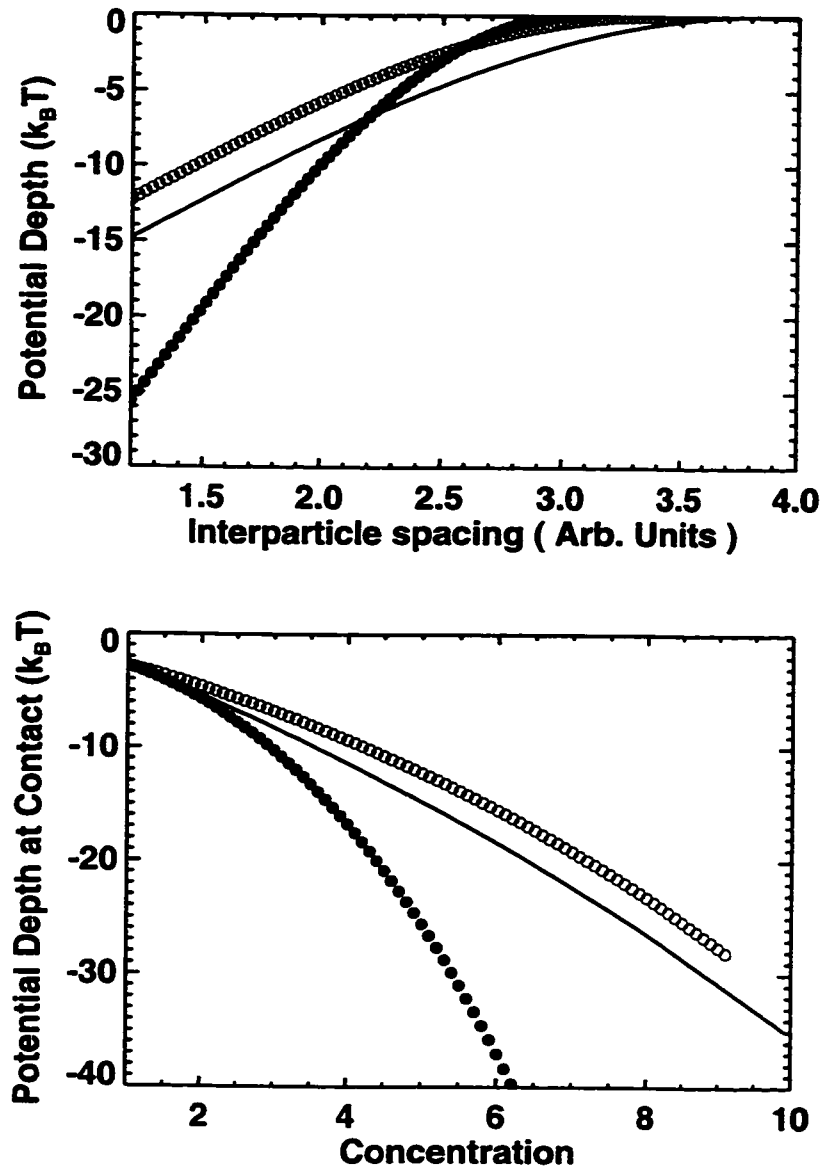


Figure 3.10: In (a) we see the depletion potentials in the different polymer phases. The potentials are calculated by using an AO model but including the scaling characteristics for each region. The solid line represents the potential in Region VI, the open circles represents Region IV and the filled circles show the potential in Region V. All potentials are calculated at a fixed monomer density. In (b) the changes in the depth of the potential at contact is depicted as the monomer concentration is varied. Once again the symbols correspond to the phases in (a).

semi-flexible polymer solutions with two point contacts dominating, (region VI) and flexible polymers in the fluctuating regime, (region IV) show similar behavior. On closer examination, however we see that the range of the interaction in semi-flexible polymer solutions is larger than that in a flexible polymer solution of equal concentration. The strength of the depletion interaction is also larger when compared with a solution in Region IV. The interaction energy for the same polymer concentration is much larger in solutions that lie in Region V, where triple contacts dominate. However the range of the interaction is reduced as seen from Fig. 3.10. Thus we see that depletion can be driven effectively by polymers that are stiff as well as solutions which have two point contacts and three point contacts dominating polymer-polymer interactions. On the other hand if attractive interactions are to be reduced then it is better to use a flexible polymer in which fluctuations are important.

3.8 Polydispersity Model

So far all discussions on polymer depletion have included an effective polymer size that can be characterized by either the radius of gyration or a correlation length. This implies that the molecular weight of polymer can be defined by a single number. In reality polymers, especially synthetic polymers, have an inherent molecular weight distribution that is determined by the manufacturing process. For example polystyrene is usually produced by anionic polymerization [1] which results in a Pois-

son distribution of molecular weights. Other common processes involve free radical polymerizations [15, 64] that result in a Gaussian molecular weight distribution.

Another source of polymer polydispersity might arise due to an asymmetric distribution of links. The traditional polymer model uses a random walk model to describe the distribution of links. This assumes a spherical distribution characterized by the radius of gyration. However, it has been suggested that random walks are anisotropic and might be better represented by an effective ellipsoid than a sphere [65, 62]. This would lead to a change in the shape of the depletion potential. Anisotropic link distributions might also arise in semi-flexible polymers, where a large persistence length makes the polymer more rod-like. Alternatively, one might ask whether the depletion layer formed around the colloidal sphere fluctuates? For instance, the polymer can extend 'arms' into the region, which would reduce the depletion cavity and change the interaction potential. All these possibilities make it essential to understand the effect of polydispersity on the AO model. We present a simple numerical simulation to explore this problem.

We model a polymer by a random walk and use several iterations to produce different conformational distributions. We then use two different schemes to measure an effective size. The first is a measure of the mean square distribution or the radius of gyration. A typical distribution for 10,000 different random walks of 160 steps is shown in Fig. 3.11. As expected it is Gaussian and is centered around the mean

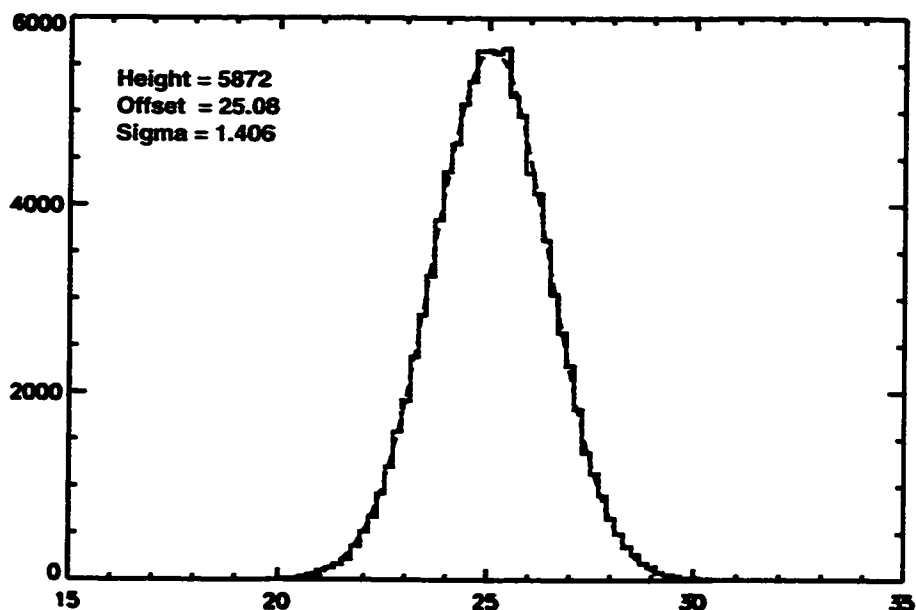


Figure 3.11: The probability distribution of the radius of gyration for a random walk consisting of 160 steps.

size. Alternatively we measure the maximum extent of the random walk, i.e. the effective size is calculated by monitoring the positions of the polymer links that are displaced the most. This allows us to create a distribution of sizes each of which is treated as sphere that contributes to the interaction potential. We refer to the second size measurement as a ‘caliper size’. The resulting distribution is shown in Fig. 3.12. We see that the distribution is asymmetric and is peaked at a slightly lower value than is seen for the radius of gyration. It also extends out much further as some configurations are much larger.

We use both these distributions to calculate a depletion potential. This is done by assuming that each effective size produces a depletion attraction and the resulting

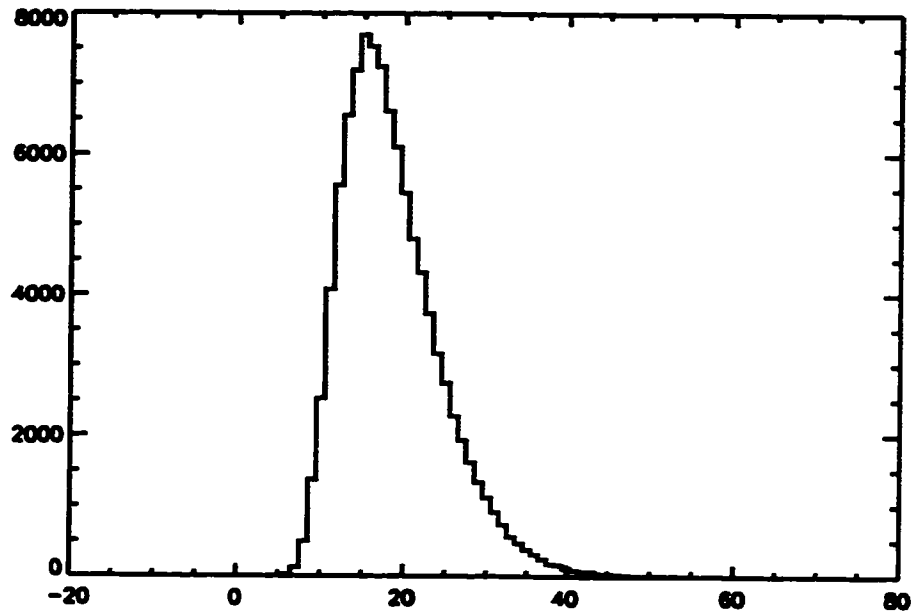


Figure 3.12: A probability distribution for the maximum extent of the polymer coil which is measured by using the ‘caliper’ technique described in the text.

interaction can be simply given as a weighted sum of all the contributions. The model assumes that linear superposition holds which is a valid assumption within the AO framework, since no second order effects are included.

The potentials calculated from the different size distributions are compared with the traditional AO potential in Fig. 3.13. We use the mean value of the Gaussian distribution shown in Fig. 3.11 as the radius of gyration of the model monodisperse polymer inducing a depletion interaction. The calculated AO model potential is shown as a solid line in Fig. 3.13. We see that the AO model accurately predicts the potential for polymers that exhibit a Gaussian distribution of sizes centered around the calculated radius of gyration. The asymmetric size distribution on the other

hand, produces a potential that is weaker but longer ranged. This can be seen more clearly in the magnified plot shown in Fig. 3.13(b). The increased interaction range results from contributions from configurations that are much larger than the radius of gyration. From Fig. 3.12 we see that there is a significant population of sizes that are larger than the radius of gyration. These larger coils also give rise to a weaker potential, since they reduce the colloid-polymer size ratio (see Fig. 3.13).

Our simple simulations reproduce the qualitative features of complex calculations carried out in the literature. Previous experimental reports [66, 67] on the effects of polydispersity on the depletion potential have indicated that polydispersity gives rise to instability in colloidal suspensions. Theoretical treatments of this issue have been limited. Walz [68] explores the effects of polydispersity via a general force-balance approach. His results at fixed volume fractions are similar to the results shown in Fig. 3.13, where polydispersity decreases the magnitude of the interaction and increases its range. Mao [69] explores the effects of polydispersity when higher order interaction effects are included in rod depletion. Second order effects usually predict a repulsive barrier in the depletion potential, however Mao predicts that polydispersity smoothens the depletion force and reduces the repulsive barrier. This is similar to the exponential tail that develops in the potential obtained in our simulations.

This simple calculation highlights that it is possible to extend the model to ternary systems and polydisperse macromolecular suspensions. The effects can be clearly seen

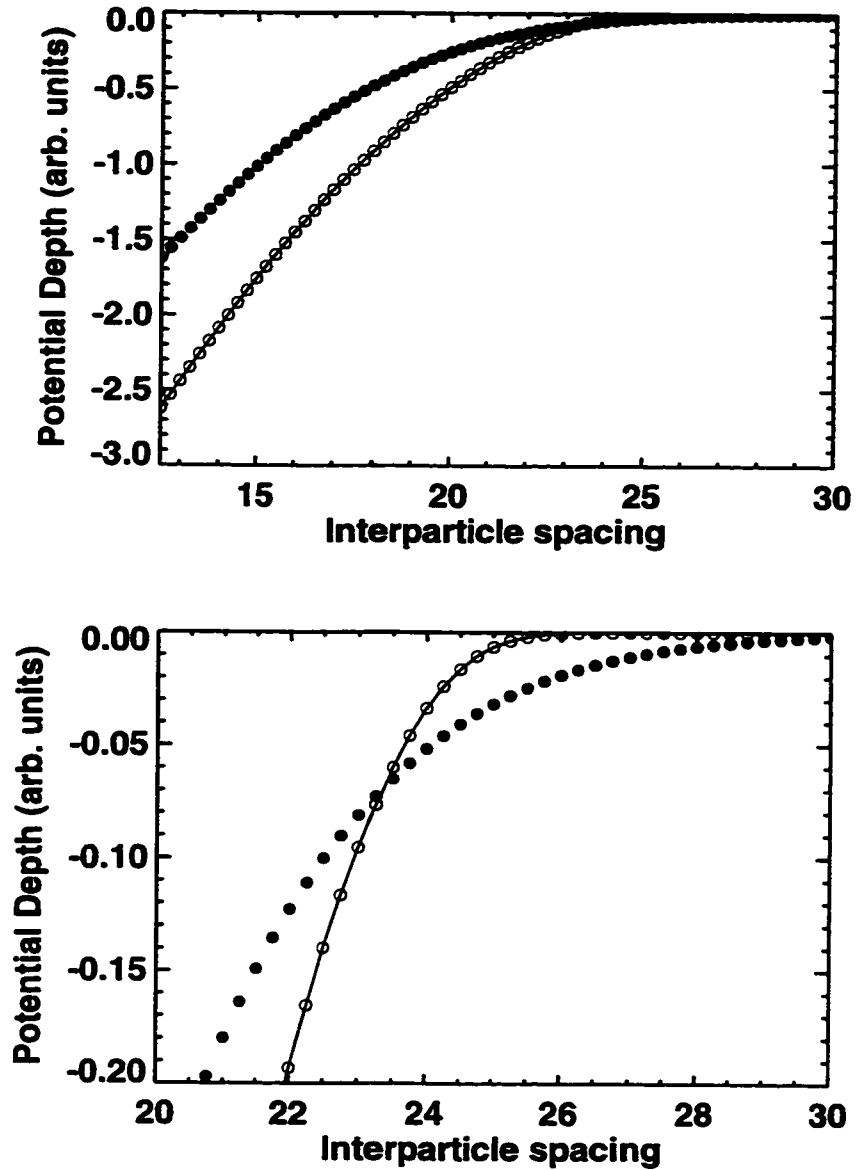


Figure 3.13: The potentials calculated by using the mean value of the Gaussian distribution (solid line), the Gaussian distribution shown in Fig. 3.11 (open circles) and the skewed 'caliper' distribution (solid circles). In (b) the crossover region is magnified.

in the calculated potentials. However if the polydispersity is very small, as was the case in the Gaussian distribution of the radii of gyration, then the effect is negligible.

3.9 Conclusions

In this chapter we have highlighted the effects that arise in colloid-polymer suspensions due to depletion interactions. We see that traditional hard sphere models can be mapped onto polymer depletion models to quantitatively predict the interactions. We will use these results to model our depletion measurements with polymeric DNA and colloidal silica in the subsequent chapters to confirm both the qualitative as well as the quantitative nature of some of these theories.

Chapter 4

Experimental Techniques

The ability to quantitatively track the motion of sub-micron probe particles is critical to this work. To do this, we need not only a microscope with high resolution imaging capabilities, but also the ability to record high quality video images for analysis. In this chapter we describe the tools that were used to obtain and process the images analyzed in this thesis. The procedures used for sample preparation are also described.

4.1 The Microscope

Most of our measurements were carried out on an inverted optical microscope, the Zeiss Axiovert 135. This is convenient for samples that sediment since they can be viewed while the slide is mounted face down. For particles heavier than water the density distribution of particles found near the cover glass is given by the Boltzmann expression [70], $P(z) \sim (1/L)e^{-(z-a)/L}$, where z is the distance from the cover glass, a is the particle radius and L is the characteristic Boltzmann length scale. This length scale represents the average height traversed by the particle due to thermal

fluctuations and is given by $L \sim k_B T / \Delta m g$ where k_B is the Boltzmann constant, T is the temperature of the system, g is the acceleration due to gravity and Δm is the mass mismatch between the particle and the displaced fluid mass. For a $1\mu\text{m}$ silica particle at room temperature this distance is on the order of $1\mu\text{m}$. The concentration of spheres near the coverslip can be conveniently imaged without passing through too much sample fluid. This is especially important for optical tweezing as a short working distance (1-10 μm) is crucial for stable particle trapping. The instability arises from the introduction of spherical aberrations in the light beam. Since the microscope objective is designed to focus a light beam in glass, the index mismatch between glass and water leads to a cylindrical focal region whose thickness increases with increased distance from the glass-water interface. As the spread of the beam into the cylindrical region increases, the stability with which particles can be trapped is reduced.

It is usually possible to obtain visually acceptable images by simple adjustment of the sample-objective working distance. However it is necessary to adjust other optical elements in the microscope when higher quality images are desired. I will discuss some of the basics of microscopy and the details involved in optimizing the parameters relevant to the present experiment. A more detailed description on the inner workings of the microscope can be found in Ref.[71].

Our microscope set-up is displayed in Fig. 4.1. As is true with most microscopes

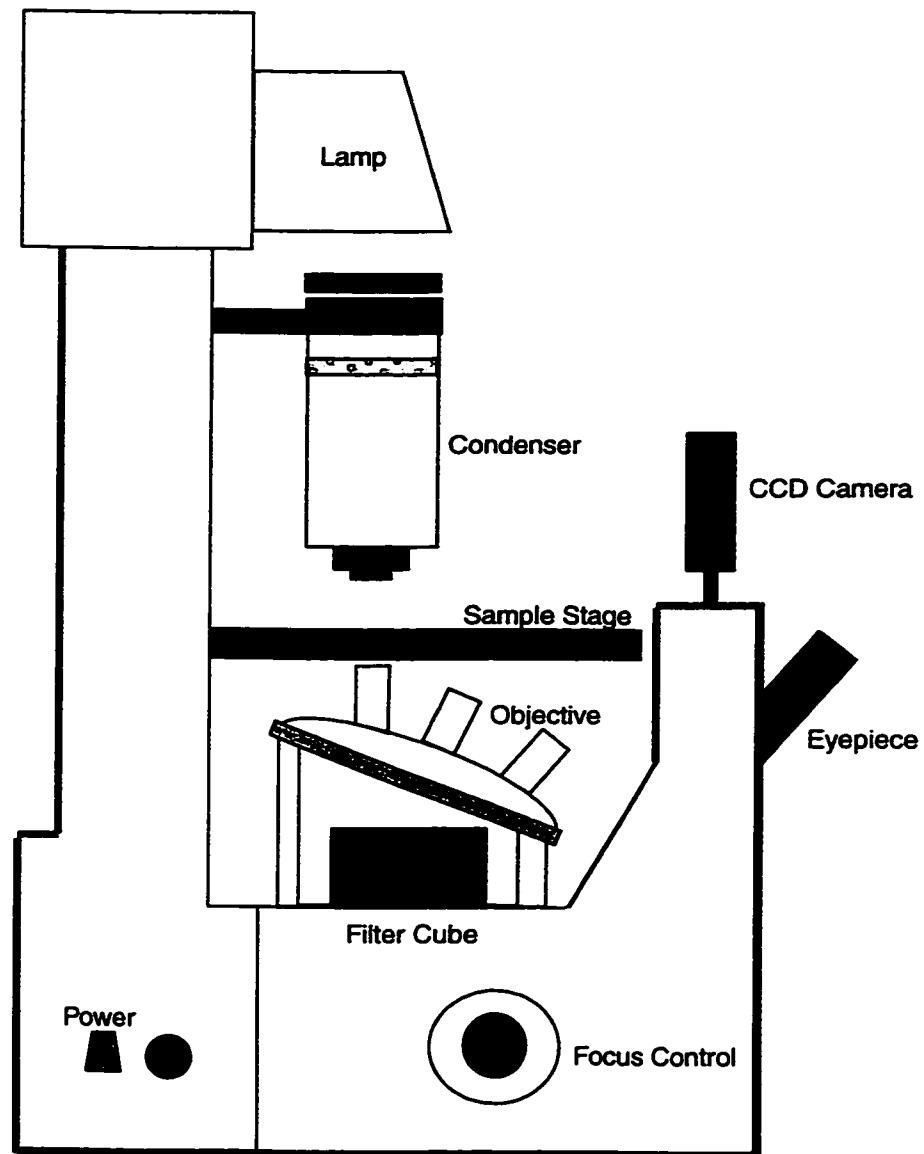


Figure 4.1: The Zeiss Axiovert 135, inverted microscope that was used for most of the experiments.

the optical path can be divided into two sets of conjugate planes - aperture planes (shown in Fig. 4.2(a)) and field planes (shown in Fig. 4.2(b)). These planes are reciprocal to each other, i.e. spherical wavefronts in the field planes are plane waves in the aperture plane and vice versa. For optimum resolution the optical elements in the microscope need to be adjusted so that these planes are reciprocally related. This is called 'Kohler Illumination'.

The halogen lamp light source (50W HBO, Osram) is positioned at the focus of a parabolic mirror for optimal light collection. A collector lens (L_c) focuses the light onto the condenser diaphragm (I_c) which is located at the focus of the next set of lenses, called the condenser lens (L_{cond}). Thus light coming to a focus at the condenser iris emerges from the condenser lens as a parallel beam. The beam passes through the specimen and is collected by the objective lens (L_o). The focal point of the objective, also known as the back aperture (B_a), is then conjugate to the condenser diaphragm. The image at the back aperture is real but inverted. Another set of lenses called the ocular lens relays this image to the eye-point. Thus the three planes at which the beam comes to a focus - the condenser diaphragm, the back aperture and the eye-point, form a set of conjugate planes, usually referred to as the aperture planes. These planes define different points along the optical path where an image of the light source can be obtained.

Similarly the reciprocal set of planes, called the field planes define different points

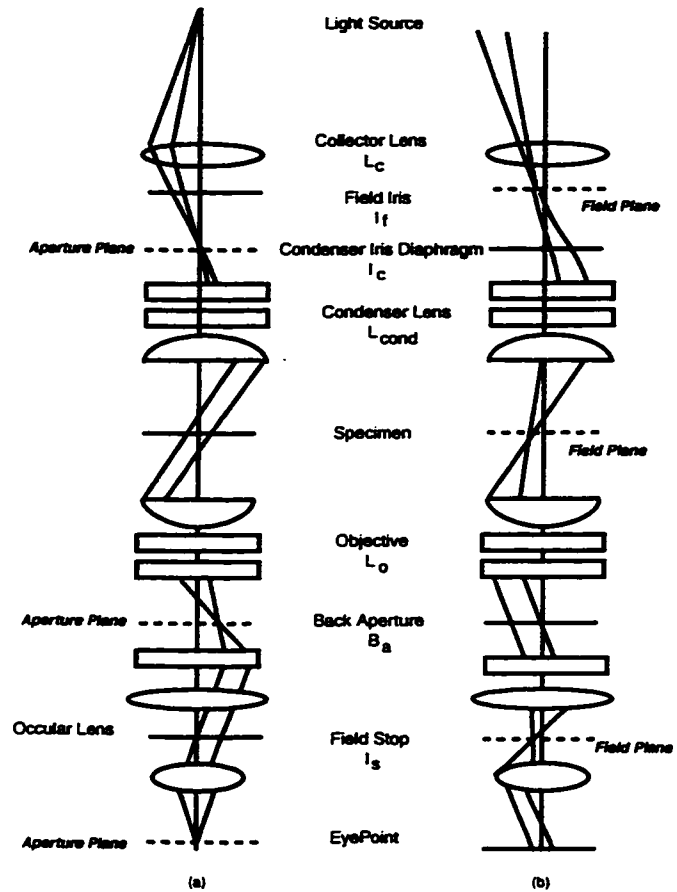


Figure 4.2: The light path through a typical microscope. In (a) we see the aperture planes and (b) shows the corresponding field planes. Each point along the path where the light comes to a focus, in (a) has a corresponding point in (b) where the light rays are parallel.

in the microscope where an image of the specimen can be found. The plane in which the sample is located is relayed through the microscope. This is shown in Fig. 4.2(b). Images of the specimen plane are found at the field diaphragm (I_f) and the field stop (I_s). Alternatively these planes also represent points at which one can find an image of the field diaphragm.

Most modern microscopes house the lens assemblies in an enclosed mount so adjustment of the collector lens relative the condenser lens is not usually needed. However the distance between the condenser lens and the specimen plane and the distance between the objective and the specimen plane is adjustable to accommodate for variations in sample thicknesses and sample holders. This makes it necessary to adjust the optics to optimize distances on either side of the specimen plane. In the first step, the objective is moved so that the focus lies in the specimen plane. This defines the working distance. To optimize the distance between the condenser lens and the specimen plane, the condenser diaphragm and the field iris is set to a minimum aperture. The height of the condenser is then adjusted so that the image of the field diaphragm comes into focus. The positioning screws are then used to center the field diaphragm. This constitutes Kohler illumination.

The next step in obtaining good quality images involves adjusting the illumination to gain the highest possible resolution while maintaining a high degree of contrast. In the x-y plane of a focused image each point is diffraction limited and is given by an

Airy disk. The resolving power is then given by the Rayleigh criterion which yields a minimum distance, r , to resolve an image to be

$$r = 1.22\lambda_0/2NA_{obj}. \quad (4.1)$$

Here λ_0 is the wavelength of the light in air, and NA_{obj} is the numerical aperture of the objective. For the 100X oil-immersion lens that was used in our experiments this number is roughly 200nm. The above condition assumes that either the specimen is self-luminous or the condenser NA is equal to the NA of the objective. When this is not the case, the resolution is determined by the sum of the condenser and the objective NA's which usually lowers the resolution, i.e. $r = 1.22\lambda_0/(NA_{obj} + NA_{cond})$.

The numerical aperture of the objective is determined by the size of the opening of the condenser iris. This controls the cone angle of light illumination and is given by

$$R = f \frac{n \sin \theta}{2} = f NA_{condenser} \quad (4.2)$$

where R is the radius of the opening, f is the focal length of the lens, n is the refractive index of the medium between the condenser and the image plane and θ is the cone angle. Increasing the opening size results in a higher NA, however it also reduces image contrast. Multiply scattered light arising from the optical components leads to this decrease in contrast. The opening size is selected according to the application to optimize these two competing effects. For our experiments this iris size was set to the mid-point of the available range, giving us a NA of roughly 1.2.

Multiply scattered light, or 'flare' as it is called, can also be reduced by the field iris. In our case the field iris aperture was opened until it was just visible at the edge of the field of view. Since the field of view for the eyepiece is slightly larger than the one for the CCD camera, the iris does not show up on the video image.

We use a Plan NeoFluar 100X oil-immersion lens (NA=1.3) as our objective. Typically oil immersion lenses allow for higher NA's and are more tolerant of spherical aberrations. In addition we also increase magnification by inserting another lens that lies between the objective and the ocular lens called the optivar or tube lens. This is set to give a multiplicative factor of 1.6 which yields a final magnification of 160. All the images are recorded are under bright field illumination. Once the sample is mounted on the stage and the microscope is brought into 'Kohler illumination', the objective is moved up to focus into the sample. It is often difficult to determine when the focus lies within the sample in a dilute aqueous solution so the edges of the cell are used to estimate the 'z' position.

Optimization of the microscopic parameters is essential for obtaining good quality images. Since we wish to extract quantitative information from our video images, all of the above parameters must be optimized so that the resulting images are high contrast, uniformly illuminated, and diffraction limited.

4.2 Optical Tweezers

The ability to manipulate microscopic objects with radiation pressure was first demonstrated by Ashkin [72, 73] in the late 70's. Since then many different versions of the optical trap and improvements have been demonstrated, most of which have been designed to operate on commercial microscopes [74, 75, 76, 77, 78]. The primary reason for this is that high NA microscope objectives are ideal for providing the strong intensity gradients needed for optical trapping. In addition, using a microscope allows the particles to be visualized while they are being manipulated. We use an optical tweezer to trap colloidal particles which are in turn used as probes to measure the properties of surrounding complex fluids. We then scan our trap at a fixed frequency to confine particles along a line. In this section we discuss some of the details of forming and scanning traps.

There are several detailed reviews to be found on optical tweezers [79, 80]. I will briefly outline the physics behind the tweezer and then discuss the relevant details for our particular trap.

Optical trapping is achieved by radiation pressure. When a beam of light is incident on an object it exerts two kinds of optical forces on the object. A scattering force, which pushes the particle in the direction of propagation of the light beam, and a gradient force which pushes the trapped object in the direction of the light intensity gradient. Therefore to trap a particle in the focus of a light beam, it is

necessary for the trapping force to exceed the scattering force which would tend to push the particle downstream. It is thus necessary to generate light beams with a large intensity gradient. Once the particle is successfully trapped it can be held in position and manipulated by moving the light beam. When the particle experiences slight displacements from the focus of the light beam, it experiences a restoring force which pushes the particle back to the focus (see Fig. 4.3). Thus it is possible to move the trapped object within the sample by slowly moving the laser focus around.

Theoretical descriptions of the trapping force are usually given in two regimes. When the particle size, a , is much smaller than the wavelength of light, λ , i.e. $a \leq 50nm$ for visible light, the Rayleigh scattering approximation holds. In this case the particle can be approximated as a point-like dielectric sphere and the total force exerted by the light field is given by [73]

$$\begin{aligned} \mathbf{F}_{\text{tot}} &= \mathbf{F}_{\text{scatt}} + \mathbf{F}_{\text{grad}} \\ &= \frac{\mathbf{E}^2}{c} \frac{128\pi^5 a^6}{3\lambda^4} \left(\frac{m^2 - 1}{m^2 + 2}\right)^2 n_0 - \frac{n_0^3 a^3}{2} \left(\frac{m^2 - 1}{m^2 + 2}\right) (\nabla \mathbf{E})^2 \end{aligned} \quad (4.3)$$

In the above equation, n_0 represents the background index of refraction and m represents the ratio of the index of refraction of the particle to that of the background medium. To achieve stable trapping the ratio of the scattering forces to the gradient force has to exceed unity. For a Gaussian beam incident on a particle of size a , this

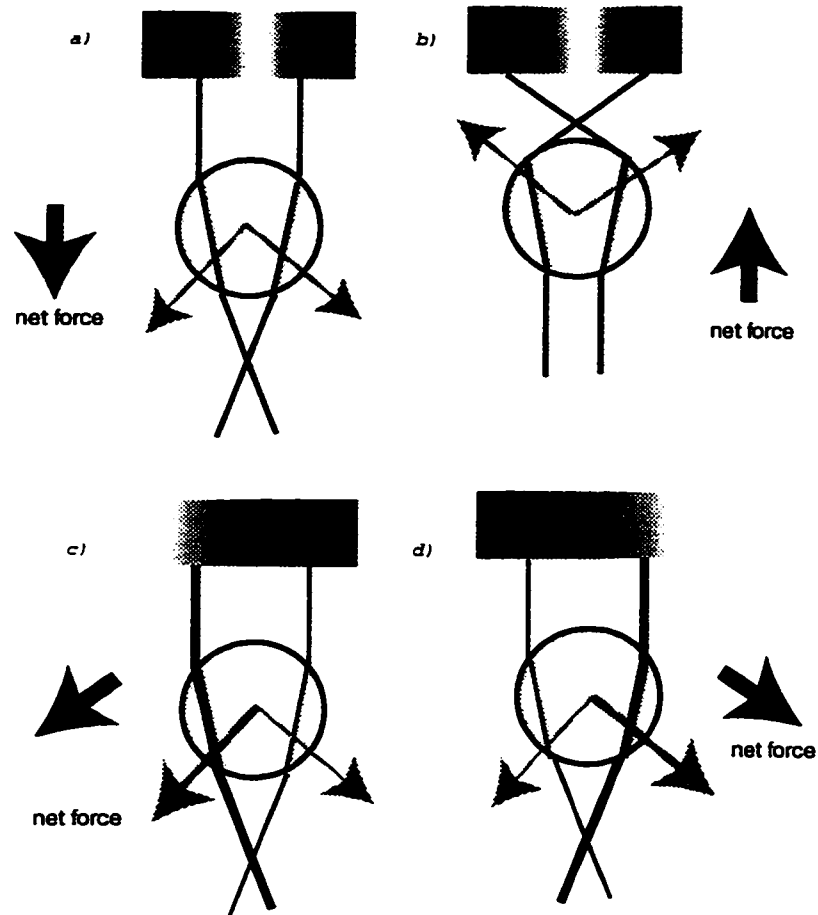


Figure 4.3: The forces exerted on a dielectric sphere in the ray-optic approximation are shown in the above cartoons. The boxes above each cartoon represent the light gradient where white is high intensity and black is low intensity. In (a) we see that the particle sits behind the laser focus. The difference between the incident ray and the refracted ray provides a momentum pulse that produces an equal but opposite reaction. This is shown by the grey arrows. The sum of the forces produces a net force towards the focus (shown by the solid black arrow). In (b) The particle lies in front of the focus. Once again conservation of momentum requires the particle to move towards the focus. In figure (c) and (d) the particle is moved off axis. The resulting forces shown by grey arrows indicate that the particle is pulled back into the beam towards the focus.

leads to the condition

$$\frac{3\sqrt{3}}{64\pi^5} \frac{\lambda^5}{a^3 w_0^2} n_0^2 / \left(\frac{m^2 - 1}{m^2 + 2} \right) \gg 1 \quad (4.4)$$

where w_0 is the laser beam waist. We see from the above stability condition that several factors control the trapping characteristics, - numerical aperture which determines $(\nabla E)^2$, the wavelength of light, the index mismatch, etc.

The above scenario is limited to the regime in which particles are much smaller than the wavelength of light. The opposite case, ($a \gg \lambda$), can be treated in a ray optic picture in which the particle essentially acts as a lens. The resulting force on the particle can be calculated by computing the momentum change experienced by each ray and then summing the contributions from all the rays - reflected and refracted. The stability conditions found in the ray-optics regime suggest that maximizing the cone angle of the incident light leads to a stable trap. In addition the dependence of the stability condition on the index mismatch has a maximum around $n=1.69$. A complete mathematical description of the resulting force can be found in Ref.[79].

The particles used in our experiments however, have diameters that lie between these two regimes. This presents a complicated scattering picture, and theoretical arguments do not as yet seem to coincide quantitatively with experimental observations [79]. Theoretical refinements based on electromagnetic theory [81, 82] have been proposed and experimental techniques are being developed to reliably calibrate the optical force [79, 83].

Even though there is a lack of agreement between theory and experiment, it is still possible to determine the key factors that control the characteristics of an optical trap. As already mentioned the numerical aperture plays an important role and beyond doubt the higher the numerical aperture the stronger is the trapping. Increasing laser power also helps make a stiffer trap, as does increasing the difference between the index of refraction of the trapped particle and the background suspension. Spherical aberration effects are also important. Trapping characteristics are greatly diminished if there is significant spherical aberration in the laser wavefront. There are many ways that this can be introduced. Most commonly, non-uniformity of the coverslip glass and large working depths in the sample volume introduce aberrations that make trapping difficult. In addition microscope objectives introduce spherical aberration into the infra-red light beams that are commonly used to form traps, since they are designed to work primarily in the visible region. Moreover the particle itself can distort the beam profile causing instabilities in trapping.

From Fig. 4.3 we see that if the particle moves out of the beam the forces acting on the sphere pull it back to the focus. If the optical trap is moved back and forth slowly within the sample, then the particle follows its focus. However if the trap is moved sufficiently fast, i.e. the viscous drag on the particle exceeds the trapping force, the particle can escape from the trap. For example, the Stokes drag on a sphere of size a moving at velocity V is given by $F_{\text{Stokes}} = 6\pi\eta aV$, where η is the viscosity of the

background fluid. For a $1\mu\text{m}$ silica sphere in water at room temperature, a velocity of $1\mu\text{m/s}$ gives a force of $\approx 1\text{pN}$, which is a typical trapping force for a 100mW incident beam. If the scan rate is further increased, the trap returns to the spot before the particle has had a chance to diffuse away, and the particle is once again momentarily trapped. By scanning the light back and forth very rapidly it is possible to achieve a one dimensional potential that confines the particle in two directions but allows it to freely diffuse in the third, i. e. along the scanning direction.

The physics behind the scanning trap can be understood by examining the forces on the dielectric particle. In a point trap the energy density stored in the light field is minimized by placing a dielectric particle at the focus of the light beam. This gives rise to the gradient force which attracts particles to the region of highest light intensity. If the region of high light intensity is changed from a point to a line the particle will once again be attracted to this region. The sphere will be confined in two dimensions but since there are no intensity gradients along the line it will be free to diffuse in that dimension. This is the scenario created by scanning a point trap back and forth rapidly. The particle feels the time average of the electric field and is trapped on a line along the direction of the scan. The details of trap induced forces on the particle will be discussed in detail in the next chapter.

To construct a line tweezer there are several practical considerations that should be taken into account. To get the maximum trapping power we need to focus the

laser to a tight spot in the specimen plane. In order to achieve this the laser beam should fill, if not overfill the back aperture. Additionally it is necessary to maintain the stability of the trap while it is scanned. This requires that as the laser beam is scanned, it should pivot around the back aperture, so as to maintain overfilling. At the same time it is increasingly important to minimize spherical aberrations since the quality of trapping in a scanning trap is highly sensitive to this parameter.

For our line trap we found that we could successfully trap micron sized silica and PMMA spheres in water but polystyrene spheres were unstable. This is contrary to the idea that higher index mismatch leads to stronger trapping, since silica and PMMA have indices of refraction of 1.45 and 1.49 respectively while polystyrene has an index of refraction of 1.58. We speculate that our system has a large amount of spherical aberration which in turn has a greater destabilizing effect on particles with a higher index mismatch. By changing the geometry or objectives it might be possible to line trap polystyrene successfully (N.B.: this has been previously reported in Ref.[74] for a ring tweezer arrangement).

To create an optical trap, we used the cw output of a Nd:YLF laser, at its fundamental frequency, 1054 nm. We also use a HeNe laser that is collinear with IR beam to aid in the visualization of the beam path. The cw IR light (and the HeNe beam) passes through a polarizer-quarter wave plate combination which serves as a power regulator (see schematic in Fig. 4.4). The light is then coupled into a single mode

fiber which emerges near the microscope table. Not only does the fiber serve as a light conduit but it also helps spatially filter the beam. We once again use a polarizer and quarter wave plate combination, to select a definite beam polarization. This is important since the shape of the effective optical trap is polarization dependent. The laser beam induces a dipole moment in the particles. A beam of light that is polarized perpendicular to the plane of incidence, i.e. s-polarized, induces dipoles in the spheres that are normal to the scan direction. This results in a repulsive interaction between the spheres that could potentially be useful in separating particles that would otherwise be aggregated. On the other hand for light polarized in the plane of incidence (p-polarized), the dipoles induced in the sphere lead to a net attraction depending on the separation. We use p-polarized light for our experiments.

After polarization selection the laser beam is reflected off a mirror that can be scanned by a galvanometer. The entire assembly is mounted on a Gimbel mount, which is positioned so that the back aperture of the microscope can be imaged onto the center of the mirror. This ensures that small motions of the mirror do not change the position of the beam on the back aperture thus making it a pivot point. However the motion results in displacements in the specimen plane. This is shown schematically in Fig. 4.5. The back aperture is imaged on the mirror through a telescopic arrangement of two lenses. We mount one lens (L1) outside the microscope assembly and the second lens (L2) is conveniently mounted in the filter cube of the Zeiss Axiovert 135. We use

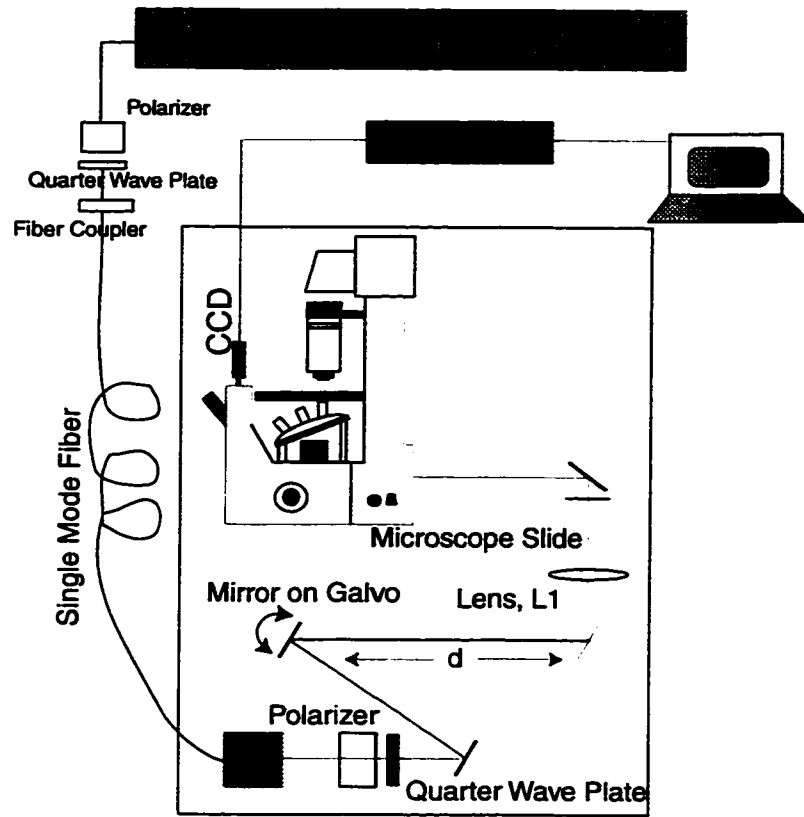


Figure 4.4: The details of the experimental set-up.

a steering mirror to direct the beam through the fluorescence port of the microscope. We also insert a microscope slide in the beam path between the two lenses to serve as a pick-off mirror which directs a portion of the beam into a power meter. This allows us to monitor the beam intensity throughout the experiment.

The telescope achieves two purposes: it forms a collimated beam whose magnification can be adjusted by appropriate choice of focal lengths and it allows the back aperture to be imaged onto the scanning mirror. In our system the position of the lens mounted on the filter cube is fixed. This fixes the distance from the lens to the back aperture, $d_{BA} = 15cm$. The position of the second lens outside the microscope is set to the sum of the focal lengths of the two lenses so that the combination of L1 and L2 forms a telescope. The distance to the steering mirror d , is then calculated to be

$$d = \frac{f_1}{f_2}(f_1 + f_2 - \frac{f_1}{f_2}d_{BA}) \quad (4.5)$$

where f_1 is the focal length of the first lens (L1 in Fig. 4.5) and f_2 (L2) is the focal length of the second lens. In our system, $f_1 = 40cm$ and $f_2 = 12.5cm$ and the distance $d = 20cm$. The beam size at the back aperture w_{BA} is given by $\sim (f_1/f_2) \times w_m$, where w_m is the beam size at the steering mirror. This is calculated to be $w_{BA} \approx 3mm$.

With our present set-up we use 50mW of infrared light to form a line trap which is scanned back and forth at 180Hz. The galvanometer is driven by a triangle wave output of a frequency generator with an amplitude of 0.25V. Theoretically this wave-

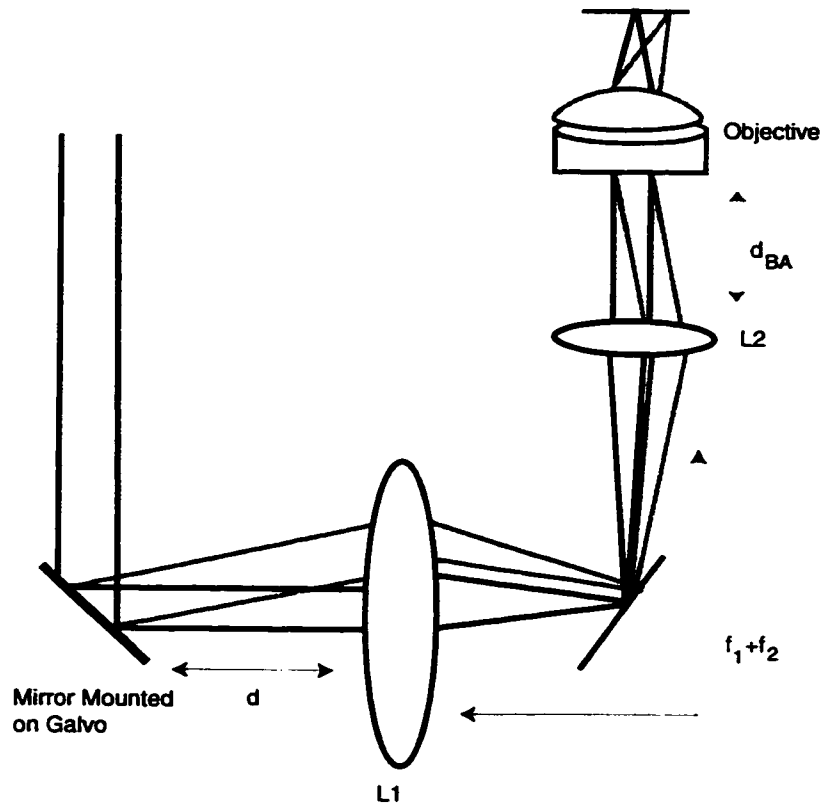


Figure 4.5: A telescope formed by lens L1 and L2 images the back aperture plane onto a point. A mirror mounted on a galvo is placed at this point. Thus small rotations result in lateral translations of the focus on the image plane. The grey lines indicate the beam path when the mirror is rotated slightly.

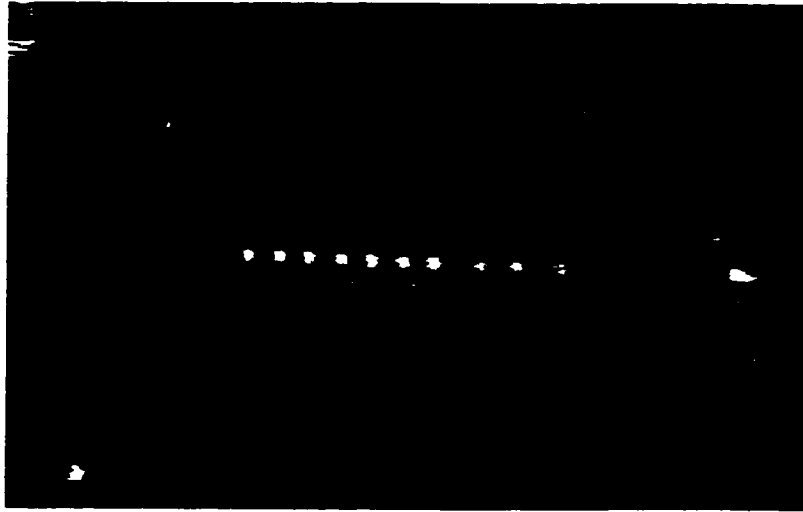


Figure 4.6: The optical line tweezer with several particles trapped on the line tweezer. form should produce a square well optical potential, however non-linearities in the function generator yield a highly complicated potential. For example the center of the scan region presents a parabolic potential with a width of $2.5\mu\text{m}$, which probably results from non-linearities that arise at the crossover point in the center of the scan range. At the turn around points the time averaged potential is much deeper leading to 'sticky ends'. A video image of the line trap is shown in Fig. 4.6. The image includes particles stuck at the turn around points, which indicates the length scanned. This 'sticking' probably results from the non-linearities in the motion of the scanning mirror and spherical aberrations in the beam. It is possible to change the scanning length by adjusting the amplitude and frequency of the driving signal (a word of caution, this can result in degradation of the shape of the optical trap at certain frequencies).

How does the scan rate affect the optical potential? An extensive survey of the effects of scanning traps can be found in Ref.[70]. Faucheux *et al.* observe three different regimes in their ring tweezer; a slow scan frequency regime in which the particle follows the trap, an intermediate regime where the particle remains trapped on the circle but feels a kick each time the optical trap traverses it and a third regime in which the particle is free to diffuse along the circle. In our experiments the scan rate exceeds the speed at which the particle would follow the trap. However we cannot distinguish between the latter two regimes. Video images seem to indicate that the particles experience a 'kick' as the laser scans over them but we see no effect of this on our measured potentials. This might be due to the bi-directional scanning employed in the line tweezer set-up. In this scheme the particle gets kicked twice, but in opposite directions, which possibly leads to a cancellation of the effect. In addition we measure relative distances between the particles which is likely to be less sensitive to the impulse imparted, since both particles are affected similarly.

4.3 The Detection System

In order to quantify the observed particle motion, we use fairly standard methods of video microscopy, (implemented by John Crocker). The analysis scheme has two parts. The first step involves recording of analog video images, using a CCD camera and a high end Sanyo VCR (Model GVR S950). The second step involves digitizing

these images and processing them to obtain particle coordinates.

Video images use up large amounts of disk storage space; a two hour data set needs approximately 800 Gigabytes of disk space! This hurdle is bypassed by using an analog recorder - a VCR, and digitizing only small regions of interest, within each image. Our images are recorded by a Hitachi Denshi CCD camera (Model KPM1U), which is fitted onto the optical microscope. A mirror deflects the light from the eyepiece onto the camera port. Our particular camera has an active area which is 768 x 493 pixels. It also has an electronically controlled variable shutter which was generally set at 1/10000 of a second. The detected image is converted into a video signal which is recorded on a S-VHS tape by a video deck.

It is necessary to stress that high quality images are needed for accurate measurements. In order to obtain high resolution images we need to optimize the optical alignment and the electronics used to detect the image. Image contrast was optimized by adjusting the illuminating light intensity and the gain and offset voltage on the CCD chip which was controlled by a Hamamatsu Power Supply (Model C2400). Prior to recording we also make sure that no pixels are saturated and we have the largest possible working dynamic range.

The video signal recorded has two important aspects that we utilize in our data analysis scheme. Since each point in the video image is defined not only by a voltage but also time delay the chronology of frames recorded can be stamped by the VCR

on the audio channel of the video tape. This proves to be an essential feature for us as it allows us to return to sections of the tape on a frame by frame basis. We can access each frame individually through our VCR which in turn is computer controlled through the RS232 port of a Macintosh 7300 computer using a NIH Image software package. Another feature that is usually present in video signals is interlacing. Every frame is dissected into an odd and even field. Each field is constructed by scanning every other line, 60 times a second. The scanning spot records the even lines on the screen until it reaches the bottom after which it returns to the top and starts scanning the second (odd) field. The two fields are then interlaced to provide a composite image. We exploit this feature to double our time resolution by analyzing each field independently. The increased time resolution more than adequately compensates for the degradation of image quality. Moreover, particles that are in motion yield jagged images which complicate image analysis. Such issues are avoided by analyzing each field separately.

The second step in video microscopy involves converting the analog images to digital ones which can then be used for quantitative analysis. This is done through a dedicated frame grabber card (LG-3, Scion Image) which is installed in the computer. The frame grabber card receives the signal from the VCR and stores it on the computer. It is also controlled by NIH Image, which allows the user to write Pascal-based macros [84] to control the functions of the frame grabber card. Our typical macro

allows us to grab small regions of interest at user defined start and stop times. This lets us automate digitization of an entire videotape, which is equivalent to 200,000 frames. For most of the interaction measurements a small spatial region of interest centered around the two spheres was chosen. The size of this area for $1.1\mu\text{m}$ spheres at 160X was usually chosen to be 40 X 112 pixels. Images were grabbed in 30 second blocks and could be directly stored on the server used for image processing.

4.4 Image Analysis

The digitized images were all analyzed on a UNIX platform using IDL (Interactive Data Language, Research Systems Inc.). The image analysis can be divided into several steps. The first step involves correcting for background effects such as intensity gradients and inhomogeneities, which will subsequently be referred to as 'flat-fielding'. The digitized images are then separated into even and odd fields and a centroid calculating algorithm is used to locate the centers of the particles in each field.

a) Flat-Fielding

Since the emphasis of video imaging lies on accurate location of particles it is essential to make sure that there are no systematic errors which lead to pixel biasing. In images that are recorded under bright field illumination, there are two sources of inhomogeneities that might arise. The light source may provide a non-uniform illumination of the specimen or the sensitivity of the CCD pixels may vary across

the chip. A combination of both these effects can lead to undesired features in the images. To prevent this, an image usually called the 'flat' is recorded at the end of each data set. Unless lighting conditions are changed between sets of acquired data, this need only be done once. The 'flat' image is an illuminated field of view that is devoid of any features. This is usually done by focusing up into the cover glass or finding a region in the sample that is featureless. At the same time a 'dark' frame is also recorded. This measures the thermal response of the CCD chip in the absence of a light source. The 'dark' frame was usually recorded by turning the halogen lamp on the microscope to the lowest setting.

The flat and the dark frames are used in a standard algorithm to calculate the background image which is then subtracted off the actual image. The background offset is calculated by

$$b = f - \left(\frac{f - d}{\bar{f} - \bar{d}} \right) \bar{f} \quad (4.6)$$

where f and d is the deviation of each pixel from the mean value of the flat and dark frames represented by \bar{f} and \bar{d} , respectively. The gain is given by $g = (f - d)/(\bar{f} - \bar{d})$. The value of each pixel in the dark and flat frames represent two points defining the gain and offset associated with each pixel. The above formula maps the gain and offset of each pixel onto the values calculated for the mean. The flat-fielded image is calculated by subtracting, $(g * \text{image} + b)$, from the original image.

b) Centroid Calculation

After the image has been flat-fielded the centroids of the spheres are calculated. This is done by locating the brightest pixel in a user defined region. It is further required that this pixel lie in the top 30th percentile of the bright pixels since the brightest pixels correspond to the particle centers. The pixel is located through a gray scale dilation scheme. In this scheme all pixels are set to the maximum value in a defined region. Then the pixel in the original image which corresponds to this value is chosen as a candidate. A circular mask is then placed at this location and a brightness weighted centroid is calculated. If the centroid value differs from the position of the brightest pixel by more than 0.5 pixels then the centroid is recalculated. A detailed description of this technique can be found in Ref.[85].

A second refinement is added to correct for biasing that may result due to brightness changes. Overlapping of features or changes in brightness due to reflections induced by one sphere on the other might lead to pixel biasing. This is especially significant when the spheres are close together. We correct for this effect by reflecting the centers of each of the spheres around the centroid of the other sphere, and selecting an area around this point. The inverse of this region, which is of the size of the spheres, is subtracted from the original image. This effectively removes the contributions from the tail of the brightness distribution of one sphere that underlies the intensity profile of the second sphere. The process is graphically illustrated for an

artificially generated image, in Fig. 4.7. The algorithm is iterated to get further refinements. The resulting positions are stored in a file along with the radius of gyration of intensity distributions, eccentricity, and a 'mass' distribution which corresponds to integrated brightness. The details of procedure routines and calling sequences are given in Appendix C.

4.5 Sample Preparation

When working with biological samples it is necessary to handle small sample volumes. Most of our experiments were carried out in small microchambers, whose cavity volumes could be easily controlled. The simple design is shown in Fig. 4.8. The coverslips and microscope slides used were bought from Fisher Scientific Inc. and were $18\text{mm} \times 18\text{mm}$ and 0.17mm thick (nos. 1.5). All coverslips and microscope slides were handled with powder-free nitrile gloves to prevent finger grease contamination. In addition they were cleaned by a methanol wipe to remove any particulates that might be present. We found that using these precautions lowered non-specific adhesion of the colloidal particles to the glass surface. The coverslips are attached to the microscope slide by Parafilm strips cut into a 'L' shape, and arranged so that they form a square with two channels left open for sample loading. The volume of the cavity is controlled by changing the width of the L's. A heating plate was used to melt the Parafilm sealing the coverslip to the microscope slide.

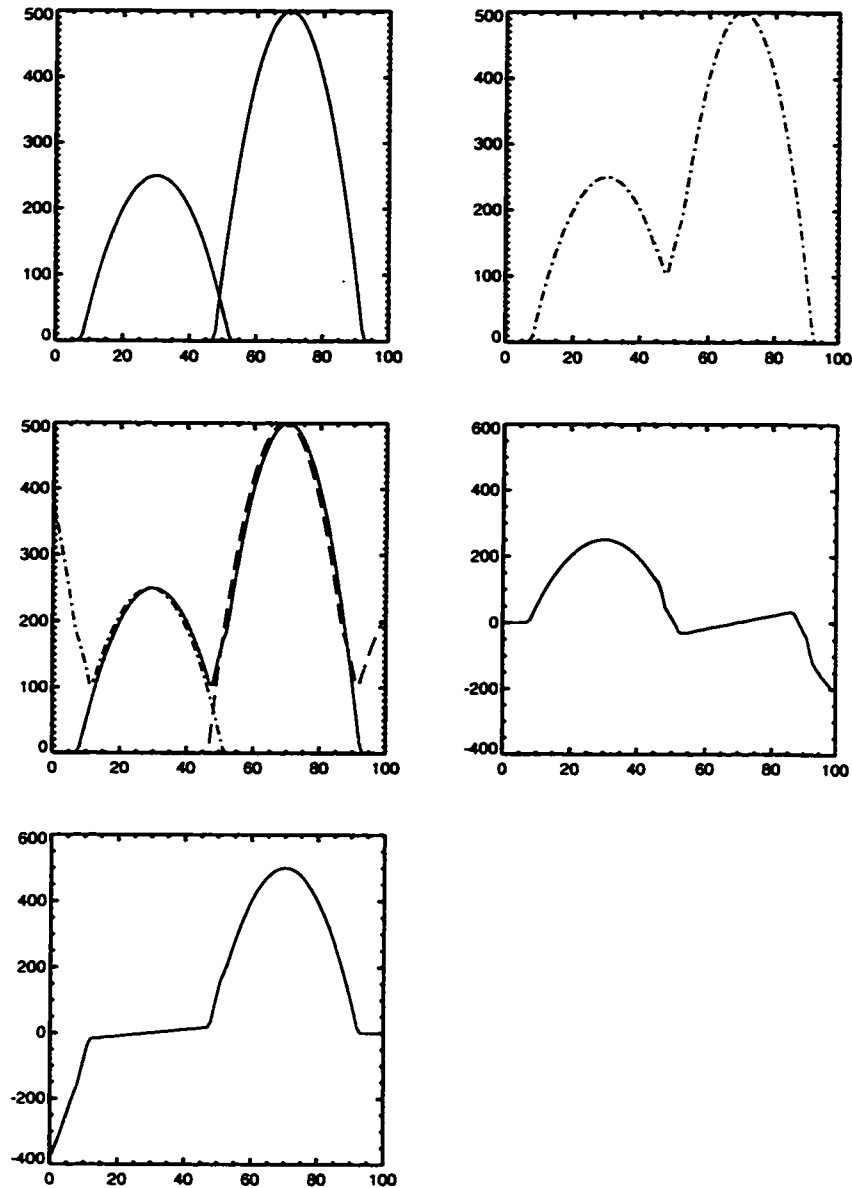


Figure 4.7: This figure shows a schematic of the centroid calculating algorithm used to correct for overlap. In (a) we show two spheres modeled as parabolic caps, with a small overlap region. The sum of the two parabolic functions is shown in (b) which is analogous to the image we measure. We then locate the two maxima and reflect the image around each of these points. This is shown in (c) as the dashed lines. The mirror image of (c) is subtracted from the original image (b) to obtain the location of the two particles shown in (d) and (e).

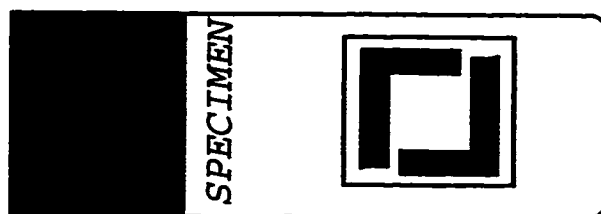


Figure 4.8: A typical sample cell. The grey region represents the Parafilm.

The channels are used to inject the sample into the chamber. A small drop placed near the opening is drawn in through capillary action. The mouths are then sealed with vacuum grease to prevent evaporation. This provides an adequate chamber to hold samples and if carefully prepared can be kept for days, without significant drying of the sample. There are of course obvious changes that can be made to accommodate other considerations. For instance one of the channels can be easily used to insert and hold a micro-pipette tip, thermocouple, capillary tube, etc.

The Colloids

The primary source of colloidal spheres used in these experiments was Bangs Laboratories Inc.. The spheres used were usually $1.1\mu\text{m}$ diameter anionic silica spheres. The surfaces of these spheres are terminated by a hydroxyl group, Si-OH which gives them their negative charge. Since our model polymer, DNA is also negatively charged the anionic sphere-polymer interaction is repulsive and can be controlled by changing the background ion concentration. Most of our experiments were carried out at low ionic concentration, $\sim 10\text{mM}$ where the electrostatic interactions are screened, making the particles and polymers effectively 'non-interacting' on larger length scales.

Silica particles were chosen for these experiments since we found that the more commonly used polystyrene spheres could not be effectively trapped in the line tweezer and PMMA spheres seemed to have occasional tethering problems probably due to the presence of a 'hairy' polymer layer on the surface. For the two sphere interaction measurements the colloidal samples were diluted to final volume fraction of 10^{-7} . We found that at these concentrations it was still relatively easy to find two particles, however the sparseness also prevented stray particles from drifting into the experimental region.

For the multi-particle tracking experiments described in Chapter 6, fluorescently labelled polystyrene spheres (Molecular Probes Inc.) were used. Since polystyrene has a density close to that of water, $1.05\text{g}/\text{cm}^3$, the density of the background solution could easily be adjusted to remove buoyancy forces. This was done by using a mixture of water and heavy water, $H_2O : D_2O = 1 : 1$. The exact volume fraction of colloidal spheres was not known for the multi-particle tracking experiments since the samples used were pre-filtered through $2\mu\text{m}$ filters to remove aggregates. The number is estimated to be around 10^{-4} . In both sets of experiments the colloidal particles were diluted in the buffer that was used for the DNA molecules. For particle tracking experiments aqueous buffers were replaced by the heavy water-water mixture.

4.6 DNA Preparation

For the purposes of this thesis we needed a model monodisperse polymer with a size range that was larger than a hundred nanometers but still within a couple of microns this would allow us to clearly resolve the measured length scales and at the same time not have it exceed the size of our optical trap. Most commonly available synthetic polymers have sizes that lie in the nanometer regime with a few that can be specially synthesized to yield larger lengths. In addition the polymerization processes used to synthesize these polymers produce a wide distribution of molecular weights, which would introduce significant polydispersity in our measurements. These limitations are easily overcome by biopolymers which provide a vast resource for experimental polymer physics. Additionally, studies on these polymers often reveal interesting structural and mechanical properties that help us better understand their biological functions [86, 12]. In this thesis we use DNA as a model polymer to study conformational properties of macromolecules in solution. They easily fulfill the requirements necessary - i.e. monodispersity and a large size-scale. Moreover, biochemical techniques allow structural and topological changes that can change interactions from the angstrom regime all the way up to the micron region, with a high degree of accuracy. This makes biopolymers particularly valuable for opening up areas of study that are difficult to access with synthetic polymers. In this section we discuss certain basic handling and biochemical protocols used for these molecules.

The DNA molecule is made up of sugars, phosphates and nitrogen bases that arrange themselves in the well known double helical structure (see Fig. 4.9). The sugars and the phosphates form a backbone on the outside and the nitrogen bases pair up to form a ladder structure in the interior region. The nucleotides (= sugar + phosphate + nitrogen bases) come in different varieties, however bonding only takes place between specific pairs. For example, Guanine (G) only bonds to Cytosine (C) and Adenine (A) only binds to Thymine (T). This allows the identification of a complementary strand given a single strand of a known sequence.

The double stranded DNA structure is formed by complementary nucleotides polymerizing to form the helical structure. The nucleotides bind together through phosphodiester bonds, i.e. the hydroxyl groups attached to the 3' carbon of the sugar, bonds to the phosphate of another nucleotide. The single strand has a chemical orientation; one end is labeled the 3' and the other is called the 5' end. The 3' end has the hydroxyl attached to the 3' carbon of the sugar and the 5' end has a phosphate group attached to the 5' carbon of the sugar. The double stranded DNA is formed by bonding between two anti-parallel single strands, i.e. one chain orientation runs from 3' to 5' while the other runs from 5' to 3'. These orientations become important when considering enzymatic activity.

The spacing between base pairs in the double stranded DNA is 3.4 Angstroms and 10 basepairs form a single twist resulting in a helical pitch of 3.4 nm. This helical

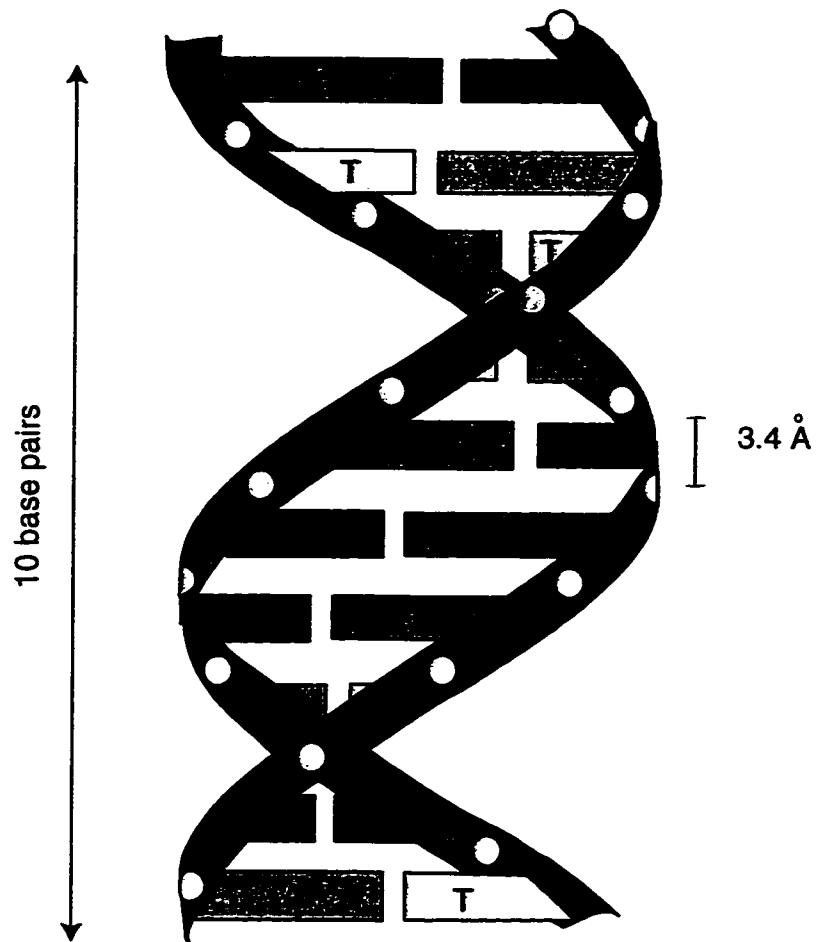


Figure 4.9: The helical structure of double stranded DNA. The outer backbone is formed by the sugars and the phosphate groups. The inside is primarily composed of nitrogen base pairs.

secondary structure gives rise to the long persistence length that is found in DNA molecules. In most common buffers the persistence length is measured to be 50 nm. In contrast single stranded DNA has a persistence length of only 2 nm. However, sufficiently long double stranded DNA still form random coils.

For our experiments we use a $16\mu\text{m}$ long DNA called lambda phage DNA. Lambdaphage is a virus with a very simple DNA structure. It invades E.coli bacteria and uses the native DNA to replicate. Enzyme digestion of infected E. Coli and subsequent purification produces abundant quantities of lambdaphage DNA. In the bacteria, λ -DNA exists as a plasmid (i.e. it is circular), but subsequent digestion produces linear lambda, which is exactly 48,502 base pairs long.

I. Fill-in, cutting and ligating

On each end of the linear DNA produced by digestion of plasmids, there is an overhang of single stranded DNA that is 12 base pairs long. These are often referred to as 'sticky ends'. This is a result of the digestion process in which the restriction enzyme cuts the plasmid λ -DNA (See Fig. 4.10) diagonally. As a result the sequences on the two ends, CAATTG, and GAATTC are complementary, and have a tendency to close on themselves or attach on to other lambda DNA in solution forming plasmids and multimers.

λ -DNA with cohesive ends can be commercially bought from numerous companies (New England Bio-Labs, Promega Inc., Gibco etc.). It is usually shipped in a buffer

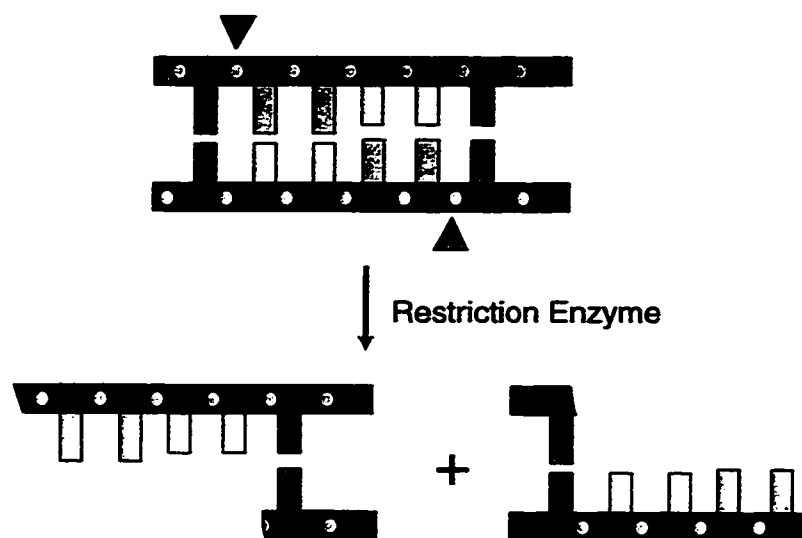


Figure 4.10: An example of a restriction enzyme that cuts double stranded DNA diagonally, leaving a single stranded overhang on the two different pieces.

which contains, 10mM Tris-HCl (tris[hydroxymethyl]aminomethane hydrochloride) and 0.1mM EDTA (ethylenediaminetetraacetic acid) and has pH=8.0. Tris-HCl serves as buffer for biological reactions whereas EDTA serves as a preservative that keeps bacteria from growing in the solution. It depletes the solution of divalent ions such as Ca^{++} which are essential for bacterial growth.

The affinity of the complementary ends is a problem for our measurements since we are interested in properties of linear polymers that are monodisperse. The formation of random plasmids, dimers and trimers are not acceptable. Fortunately, DNA biochemistry has developed many tools that prove to be invaluable for our purposes. (Most of the biochemistry used here was done at the DNA Sequencing Facility (contact: Liz Geiger, Richards Building, 573-7407), however, with the right equipment

and a little bit of experience it can be done in our laboratory as well. There is a whole family of enzymes that can manipulate and selectively alter DNA strands. The cohesive ends can be 'filled in' with one such enzyme called T4 DNA Polymerase. This enzyme, in the presence of a special buffer (T4 DNA Polymerase Buffer which contains 50 mM NaCl, 10mM Tris-HCl, 10mM MgCl₂, 1mM dithiothreitol (pH7.9, 25C)), BSA (Bovine Serum Albumin) and dNTP's (nucleotides), adds nucleotides to the 5' end that overhangs the 3' end and removes the 3' overhang to form a blunt end. Since λ -DNA has two overhanging 5' ends the addition of T4 DNA Polymerase to a solution containing λ -DNA, and nucleotides (in the presence of Mg²⁺) leads to a 'fill-in' reaction (for details see flow-chart in Fig. 4.11). This specific function of the enzyme is termed its ' 3' \rightarrow 5' exonuclease activity'.

It is important for our experiment that there are no remnant proteins or divalent ions left behind. The DNA is subsequently purified through a phenol-chloroform extraction. This resuspension procedure is also used for changing salt concentration of buffers. The addition of equal amounts of phenol and chloroform renders the solution a 'poor solvent' for the protein leading to the formation of an aqueous and an organic phase. The mixture is centrifuged and the aqueous solution is carefully removed with a pipettor. This step is repeated several times till there is no visible murky interface between the aqueous and organic phases. The last few extractions are done with chloroform only since it easily evaporates, which reduces the chances of

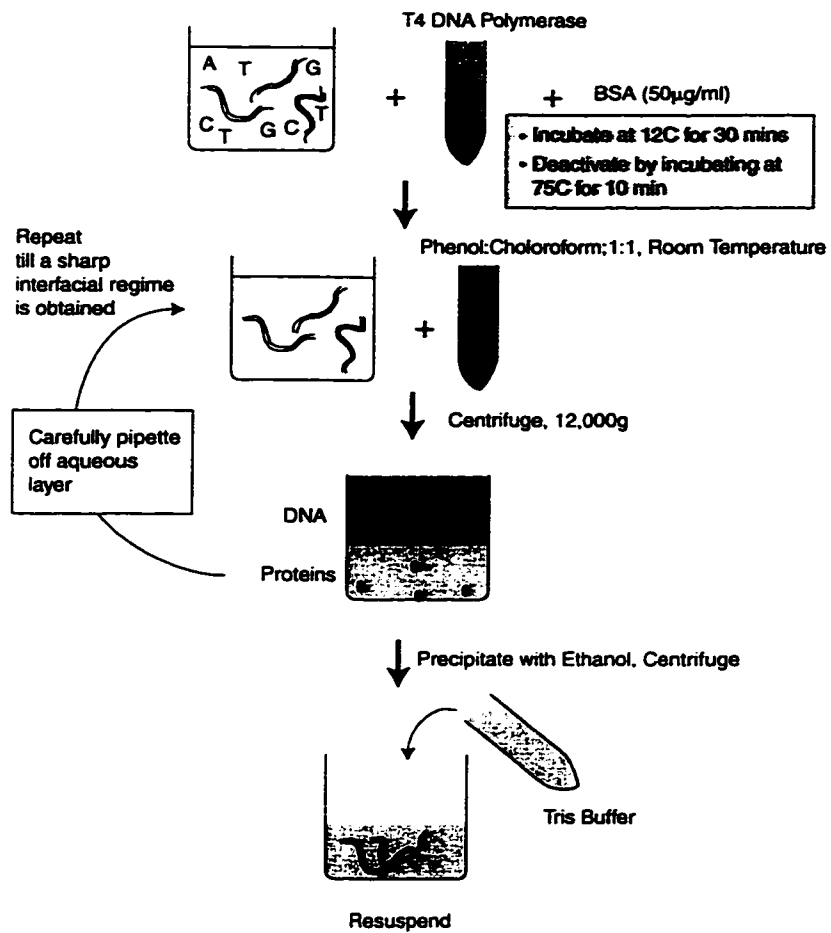


Figure 4.11: The different steps of the fill-in reaction. T4 DNA Polymerase adds nucleotides from solution to single stranded DNA.

contamination in the final solution. The DNA is then precipitated out of the aqueous solution by adding ethanol. Subsequent washes with 70% ethanol help rinse out salts that might have precipitated along with the DNA after which it can be resuspended in the buffer of choice. As an additional precaution we also centrifuge the solution in a micro-centrifuge tube fitted with a filter with a nominal molecular weight marker which facilitates the removal of low molecular weight impurities.

The myriad of restriction enzymes available for modifying DNA opens up the possibility of changing the size of the DNA (N.B.: the restriction maps can be found at the back of the New England Biolabs catalog). We modified the DNA length by using XBa I, an enzyme that cuts λ -DNA into two nearly equal segments of 24,508 and 23,994 base pairs. This results in half-cut DNA which should have a radius of gyration which is smaller than that of λ -DNA by a factor of $1/\sqrt{2}$. The topological structure can also be changed, by ligating the two cohesive ends of lambda DNA. The number of available configurations for the resultant plasmid would be constrained resulting in a change in the entropic attractions studied in this thesis. We were not successful in producing plasmids with the last procedure since ligation produced highly entangled DNA leading to problems in solution homogeneity. However theoretically it should be possible to produce plasmids with an improved technique.

II. Electrophoresis and Spectroscopy

The lengths of the DNA produced through restrictions as well as the possibility

of fragments introduced through handling was checked by gel electrophoresis. The DNA molecule is a strong polyelectrolyte carrying half a unit of negative charge on each base pair. The molecule becomes oriented in a electric field and moves through a gel matrix. The rate at which it moves through the gel is determined by the length of the molecule in addition to other factors. For example, larger molecules move less efficiently since they are more likely to get caught in the pores than smaller molecules. Thus DNA conformation plays an important role and this procedure is often used to distinguish between, circular, nicked and linear DNA. In addition, the properties of the gel also determine characteristic pore sizes which control migration rates. Applied voltages, buffer composition and temperature are other factors that affect gel migration. During gel electrophoresis, the DNA samples are loaded into small wells in the gel along with a marker DNA which is used for calibration. The different DNA's simultaneously migrate across the gel and the distance traveled can be related to the size of the DNA.

We used a 3% agarose gel made with Tris-Borate Buffer. A Teflon comb is inserted into the gel before it sets to create small wells to hold the DNA solution. These serve as the start of 'lanes' along which the DNA migrate. The DNA are stained with Blue/Orange 6X Loading Dye (Promega Corporation) which serves two purposes. It helps the DNA settle in the well which in turn ensures uniform migration through the gel. In addition the visible dye molecule can be used to monitor the DNA migration

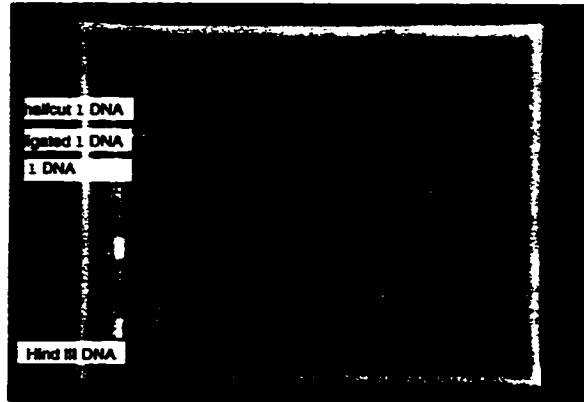


Figure 4.12: A picture of a typical gel. The DNA is stained with Ethidium Bromide and the picture is taken with UV illumination. The three lanes shown contain, half-cut λ -DNA, λ -DNA and ligated λ -DNA. We see that neither of these migrate as far into the gel as the marker DNA which is usually Hind III fragments.

through the gel as it has a mobility which is similar to that of short DNA. Along with the test DNA a calibration DNA such as Hind III Marker (Promega Corporation) fragments are also loaded in one of the wells. The samples are equilibrated for 15 mins at 0V after which a 50V DC signal is applied across the gel for 2 hours or till the dye molecule reaches close to the end of the gel. The gel is then soaked in ethidium bromide which fluorescently stains the DNA molecules allowing each lane to be viewed under a UV lamp. The DNA contour length can be calculated by comparing the distances moved by the calibrated marker DNA and that traversed by the test DNA. A typical gel run is shown in Fig. 4.12.

The concentrations of DNA in solution is checked with a spectrophotometer since DNA has a strong absorption feature at 260nm which is directly related to the number of basepairs in solution. The concentration can be related to the absorbance by Beer's law which is given by

$$c = \frac{A}{\epsilon l} \quad (4.7)$$

Here A is the absorbance, which is defined as the logarithm of the ratio of the incident light, I_0 to the transmitted intensity, I , $A = \log(I_0/I)$. The length of the sample that the light traverses is denoted by l and ϵ is the molar absorptivity of DNA which is $0.02\text{ml}/\mu\text{g}\cdot\text{cm}$. A 0.05 cm long quartz cell was used for the absorption measurements which are carried out in a Perkin-Elmer Spectrophotometer. The quartz cells are cleaned in an ultrasound with methanol prior to use. A typical absorption spectra is shown in Fig. 4.13. The spectra also reveals information on the purity of the DNA since the 260 nm absorption is dominated by the nucleosides whereas at 280nm the absorption results primarily from proteins in solution. This is given by the ratio of the absorbance at 260nm to the that at 280nm. A completely pure sample presents a ratio of 1.8. All samples used here had a ratio that was higher than 1.6.

III. Protocols

Handling DNA calls for several protocols that are usually not commonplace in physics laboratories. A relatively clean environment with sterilized water and containers is needed since bacterial contamination must be prevented. All micro-pipette

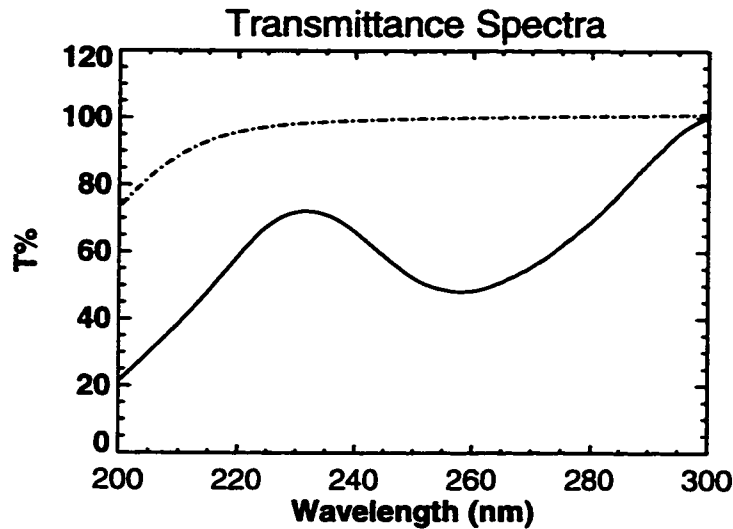


Figure 4.13: An absorption spectra for a DNA solution. The dashed curve represents the absorption spectra of the buffer taken in a quartz cell. The increase in absorption around 200nm arises due to the cut-off of UV transmission in that regime due to the container. The DNA absorption is pronounced at 260nm.

tips, micro-centrifuge tubes and buffer solutions were autoclaved (i.e. they were sterilized at high pressure at 120° C for 20 minutes). The DNA is stored at -20° C and freeze thaw cycles are minimized to reduce sample degradation. The commercially obtained λ -DNA is fairly robust. However, the filled in, ligated and half cut DNA are more susceptible to degradation. Additional measures such as blunt edged pipettor tips and slow stirring are used to prevent DNA breakage. Pipetting small volumes of viscous fluids is highly susceptible to error. To avoid variances in concentrations all DNA solutions were weighed on a sensitive Denver Instruments balance (M220D) which has an accuracy of 0.01gm.

IV. DNA Labeling

It is also possible to directly visualize DNA in the microscope by labeling the DNA with a fluorescent dye such as Ethidium Bromide, Acridine Orange or YOYO-1 [87, 88]. Most of these dyes are weakly fluorescent in solution, however upon DNA binding the fluorescence activity is greatly enhanced. For example, YOYO-1 has been shown to produce enhancement factors of 1400 [87] making DNA visualization relatively easy. Binding occurs by intercalation between the base pairs. Ethidium Bromide and Acridine Orange fully intercalate between the base pairs and have strong electrostatic interactions with the phosphate groups. YOYO-1 also intercalates between the base pairs though full intercalation usually takes much longer than it does for the other dyes. However all degrees of intercalation leads to an increase in DNA contour length.

All visualizations of DNA were done with YOYO-1 (Molecular Probes Inc.) labeling. This dye absorbs in the blue (491nm) and emits in the green (509nm) which is very similar to the commonly used dye, fluorescein. This makes it convenient to use as most microscopes are fitted with a FITC filter ¹ to accommodate these wavelengths. The manufacturer recommends incubating one YOYO-1 molecule per 20-50 DNA base pairs for 2 hrs. For quick and easy visualization we found that diluting the stock dye solution to 1 ng/ml and incubating with the DNA for 10 minutes provided samples that could be easily visualized.

¹FITC is an acronym for the dye, fluorescein isothiocyanate, and is commonly used to label processes that need blue excitation and emit in the green.

The biggest problem encountered in DNA visualization is bleaching. The free oxygen in the solution reacts with the dye molecule in the presence of light, quenching fluorescence activity. Visualization under a 100W arc lamp leads to bleaching in a couple of seconds. Therefore low intensity laser excitation on the confocal microscope was used to produce most of the images presented here. The 488nm line of an Argon-Krypton laser was used to excite the dye molecules. Motion of the DNA coupled with bleaching exclude the use of averaging techniques. Reasonable images were obtained when the illuminating intensity was kept at 30 percent of the available power and the gain of the photomultiplier tube was turned up. Addition of anti-fade agents, also helped increase the visualization time. A mixture of glycerol, glucose oxidase and catalase was used as an oxygen scavenger. Each milliliter of Tris-HCl buffer contained 100 μ g of catalase, 500 μ g of glucose oxidase and 100 μ g of glucose (all chemicals can be obtained from Sigma). Visualizing times could now be extended to 15 -20 minutes. Fig. 4.14 displays various images of DNA obtained under the microscope.

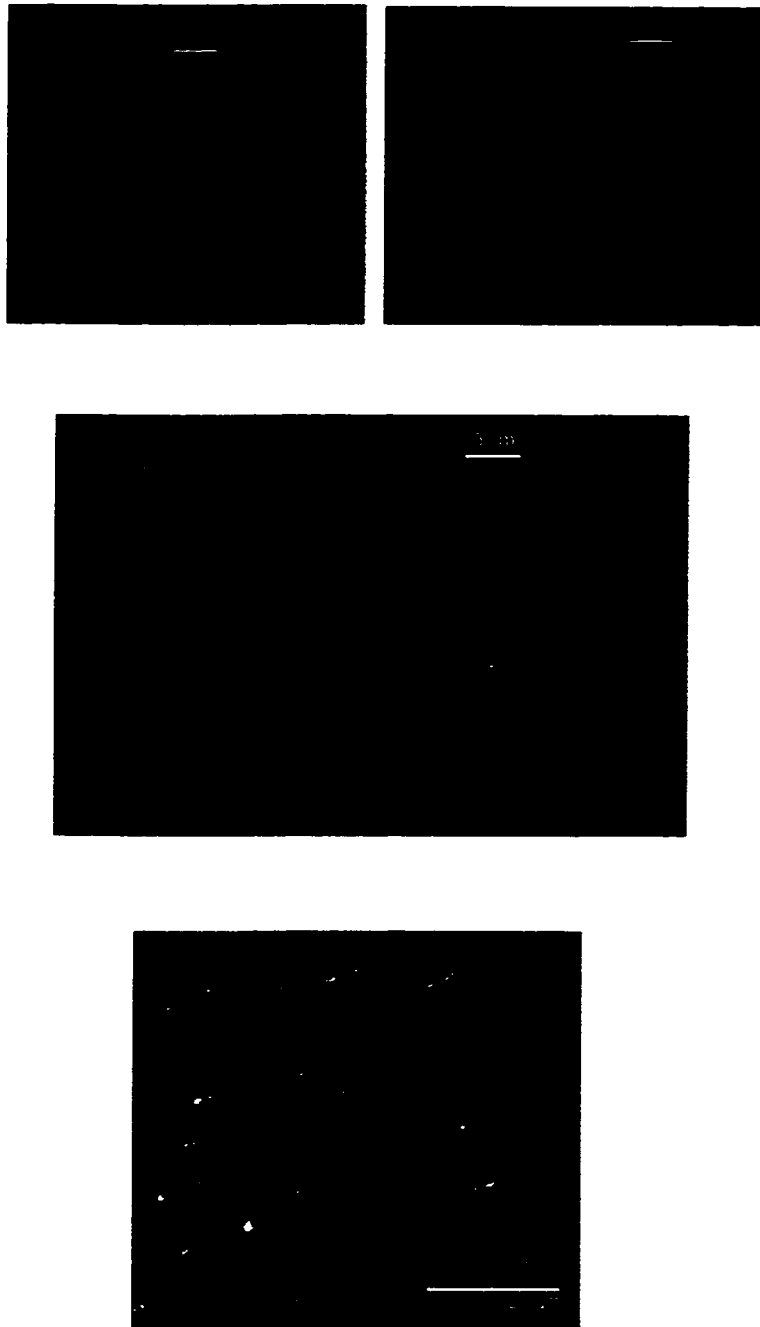


Figure 4.14: Fluorescent images of DNA with YOYO labelling. In (a) we see two different views of K-DNA which is formed by a number of interlinking plasmids forming a cup like structure. In (b) we see images of λ -DNA. Individual coils can be visualized and seen to re-arrange their configuration. In (c) the λ -DNA have been stuck to the glass and stretched out by a controlled convective drying process. The entire length of the DNA can be visualized and measured.

Chapter 5

Equilibrium Interactions

So far we have discussed the theoretical and experimental background needed to explore the interactions that arise in colloid-polymer mixtures. In this chapter we present measurements that probe the functional form of the interaction potentials in these suspensions. We explore the nature of these potentials over a wide range of polymer concentrations from dilute solutions to the semi-dilute regime in which polymers coils are strongly entangled.

This chapter is organized as follows. In Section 5.1 we review the general experimental procedures that were used to measure the depletion potentials in DNA solutions. In the next section, Section 5.2, we discuss the methods used for data analysis. Details about how we extracted measured potentials from raw images is presented in this section. The results are presented in Section 5.3. Here the scaling of the fitted parameters, i.e. the osmotic pressure and the radius of gyration, are compared with theoretical predictions. Physical properties such as the second

virial coefficient and solvent quality are extracted from our measurements and then discussed extensively in Section 5.4. Finally in Section 5.5 we explore how the interaction potential changes as we vary polymer-colloid size and the background ionic strength of the solvent. The last section briefly summarizes the work.

5.1 General Experimental Procedures

We measured two-particle interactions with colloidal silica spheres in a background solution containing λ -phage DNA. The particles were trapped on an optical line tweezer and their motion was imaged for 30 minutes at video rates. The data collection time periods were extended to an hour when the potentials were weak in order to improve the statistical accuracy of the data. Throughout the course of the experiment we monitored the laser trapping power and the distance of the laser focus from the microchamber wall. Because changes in laser intensity can lead to variations in the strength and the shape of the potential, the laser power must be kept constant. The laser intensity was monitored using the light reflected by a pick-off mirror that was inserted in the beam path. At this spatial position the laser power was $\sim 13\text{mW}$ and fluctuations were kept to within 0.5mW , by manual adjustments.

The distance between the coverslip and the laser focal plane varied as a result of a mechanical flaw in the nosepiece of the Zeiss microscope. Occasional and irregular mechanical drifts caused the focus to drift upward toward the coverslip wall. These

distance variations could lead to changes in the shape of the optical potential due to changes in the focusing characteristics of the beam. In addition the observed potentials could be distorted as added interactions between the particles and the wall could affect the particle dynamics. To minimize these detrimental effects, the microscope focus was adjusted every three minutes. The focal depth from the wall was optimized at $3\mu\text{m}$, which is approximately three times the maximum polymer size. These distances are large enough to avoid wall effects, yet short enough so that the trap is not weakened by spherical aberration. At larger depths the out-of-plane motion of the silica spheres increased thereby indicating that the strength of the optical trap had weakened. The distance from the chamber wall was monitored by a focus-drive motor (ASI, Model MFC-1) that controlled the focus of the microscope. While holding two beads in the line trap the focal plane (which also defines the position of the line trap) is lowered to the coverslip wall which causes the image of the two spheres to blur. This indicates that the trap position has reached the coverslip wall. We define this as the zero position and for our experiment the focal plane was moved $3\mu\text{m}$ into the sample. This technique would usually yield an accuracy of $\pm 0.5\mu\text{m}$ in the measurement of the focal distance.

We also made measurements on samples containing only silica spheres suspended in buffer (TE buffer) solution. These were then used to remove optical effects from our sample measurements, which will be discussed in detail in the next section. The

buffer measurements were made immediately before and after each DNA sample so that differences resulting from drifts were minimized.

5.2 Calculation of the Potential

Video images were digitized and analyzed in accordance with the procedures discussed in the previous chapter. Particle positions were extracted using these methods; these data were then used to calculate interaction potentials. If the system is in equilibrium, then the probability, $P(\mathbf{r})$ of finding the two spheres with centers separated by r is related to the free energy of the system through the Boltzmann relation, $P(\mathbf{r}) \propto \exp(-U(\mathbf{r})/k_{\text{B}}T)$, where $U(\mathbf{r})$ is the free energy, k_{B} is the Boltzmann constant and T is the temperature. We estimate this probability distribution from a histogram of the measured separations and then calculate the interaction free energy by taking the natural logarithm of this distribution.

There are two features of the line tweezer that aid in estimating the probability distribution, $P(\mathbf{r})$. The line tweezer creates an optical potential that confines the spheres in the y and the z direction, but allows them to freely diffuse over a certain distance in the direction of the scan, i.e. the x direction. Along the scan direction, particle diffusion is limited to the length of the line scanned by the laser beam. This optical cage along the x direction is highly desirable as it forces the two particles closer together and thus reduces data collection times. In addition to the statistics

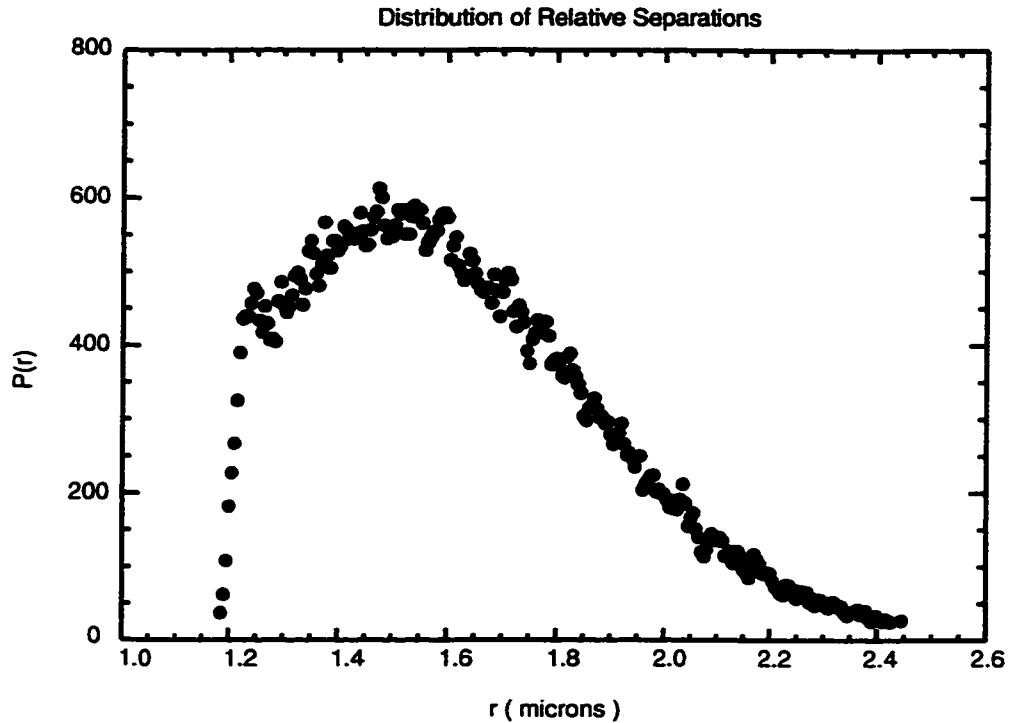


Figure 5.1: A typical probability distribution function that is obtained for the relative separation between two particles in a buffer solution

required to accurately characterize the potential we also need to be able to determine the three dimensional inter-particle separation, r . In a typical microscope image in which particles are not confined, it is only possible to measure the two-dimensional projection of the actual three dimensional separation. The line tweezer confines the motion of the particles to the focal plane (within 50nm); thus the two dimensional separation is equal to the three dimensional separation of the spheres. This greatly increases the spatial resolution of our measurements.

Although the line tweezer is a useful tool that aids in improving measurements of the probability distribution, it also introduces optical forces that complicate the

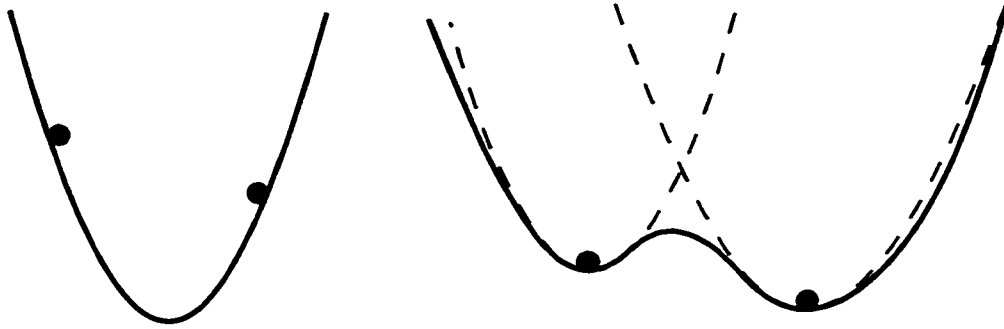


Figure 5.2: In (a) we see a parabolic potential characterized by a spring constant, k . In (b) the strength of the potential is characterized locally by parabolas (dashed lines) which have different spring constants. This does not allow for a separation of the potential into a contribution from the relative co-ordinate and the center-of mass coordinate

interpretation of the measured distributions. The measured free energy now contains contributions from the trap in addition to the entropic attraction we wish to probe. One of these forces arises due to the optical cage that exists along the scan direction. The motion of the particle is determined by the shape of the potential created by the laser beam, which in turn depends on the subtleties of the scanning characteristics. For example, if the laser beam slows down during the middle of the scan, the higher time averaged field attracts the particle to the center of the scan region. Such spatial variations in the trapping characteristics affect the probability distribution, $P(\mathbf{r})$, of the particles and are apparent in the measured potentials. In addition the light can also induce dipole moments in the dielectric spheres which then interact to produce short range repulsions. The latter effect is found to be minimized by choosing light that is polarized perpendicular to the scan direction.

The optical artifacts introduced by the line tweezer can be removed for some simple

cases, such as a ‘flat or a parabolic optical potential. If the optical potential is spatially independent over the region of interest then the measured potential only depends on true interactions in the suspension. However if the trap has spatial variations then at each point in space there is a force that is exerted on the particles. The total force on each sphere is the sum of the entropic forces and the trap induced forces. In the harmonic approximation, the total force on the i th sphere can be written as

$$\mathbf{F}_{tot}^i = \mathbf{F}_{ent}^i - k_i(r_i)(\mathbf{r}_i - \bar{\mathbf{r}}_i) \quad (5.1)$$

where the local strength of the trap is characterized by $k_i(r_i)$. The equilibrium position of each particle is given by $\bar{\mathbf{r}}_i$ and F_{ent} represents the entropic force. For two particles in such a trap the effective potential U_{total} is given by

$$U_{total}(\mathbf{r}_1, \mathbf{r}_2) = U_{ent}(|\mathbf{r}_1 - \mathbf{r}_2|) + \frac{1}{2}k_1(r_1)(\mathbf{r}_1 - \bar{\mathbf{r}}_1)^2 + \frac{1}{2}k_2(r_2)(\mathbf{r}_2 - \bar{\mathbf{r}}_2)^2. \quad (5.2)$$

Here $U_{ent}(|\mathbf{r}_1 - \mathbf{r}_2|)$ represents the entropic interaction potential we are interested in measuring and it only depends on the relative separation of the two particles, $\mathbf{r} \equiv |\mathbf{r}_1 - \mathbf{r}_2|$.

If the optical potential is spatially independent then the last two terms in Eq. 5.2 are constants that just provide an additive offset to our data. On the other hand if the trap is parabolic, $k_1 = k_2 = k$ then U_{total} can be rewritten as

$$U_{total}(\mathbf{r}, \mathbf{R}) = U_{ent}(\mathbf{r}) + \frac{1}{2}k\mathbf{r}^2 + \frac{1}{2}k\mathbf{R}^2 \quad (5.3)$$

where $\mathbf{R} = \frac{1}{2}(\mathbf{r}_1 + \mathbf{r}_2)$ is the center of mass co-ordinate of the two particles and $\mathbf{r} = (\mathbf{r}_1 - \mathbf{r}_2)$ is their relative position co-ordinate. Since the entropic interaction potential we are interested in measuring depends only on the relative co-ordinate, we can decouple the interaction potential into two parts; one that depends solely on the relative separation of the spheres and the other part that depends on the center of mass co-ordinate. This would not be possible for potentials which cannot be approximated by a single harmonic well such as those shown in Fig. 5.2. The different optical strengths would lead to optical forces on each particle that could not be easily separated from the entropic forces. To verify the validity of our data, we made independent measurements to ensure that the potential is parabolic. This was done by trapping a single particle and calculating its potential from a histogram of its positions. The motion of the particle maps out the shape of the potential which is shown in Fig. 5.3, which is indeed parabolic.

In the special case in which the optical potential can be exactly determined, the above constraints can be relaxed. For our experiments we use a subtraction technique that allows us to remove the optical effects. This is shown in Fig. 5.4. We measure the potential between two spheres in a buffer solution that is DNA-free. This serves as our background potential and is subtracted off from the potentials measured with DNA in solution. We fit the background potential measured in the pure buffer solution to a second order polynomial outside the repulsive core region. This reduces artifacts

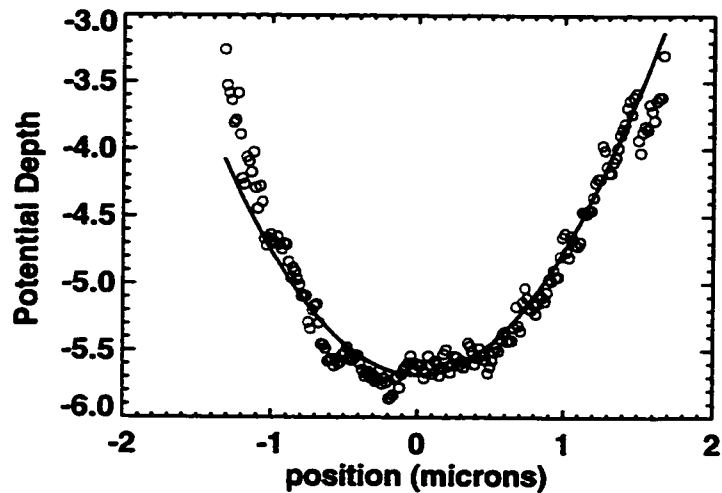


Figure 5.3: A typical optical potential. The solid line is a parabolic fit with a spring constant of $\approx 0.5k_B T/\mu\text{m}^2$. The potential is measured by trapping a single particle in the trap and letting it trace out the optical forces.

that might arise due to polydispersity and also prevents the introduction of additional noise. Fig. 5.4(a) shows a typical buffer potential with an overlaid parabolic fit.

This subtraction technique relies on the fact that the optical properties of the solution do not change when DNA is added to the solution. Thus there are no changes in the trapping characteristics and the buffer measurements accurately represent the optical potential. In our measurements the optical properties (i.e. the refractive index) do not change noticeably over the range of DNA concentrations used. If this optical potential was not parabolic we would also need to apply an additional criterion which would require us to sample all possible center-to-center separations. For example, if the background optical potential was not separable into center-of-mass co-ordinates, \mathbf{R} , and relative co-ordinates, \mathbf{r} (Eq. 5.3), then measurements made in

the \mathbf{r} co-ordinate system would depend strongly on the value of the \mathbf{R} co-ordinate. Theoretically this effect can be eliminated by averaging over all possible ensembles. However, experimentally it is difficult to explore the entire phase space.

5.3 Interaction Potentials

To quantitatively interpret our data we turn to the depletion models described in Chapter 3. We utilize all three models, i.e. the AO Model (Eq.3.4), the mean-field predictions (Eq.3.28) as well as the interaction free energy that is predicted for two point like particles (Eq.3.17). In all cases we let the osmotic pressure, Π and the correlation length be free parameters and obtain values from the best fits. Fig. 5.5 shows the measured interaction potential at a DNA concentration of $140\mu\text{g/ml}$ with overlaid fits. We see that attempts to fit the potential to the Yukawa like free energy of interaction predicted for two point spheres (Eq.3.17) is not successful. The fit underestimates the depth of the potential and fails to describe the shape at large distances. On the other hand the potentials can be well described by the AO Model as well as the mean-field model. This is not surprising since the second order terms of the two models are identical (see Chapter 3, Section 3.4). The importance of the third order term in Eq.3.29 can be determined by looking at the ratio, $(r - \sigma\lambda)/(3\sigma\lambda)$. For our experimental conditions, this ratio varies from 0.33 in the dilute limit to 0.08 in the semi-dilute region, reducing the significance of the third order term.

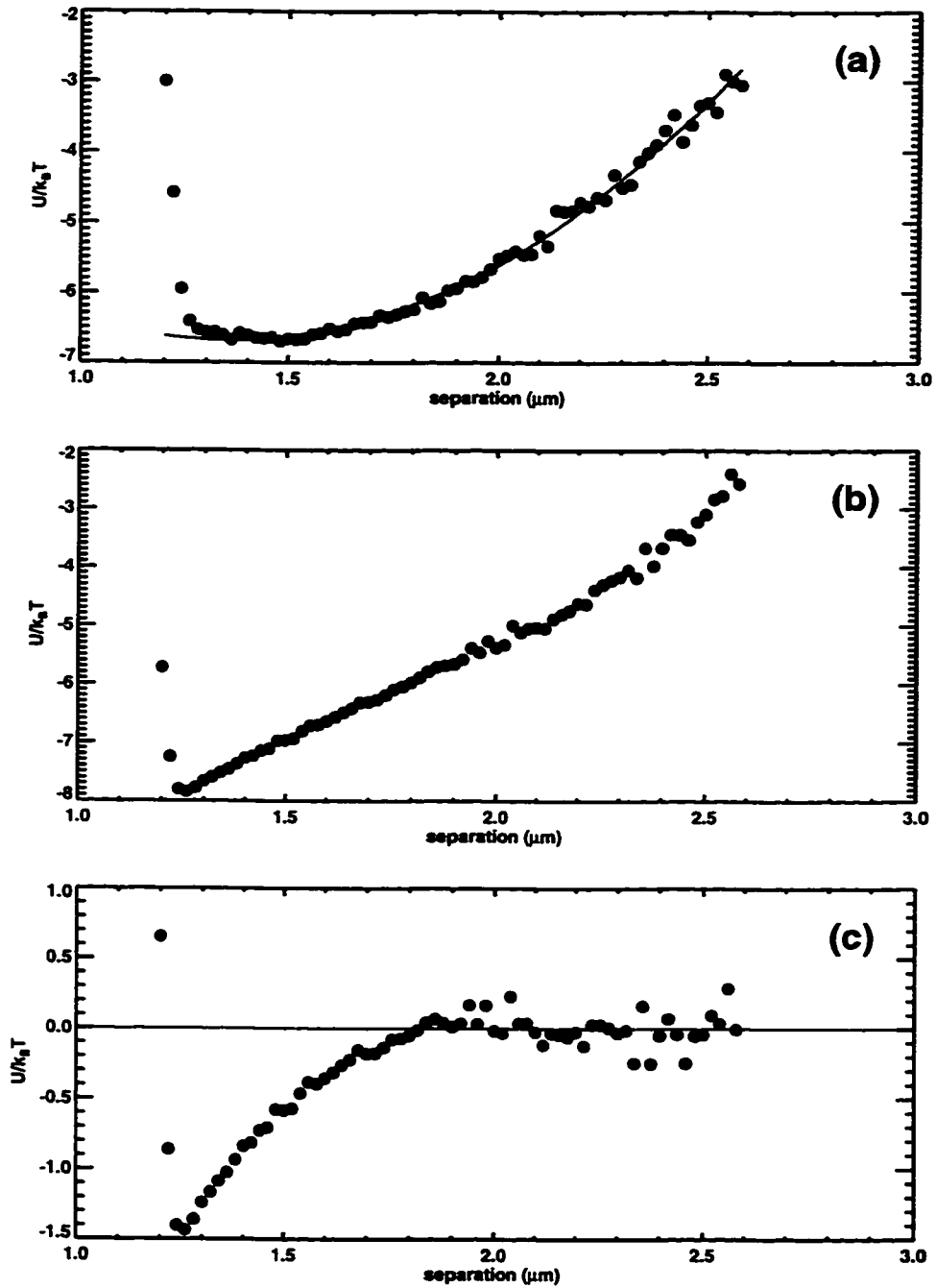


Figure 5.4: The filled circles in (a) and (b) represent the raw potentials measured in a pure buffer solution and a DNA solution respectively. The solid line in (a) represents a fit to a quadratic function. The third plot (c) shows the result of subtracting the solid fit from the measured potential shown in (b). This removes the optical effects if the optical properties of the solution haven't changed. The flattening of the final potential (c) indicates that indeed the optical potential between (a) and (b) did not change for the two samples.

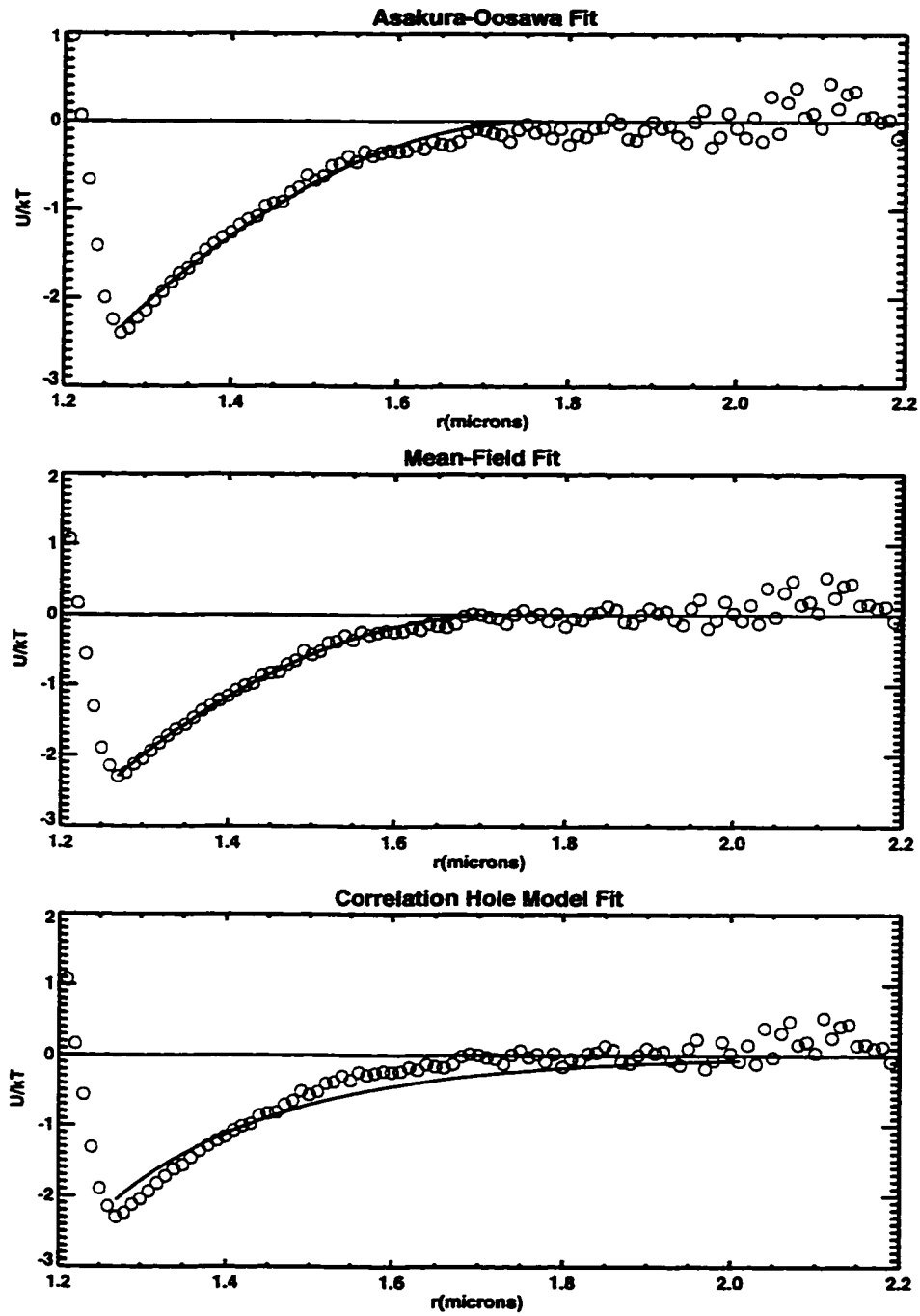


Figure 5.5: Fits to the (a) Asakura-Oosawa Model, (b) Mean-Field Model and (c) the Correlation Hole picture is shown in the above graphs. All curves were offset so that at large separations the interactions were zero. All the solid lines represent best fits with a two parameter fit to the models described in the text.

In this section we choose to leave in the third order term and adopt the Asakura-Oosawa (AO) depletion model to interpret our data. Our measured potentials are fit with Eq.3.4 treating Π_p and R_p as free parameters. Since our method only determines the potential up to an undetermined additive offset, we shift the potential curves vertically so that the potential at long-range is zero.

The resulting potentials for all measured DNA concentrations display a long-range attraction. The lower concentrations exhibit shallow potential wells and the longest interaction range. As the concentration is increased, the potential wells get progressively deeper and the range contracts dramatically. Throughout the range of concentrations explored, we observe a shrinkage in the range of the well from $1\mu\text{m}$ to about 300nm and, at the same time an increase in well depth from $0.5k_B T$ to $5k_B T$.

We can then divide our observations into measurements in the dilute regime and the semi-dilute region. For λ -DNA the crossover concentration that divides these two regimes can be calculated from the size of an ideal coil. Since the persistence length for λ -DNA is 50nm and the contour length is $16\mu\text{m}$, the effective radius of gyration is calculated to be $R_g = \sqrt{2Ll_p/6} \sim 510\text{nm}$. This yields a crossover concentration value of $c^* = (N_A/M_W)((4\pi R_g^3/3))^{-1} \sim 60\mu\text{g/ml}$, which is roughly consistent with mobility measurements that probe, c^* . Pernodet *et al.* [89] use gel electrophoresis to study the the mobility of fluorescently labeled DNA at different concentrations, and determine the overlap concentration to occur around $35\mu\text{g/ml}$.

5.3.1 Dilute Region

The measured interaction potentials for the dilute regime is shown in Fig. 5.6. In the dilute solution the effective polymer radius R_p should equal the radius of gyration of the polymer, R_g and the fitted osmotic pressure should depend linearly on DNA concentration c , n_p (i.e. $\Pi_p = n_p k_B T$). Here n_p represents the number of polymer coils in solution and can be related to the monomer concentration through $n_p = c/N$, where N is 48,502 for λ -DNA. The first three data points in Fig. 5.9 and Fig. 5.8 correspond to the fit parameters of the dilute regime. The observed trends agree with the predictions for a dilute polymer solution– the effective diameter of the polymer is measured to be $1.1 \pm 0.2 \mu\text{m}$ and is independent of the concentration. This value also agrees well with light scattering measurements for R_g [89] in similar buffers which yield $R_g \sim 500\text{nm}$.

The osmotic pressure displays a nearly linear behavior, although the measured prefactor of 0.5 ± 0.3 obtained for this fit deviates from the expected hard-sphere value of unity. The relatively large error for the parameters in the dilute limit is a result of the shallow well-depth of the interaction curves. In addition the long range also tends to increase the uncertainty in determining their vertical offset. On the other hand the deviation in the prefactor might arise because the effective volume occupied by the polymer (i.e. the multiplicative volume term in Eq. 3.4) can no longer be described by a sphere [62]. For instance any anisotropy in the random walk configuration could

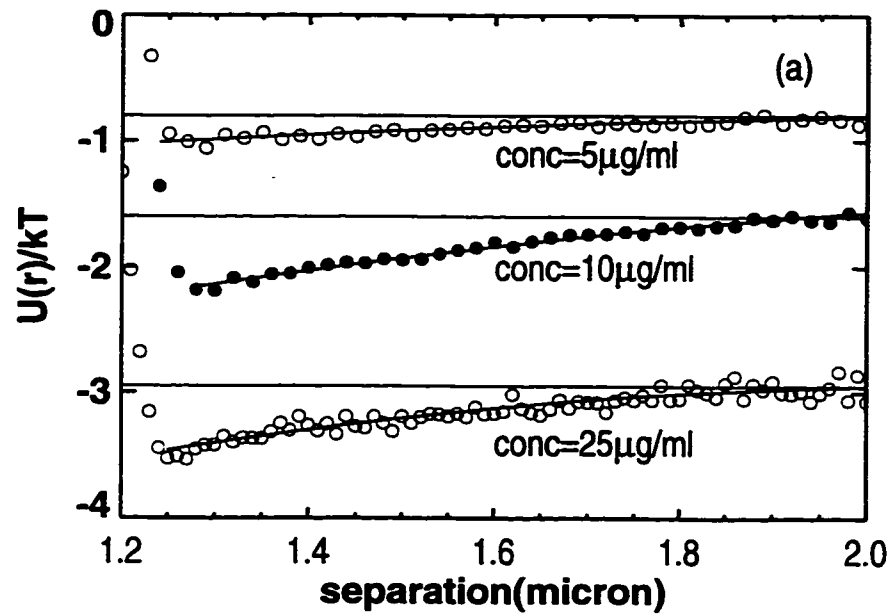


Figure 5.6: The measured interaction potentials in the dilute regime. The filled circles are measured data points and the solid lines are fits to the AO Model

lead to non-spherical distributions whose effects could be partially accounted for by a different multiplicative pre-factor in the equation for the interaction potential. The reduction in the prefactor has also been attributed to polymer-polymer interactions. Neutron scattering experiments that probe the structure factor of colloid polymer solutions observe a similar reduced linear virial coefficient [25, 90].

From our measurements in the dilute regime we can conclude that the Asakura-Oosawa model provides a good fit to the depletion potential. We are able to extract a range and an osmotic pressure, from our potentials. We find that the polymer size we probe does not change with concentration, an observation that is consistent with the predictions in the dilute concentration regime. However the osmotic pressure deviates from the expected linear virial predictions. Currently measurements on half-cut λ -DNA are underway to reduce the uncertainty in the dilute regime measurements. This will enable us to better understand the origins of the measured deviations.

5.3.2 Semi-Dilute region

The behavior of the interaction potentials changes dramatically in the semi-dilute regime. Beyond the critical concentration, the range of the potential starts to contract and the depth increases significantly. The potentials are shown in Fig. 5.7. A best fit to parameters extracted from the data yields $R_p = (0.4 \pm 0.05)n_p^{-0.5 \pm 0.1}$ and $\Pi_p/k_B T = (0.8 \pm 0.2)n_p^{2.2 \pm 0.2}$ where R_p is measured in μm and n_p and $\Pi_p/k_B T$ in $(\mu\text{m})^{-3}$. The

relationship between the ‘effective size’ and n_p has a measured scaling exponent of -0.5 ± 0.1 . This strongly suggests that the polymer solution lies in the weakly fluctuating regime for semi-flexible polymers. The $-3/4$ exponent predicted for the strongly fluctuating semi-dilute region (V) lies outside the measured error bars. The exponent corresponds with the predictions that are made for a correlation length, $\xi \sim n^{-1/2}$ and not for what is expected for the radius of gyration, $R_g \sim n^{-1/8}$ [16]. This indicates that range of the interaction is determined by the correlation length and it further corroborates our substitution of $(\pi/2)\xi$ for R_p in the AO model (see Chapter 3, Section 3.4).

The measured exponent of 2.2 ± 0.2 for Π_p as a function of n_p , has too large of an error to distinguish the predictions of 2.25 for the strongly fluctuating regime from the value of 2 for the weakly fluctuating region. This is probably a result of the greater uncertainty associated with the well depth measurements.

We also examined the dependence of the pressure versus the correlation length. This plot further confirms that the semi-dilute DNA solution lies in the weakly fluctuating phase where two point contacts dominate. In this regime mean-field theory predicts that the pressure is related to the correlation length [16] through

$$\Pi = k_B T / \xi^4 \quad (5.4)$$

From Fig. 5.10 we see that our data exhibits an exponent of -3.9 ± 0.1 which corresponds closely to the mean-field prediction, but excludes the value of -3 that is

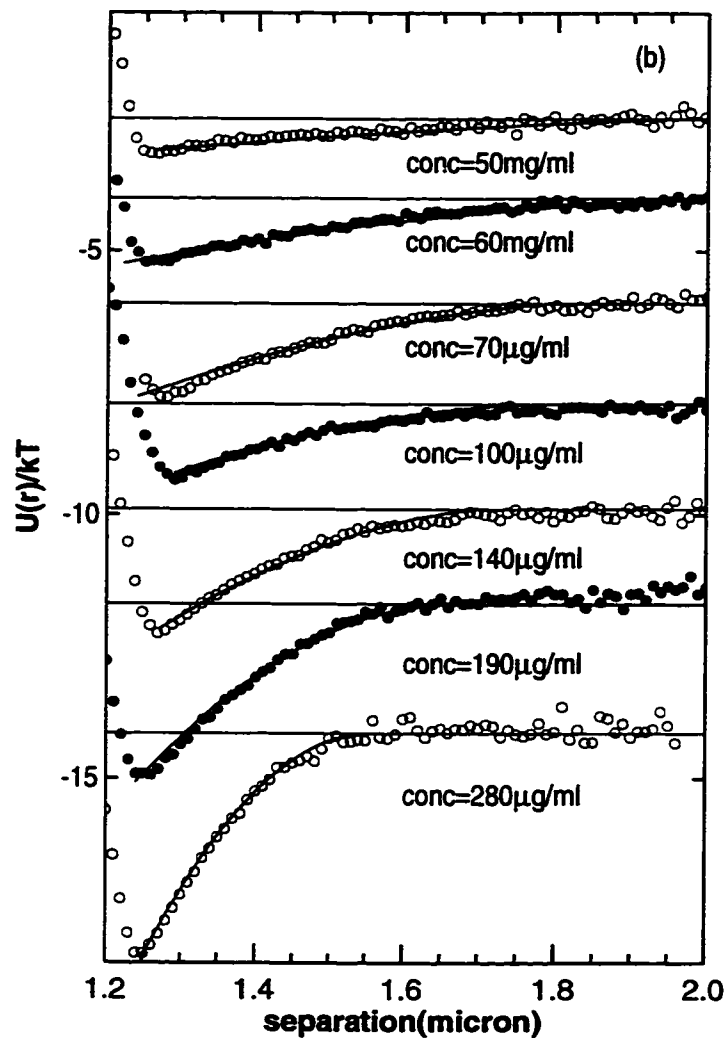


Figure 5.7: The interaction potential between two $1.25 \mu\text{m}$ silica spheres, in (a) the dilute and (b) the semi-dilute region. The dimensionless potential $U(r)/k_B T$ is plotted as a function of r , the inter particle distance. The open circles represent actual data points and the solid lines are fits to the AO model, as described in the text.

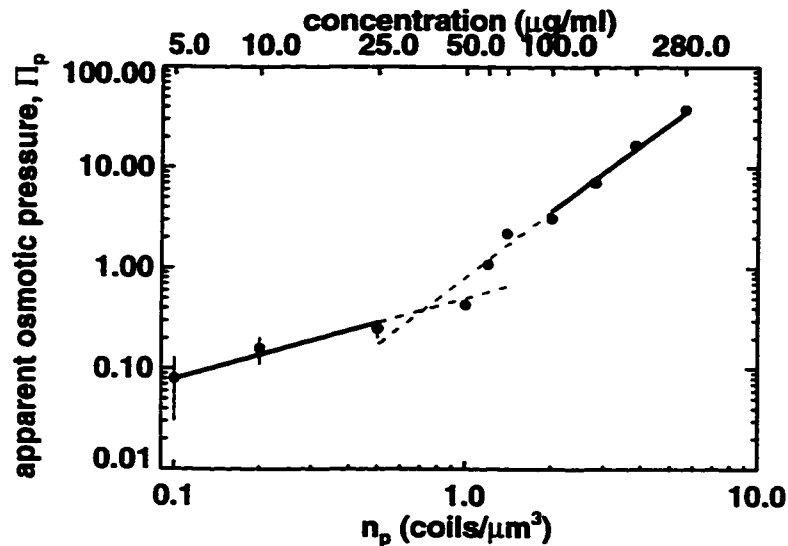


Figure 5.8: In (b) the filled circles represent the fit parameter R_p (we have used $\xi=(2/\pi)R_p$ in the semi-dilute regime) in microns is plotted against different polymer concentrations. The solid lines represent fits to mean field theory predictions and are described in detail in the text. In the graph $n_p^* \approx (4\pi/3)R_p^{-3} \approx 1.0\mu\text{m}^{-3}$ marks the crossover from the dilute to the semi-dilute regime.

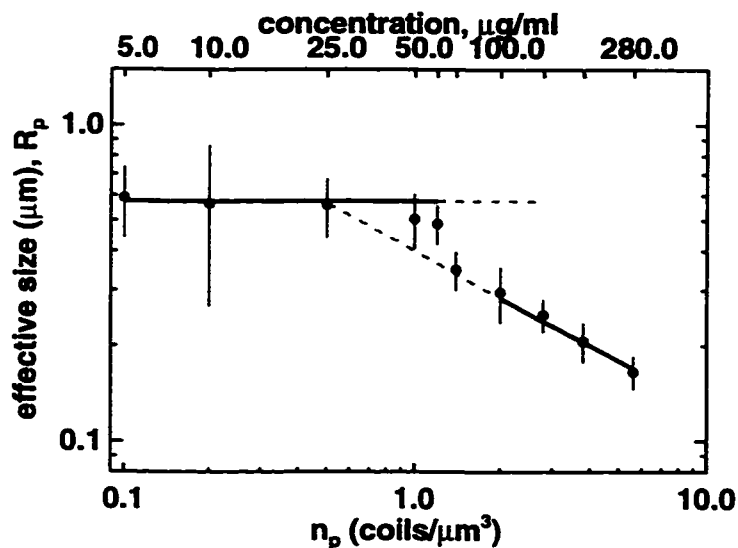


Figure 5.9: In (a) we present the scaling behavior of the osmotic pressure vs. the concentration. The vertical axis represents $\Pi/k_B T$ and the horizontal axis is concentration in units of number density.

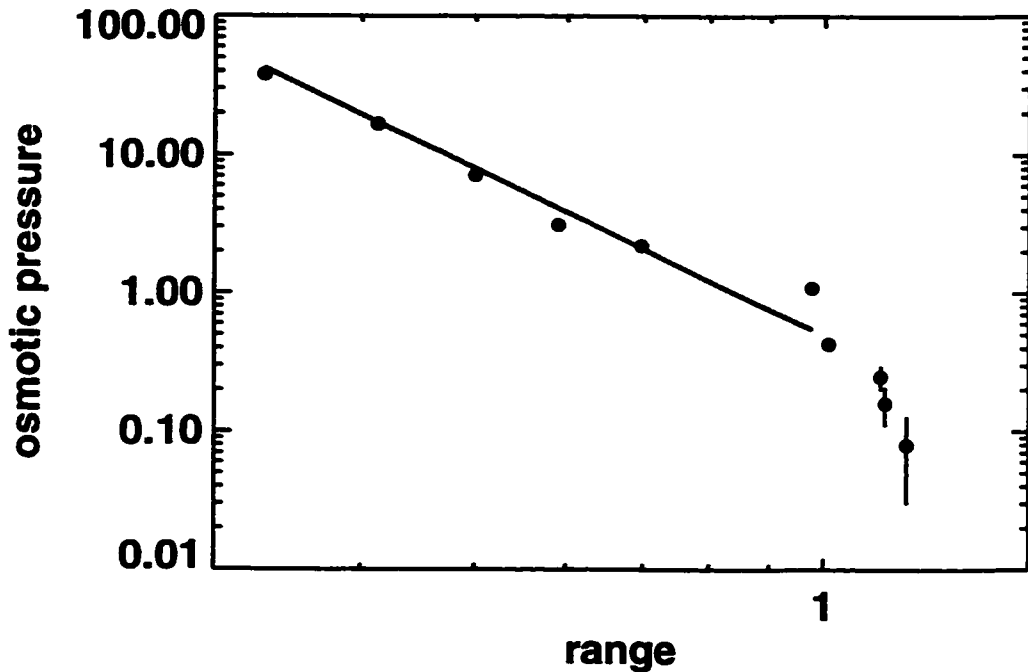


Figure 5.10: In (a) we present the scaling behavior of the osmotic pressure vs. the correlation length. The vertical axis represents $\Pi/k_B T$ and the horizontal axis is proportional to ξ in units of microns. The solid line represents a fit which yields a measured exponent of 3.9 ± 0.1 .

predicted for flexible polymers with strong fluctuations.

5.4 Second Virial Coefficient

Our measurements also allow us to determine the solvent quality of the buffer suspension which is widely used in DNA preparations by microbiologists. A simple measure of the solvent quality is given by the ratio of the measured radius of the polymer coil to the radius of gyration that would be expected in an ideal solvent [17]. This ratio,

α , is usually called the swelling parameter, and from our measurements in the dilute DNA solution we calculate this to be

$$\alpha = \frac{R}{R_{ideal}} = 1.15 \pm 0.2. \quad (5.5)$$

At the theta point, $\alpha = 1$. Thus the value of our swelling parameter indicates that the DNA in our solution is close to being ideal. We can further utilize the swelling parameter to calculate the z parameter (see Chapter 2. Section.2). The swelling parameter, α can be expanded in terms of z to give

$$\alpha^2 = 1 + \frac{4}{3}z + .. \quad (5.6)$$

from which we can calculate a z value of 0.25 ± 0.03 . Since $z = 1$ defines the transition between ideal coils and swollen coils, our measured value of z definitively indicates that our solution lies close to the θ -point. We also use the z parameter to calculate the second virial coefficient, by using the relationship (see Chapter 2, Section 2.4), $B = (z/2)(2\pi/3)^{3/2}(N_{\text{eff}}^{-1/2})l_k^3$. The measured z parameter yields $B = 2.99 \pm 0.4 \times 10^{-5} \mu\text{m}^3$.

The above results are cross-checked by comparing with the measured virial coefficient in the semi-dilute DNA solution. This is estimated from the slope of the osmotic pressure data to be $B = 3.1 \pm 0.8 \times 10^{-5} \mu\text{m}^3$ since, $\Pi_p = BN_{\text{eff}}n^2$. Our measured value can be converted to more conventional units $A_2 = N_A B N_{\text{eff}}^2 / M_w^2$, which yields $A_2^\Pi = 4.8 \pm 1.2 \times 10^{-4} \text{ mol-cm}^3/\text{gm}^2$. This result is comparable with previous light scattering measurements that estimate this number to be $A_2^\Pi = 2.8 \pm 1.2 \times 10^{-4} \text{ mol-cm}^3/\text{gm}^2$ [20].

The known second virial coefficient, and the relationship between B and z (Eq.2.31 from Chapter 2), enables us to calculate a value for the z parameter from the semi-dilute results. This yields $z = 0.248 \pm 0.01$ which is very similar to the results obtained from the dilute regime estimates. This further confirms the interpretation of our data.

Another internal consistency test of the interpretation of our data, compares the measured correlation length $\xi_m = (2/\pi)R_p$ with the theoretically predicted correlation length $\xi_t = l_p(6BN_{\text{eff}}n_p)^{-1/2}$ that can be calculated using the measured B . This predicts that $\xi_t n_p^{1/2} = (0.28 \pm 0.03)\mu\text{m}^{1/2}$, whereas, $\xi_m n_p^{1/2} = (0.25 \pm 0.03)\mu\text{m}^{1/2}$. These numbers agree within error estimates.

The measured z parameter can be used to precisely place our experiment on the phase diagram for semi-flexible polymers. Using the persistence length and the number of effective links, N_{eff} we can calculate a phase diagram for our solution following the discussion in Chapter 2. The expected phase diagram for DNA with our measured second virial coefficient is shown in Fig. 5.11. The cross-section sampled by our experiments is shown in the diagram as a dashed line. We calculate the τ value from our measured second-virial coefficient by using the relationship, $\tau = B/(dl_p^2) \sim 6 \pm 1$. We see that our experimental results lie close to the theta point. At our calculated value of z , our data traverses Region I where we expect a dilute solution of Gaussian coils and then passes into Region VII. This region looks similar to Region I in terms of observable characteristics (i.e. variations of π and ξ) and could

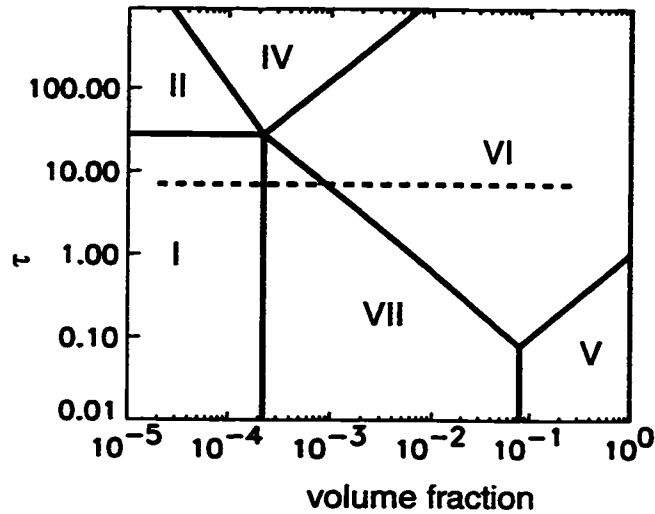


Figure 5.11: The DNA phase diagram, calculated by using the values measured from the interaction potential. The dashed line represents the phase space explored in this experiment.

explain why our measured overlap concentration appears to be higher in value than the calculated c^* . For further increases in DNA concentration, the polymer solution enters regime VI which is consistent with the scaling characteristics we observe. This is an unambiguous test of the theory of semi-flexible polymer solutions that has not been seen clearly to date.

Size Ratio Effects

As a control, we also measured the depletion effect with a different sized colloidal sphere. The potentials for the two different sizes, $1.25\mu\text{m}$ and $1.55\mu\text{m}$, at a DNA concentration of $60\mu\text{g/ml}$ are shown in Fig. 5.12. We see that the hard sphere repulsion for the two sizes turns on at different separations as would be expected. The

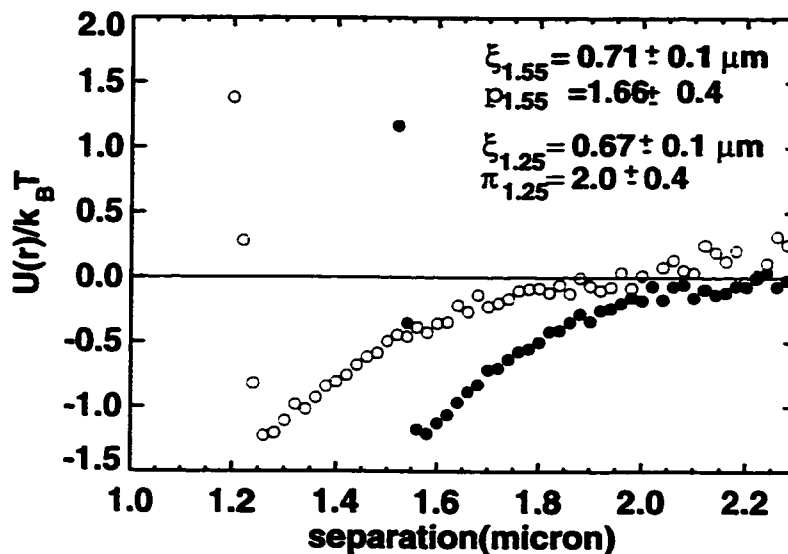


Figure 5.12: The interaction potential between two different sized spheres measured in DNA solution of $60\mu\text{g/ml}$. The filled circles represent the interaction potential between the $1.25\mu\text{m}$ and the open circles represent the $1.5\mu\text{m}$ spheres.

parameters obtained for correlation lengths and osmotic pressures are similar within error bars, as would also be expected. This lends further credence to the fact that the observed depletion potential arises due to polymer induced entropic contributions and is not an artifact of the sphere size chosen.

5.5 The Effects of Monovalent Salt

We investigated the changes in the depletion attraction that arise due to changes in the ionic strength of the solution. The salt concentration is used to control the repulsive attractions between the DNA links. By decreasing the amount of monovalent salt the range of electrostatic interactions can be increased. The Tris-HCl salt concentration

was varied from 0.1mM to 50mM. changing the screening length from $\sim 30\text{nm}$ to $\sim 1\text{nm}$. As a result of the increased repulsion range the persistence length changes dramatically. From previous measurements of force versus extension on *dsDNA*, an exponential change in l_p from 0.5mM to 50mM is observed. The persistence length goes from $0.9\mu\text{m}$ to $0.5\mu\text{m}$ over this range [12]. This leads to a change in the number of effective links. For λ -DNA, N_{eff} goes from being 160 to ~ 80 .

We measure the entropic interaction potential in each of these buffers. At the low salt concentrations the DNA was precipitated from the regular TE buffer by phenol-chloroform extraction and resuspended with care in low salt Tris buffer. At the high salt concentrations, 25mM and 50mM, small amounts of the surfactant ($\approx (0.2-0.8) \times \text{CMC}$ where $\text{CMC} = 2.7 \times 10^{-4}\text{mol/kg}$, 59 micro-molar), Tween 20 (polyoxyethylene sorbitol esters), was added to the solutions to maintain colloidal stability. Surfactant concentrations were kept below the critical micelle concentration (CMC) to prevent attractions that might arise due to micellar depletion. Control measurements of intersphere potentials in DNA solutions, were made in regular TE buffer (10mM Tris-HCl) as well as in TE buffer that contained surfactant (once again surfactant concentration was under CMC) to determine whether Tween 20 had adverse effects on the DNA coils. No differences were observed when the potentials are compared. However even in the presence of surfactant we could not explore solutions with salt concentrations higher than 50mM. Colloidal stability was destroyed which lead to irreversible particle

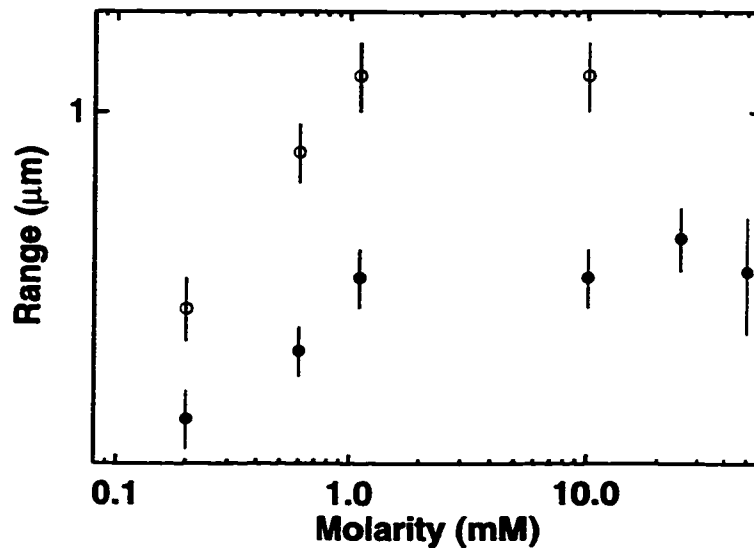


Figure 5.13: The interaction potential in solutions containing different amounts of monovalent Tris-HCl. The ranges of the potentials were measured in the dilute regime ($20 \mu\text{g/ml}$) (open circles) and the semi-dilute regime ($100 \mu\text{g/ml}$) (filled circles). Surprisingly the range shrinks at low salt concentrations.

aggregation.

The potential between the two silica spheres was measured at different salt concentrations in both the dilute ($20 \mu\text{g/ml}$) as well as the semi-dilute regime ($100 \mu\text{g/ml}$). No significant changes were observed for salt concentrations between 10mM and 50mM . This trend is similar to light scattering observations [21], in which no significant change was observed in the measured radius of gyration. However the potential at small salt concentrations (0.2mM , 0.5mM and 1mM) yielded anomalous short range potentials. The measured correlation lengths decreased in size as the salt concentration was lowered. Previous measurements on DNA with different monovalent salt



Figure 5.14: A YOYO-1 labelled DNA in 0.1mM buffer. In general the DNA images appear to be more anisotropic than in regular 10mM buffer.

concentrations have shown that the persistence length increases dramatically [87] at low salt concentrations. This effect leads to a reduction in the number of effective links, strongly affecting the anisotropy of the polymer. One possibility for a decreased range of the potential could arise due to this anisotropic distribution of links. In fact, direct visualization of λ -DNA in the 0.2mM buffer shows a more anisotropic distribution of links than what is seen in the regular 10mM buffer. Fig. 5.14 an image of DNA in 0.1mM Tris solution. Individual DNA molecules in this lower salt buffer appear to have a more anisotropic distribution when compared to those in the higher salt buffer.

5.6 Conclusions

To summarize, we measured the interaction potentials for a colloid-polymer mixture consisting of anionic silica particles and polymeric λ -DNA. The resulting potentials are the first simultaneous measurements of the range and depth of the interaction potential between two colloidal particles in a polymer solution of varying concentration, including a regime where the semi-flexible chains are strongly entangled. The range of the measured interaction potentials was found to be related to the radius of gyration of the polymer in the dilute regime and the correlation length in the semi-dilute region. The depth of the potentials was found to increase linearly with concentration in dilute DNA solutions, however a near quadratic dependence was observed after the overlap concentration was exceeded. In both concentration regimes the AO Model was successfully used to fit the interaction potentials. As expected the dilute region can be envisioned as a solution consisting of polymer coils which act as hard spheres of size R_g . Surprisingly the model can be extended into the semi-dilute region, where the polymer solution is described as a gas of uncorrelated hard spheres of a radius of $\approx (2/\pi)R_p$.

The colloidal particles also act as a gentle probe that monitors the polymer behavior in solution. Our observations present strong evidence for transitions from a near ideal dilute solution to a semi-dilute regime which is dominated by pair-wise contacts and is predicted to exist to only for semi-flexible polymers [33, 34]. More-

over our analysis allows us to quantitatively determine the solvent quality. Changes to the solvent quality brought about through changes in the ionic strength showed anomalous behavior at low salt concentrations. The resulting decrease in interaction range might result from an anisotropic distribution of links caused by an increased persistence length.

Our *model-independent* potentials serve as an exemplar for the microscopic investigation of a broad range of questions that commonly arise in colloid-polymer solutions. Most importantly they provide a functional form for the interactions that are inherent in these suspensions. They also highlight the important role that the polymeric phase plays in driving depletion. The comparable size ratio of the colloid and the DNA used in our experiments also ventures into a previously unexplored regime that often arises in nanometer scale solutions.

Chapter 6

Particle Dynamics in DNA solutions

The dynamical properties of colloidal particles in DNA solutions are of wide ranging interest. From electrophoretic migrations through gels to chromatographic separation techniques, understanding the motion of beads in mesh-like polymer solutions is extremely important. Moreover, recent interest in probing the *in vivo* properties of cellular environments has led to the development of numerous techniques to measure the microrheological properties of minuscule volumes of complex fluids [91]. One such technique follows the motion of colloidal probe particles suspended in the medium of interest. The trajectories are monitored by, centrifugation, light scattering and most recently by video microscopy. In all of these experiments the material properties of the medium, such as the viscosity, moduli etc. are then inferred from the motion of the particles. Data interpretation relies on the fact that the diffusion in the complex fluid is described by the Stokes-Einstein relationship, and therefore the spheres probe the background viscosity of the solution. In this chapter we examine

the hydrodynamic interactions between the probe spheres in the background solution of DNA.

Previous studies have examined colloidal dynamics in different polymer backgrounds. Quasi-elastic light scattering has been used to probe the dynamics of latex spheres in a polystyrene polymer solution [92]. Other studies have varied the composition of the colloidal particles, or varied the background dispersant [92, 93, 94, 95, 96]. Pioneering work using sedimentation techniques was done by Langevin and Rondelez [97]. They probed the properties of a polyethylene oxide (PEO) solution with various colloids ranging from latex spheres to globular bovine serum albumin. More recently sedimentation of colloidal particles (CaCO_3 with adsorbed calcium alkylbenzene) through poly-ethylene-propylene (PEP) [98] has been used to test the theoretical scaling predictions of the viscosity[16]. In all of these studies, with perhaps the exception of the last one, the equilibrium interactions between the colloid and the polymer were not well characterized. This can be a critical issue because adsorption and inhomogeneities tend to complicate the interpretation of data resulting in differing viewpoints of colloidal diffusion in polymer solutions.

Our DNA-colloidal system is ideally suited for studying the dynamics of beads in different background concentrations. Having developed an understanding of the characteristic entanglement lengths and colloid-polymer interactions, we can now use this system to study dynamic properties of such mixtures. This chapter explores two

aspects of the bead dynamics in DNA solutions. The first part is dedicated to the problem of a single sphere diffusing in a background polymer solution. We explore the dynamics of different sized particles as a function of polymer concentrations. The second half of the chapter studies the hydrodynamic interactions that arise between the two beads in the presence of a polymer background. As colloidal concentrations are increased the inter particle spacing decreases, and hydrodynamic interactions become important. We study these effects by looking at the mobility of two spheres at close range. The results presented in this chapter represent our preliminary investigations into this system; further work is currently underway.

In this chapter I will first discuss the diffusion of single particles in a background of DNA. We use video microscopy to monitor the motion of the colloidal spheres, and relate the time evolution of their mean square displacements to the diffusion coefficient. We explore the diffusive nature of these colloidal spheres by looking at several different sized particles in background solutions of varying DNA concentrations. We find that the simple Stokes-Einstein equation is insufficient for relating the observed diffusion coefficients to the background viscosity. These measurements show that spheres whose sizes are comparable to the polymer mesh size probe the solvent viscosity. Particles feel the effects of the polymer background only when they are much larger than the characteristic entanglement length. This suggests that the depletion cavity and the hydrodynamic coupling of the bead to the polymer solution

strongly influence the observed dynamics. We also explore bead dynamics in a DNA background for separations wherein the hydrodynamic coupling is important. This is done by confining the motion of the two beads in an optical trap and extracting their relative mobility. Our results clearly show the effects of screened hydrodynamics in polymer solutions.

6.1 Brownian Motion

The role of thermal forces affecting Brownian motion was well studied in the early part of this century. The problem is usually approached from either the Einstein-Smoluchowski equation or through the Langevin formalism [19, 99]. The first approach, examines the concentration gradients created by the thermal variations in the particle velocities and suggests that the diffusive behavior arises due to the net flux between the created inhomogeneities. This is usually modeled by Fick's law which relates the net flux $j(\mathbf{r}, t)$, of the particles to the concentration gradient $c(\mathbf{r})$, through, $j(\mathbf{r}, t) = -D\nabla c(\mathbf{r})$, where D is the diffusion constant. The probability distributions for particle displacements are calculated by demanding that the number of particles be conserved. The Langevin approach, incorporates the thermal fluctuations through a stochastic force. We present a brief description of the latter formalism and see how it is related to our observed particle motions.

6.1.1 Langevin Formalism

Perhaps the simplest approach to describing the motion of a particle in a fluid is to examine the forces acting on it. For simplicity we focus on the physics in one-dimension. The equation of motion for the particle is given by [99]

$$m \frac{d^2 x}{dt^2} = -\zeta \frac{dx}{dt} + f(t) \quad (6.1)$$

where m represents the mass of the particle and x is its position. The forces acting on the particle are characterized by the two terms on the left. The first, $\zeta dx/dt$ represents the viscous drag on the particle the magnitude of which is determined by the friction coefficient, ζ . Most commonly, the strength of the friction coefficient is given by Stoke's Law which ignores inertial effects. This is given by

$$\zeta = 6\pi\eta a \quad (6.2)$$

where η is the viscosity of the fluid and a is the particle radius. The second term in Eq. 6.1, $f(t)$ represents the stochastic forces acting on the particle that arise due to thermal fluctuations. There are several assumptions that are made about these fluctuating forces in attempting to solve the Langevin equation. It is assumed that these forces are independent of the particle velocity and uncorrelated at different times, i.e. $\langle f(t)f(t + \Delta t) \rangle = \delta(\Delta t)$. Under these assumptions, Eq. 6.1 can be multiplied by $x(t)$ and rewritten as

$$\frac{m}{2} \frac{d}{dt} \left[\frac{d(x^2)}{dt} \right] - m \left(\frac{dx}{dt} \right)^2 = -\frac{\zeta d(x^2)}{2dt} + f(t)x \quad (6.3)$$

where we have used the fact that $x d^2x/dt^2 = \frac{1}{2} \frac{d}{dt} \left[\frac{d(x^2)}{dt} \right] - \left(\frac{dx}{dt} \right)^2$ and $x dx/dt = \frac{d(x^2)}{2dt}$.

Now if one considers the ensemble average of all the particles in solution, there are two simplifications that can be made. Since the random force and the particle positions are completely uncorrelated, $\langle x f(t) \rangle = 0$. Secondly we can use the equipartition theorem, $\frac{1}{2} m \langle (dx/dt)^2 \rangle = \frac{1}{2} k_B T$, to replace the second term on the left hand side of Eq. 6.3. The equation can now be written as

$$\frac{m}{2} \frac{du}{dt} + \frac{\zeta}{2} u = k_B T \quad (6.4)$$

where $\langle \frac{d(x^2)}{dt} \rangle$ has been replaced by u . Solutions to this equation are then given by

$$u = 2k_B T / \zeta + \text{const.} e^{-\zeta t / m} \quad (6.5)$$

Since we are interested in solutions where inertial effects are negligible, i.e. $\zeta / m \gg 1$, the second term in Eq. 6.5 can be ignored. Substituting for u and further integrating yields

$$\langle x^2 \rangle - \langle x_0^2 \rangle = \frac{2k_B T}{\zeta} t. \quad (6.6)$$

where x_0 is the initial position of the particle. This can be rewritten using the Stokes-Einstein result, $D = k_B T / \zeta$, as

$$\langle x^2 \rangle - \langle x_0^2 \rangle = \Delta x^2 = 2Dt. \quad (6.7)$$

where D is the diffusion coefficient of the particle.

From the above equation, we see that measurements of the mean square displacement of a particle as a function of time, can be used to extract diffusion coefficients. In addition, the probability distribution $P(x, t)$ for particle displacements, x , in time t has a second moment that is given by Eq. 6.7. Since the nature of this distribution is closely related to the fluctuations of the thermal forces, the probability distribution for Gaussian fluctuators, is given by $\frac{1}{(2\pi\sigma)^{1/2}} e^{-\frac{(x-\langle x(t) \rangle)^2}{2\sigma}}$, where $\langle x(t) \rangle$ is the first moment of the distribution and σ is its second moment. Substituting Eq. 6.6 for σ and the mean particle position x_0 for the first moment, $P(x, t)$ can be written as

$$P(x, t) = \frac{1}{(4\pi Dt)^{1/2}} e^{-\frac{(x-x_0)^2}{4Dt}} \quad (6.8)$$

The Gaussian distribution, directly reflects the random nature of the thermal forces. Deviations from this form often indicate the presence of other forces.

So far all the results have been derived in one dimension. This can be easily generalized to three dimensions since the motion along each dimension can be decoupled. The mean square displacement in 3-D is given by $\langle \Delta \mathbf{r}^2 \rangle = \langle \Delta x^2 \rangle + \langle \Delta y^2 \rangle + \langle \Delta z^2 \rangle = 6Dt$. The total probability distribution is now given by the product of the distributions in each direction, $P_{3D}(\mathbf{r}) = \frac{1}{(4\pi Dt)^{3/2}} e^{-\frac{(\mathbf{r}-\mathbf{r}_0)^2}{4Dt}}$, where \mathbf{r}_0 is the mean position of the particle. For our experimental measurements we consider probability distributions in only the x direction. This is because the interlacing (see Chapter 4) in the y direction presents complications in image analysis that might affect the measured distributions. We use Eq. 6.8 to describe the measured probability distri-

butions for particle displacements. The next section describes these experiments in detail.

6.2 Single Particle Tracking Measurements

In a homogeneous viscous medium, the diffusion coefficient of a particle is related to the viscosity of the background fluid through the Stokes equation. Monitoring the motion (and therefore the diffusion coefficient) of the particles enables us to calculate the viscosity of the solution. In a polymer solution the analysis can be complicated by the inhomogeneities in the medium. These may arise due to interactions between the bead and the polymer or due to entanglements that are present in concentrated polymer solutions.

Let us examine the causes of these inhomogeneities in further detail. The introduction of a bead into a polymer solution can lead to modifications in the local environment due to polymer interactions. For example if these interactions are attractive the polymer will adsorb on the surface of the particle, altering the effective hydrodynamic radius and consequently its dynamics. Moreover in an entangled polymer solution the ratio of the characteristic mesh size to the size of the bead plays an important role in affecting polymer dynamics. For an infinitely small sphere the dynamics might be expected to be governed by the viscosity of the solvent alone [16]. On the other hand if the bead size is much larger than the entanglement length

scale (e.g. the shearing plates of a rheometer) the bead dynamics will probe the bulk viscosity of the polymer solution. The intermediate regime in which the bead size approaches the mesh size is more complex, and is of interest to us. For particles in non-adsorbing DNA we can change both polymer entanglement lengths as well as the particle size to explore this regime.

6.2.1 Particle Tracking Techniques

We measure the dynamical properties of colloidal spheres suspended in DNA solutions by monitoring the time evolution of their positions. As in our previous experiments we use video microscopy to follow particle trajectories in order to determine single particle diffusion coefficients. However since we are interested in the free diffusion coefficient of isolated particles, we do not need, nor is it desirable, to confine the spheres in an optical trap. We simultaneously track the locations of multiple particles suspended far apart from each other. Using this multi-particle tracking approach, instead of following a single particle, enables us to obtain better statistics while minimizing the duration of our observations.

To monitor the motion of multiple particles over a long period of time, we need to maintain a sufficient density of particles in the field of view. Since the particles are no longer confined to the focal plane (as was the case in the line tweezer) they eventually settle at the bottom of the sample cell due to gravity. Such sedimentation effects can

be avoided by matching the density of the background fluid to that of the sphere. This is most easily done for our system by using polystyrene beads suspended in a Tris:buffer modified with heavy water. We used a solution of Tris in a 1:1 mixture of D₂O and water (see Chapter 4) and verified the lack of sedimentation by looking at our sample under the microscope. These samples were found to have a fairly constant particle density ($\approx 20 - 100$ particles in a field when viewed through a 63X objective) over long periods of time, suggesting that the polystyrene spheres neither sink to the bottom nor float to the top of the cell.

Additionally, precautions were taken to ensure the homogeneity of the solution. The beads were sonicated or vortexed for 30 seconds to break up aggregates. This was particularly important for the fluorescently tagged particles, since their surface chemistry makes them more susceptible to aggregation. The DNA solution was homogenized by stirring slowly (to prevent breakage) with a pipettor tip. When the two solutions were mixed together the concentration of spheres in DNA was adjusted so that a typical field of view contained only 20-100 particles in focus (vol. frac. $\sim 10^{-4}$). The number varied depending on the size of the particle. In each field of view the distance between particles was typically greater than ~ 10 particle radii which prevented hydrodynamic interactions between the spheres.

These samples were viewed with an inverted microscope (Leica, DMIRB) using a water immersion lens (63X, 1.2 NA). The use of water instead of oil as an immersion

fluid enables us to focus deeper into an aqueous sample. Our multi-particle tracking measurements were carried out at the center of the microchamber, $\sim 60\mu\text{m}$ from the coverslip wall to minimize hydrodynamic coupling between the beads and the chamber walls.

We use fluorescently tagged anionic polystyrene spheres (Molecular Probes Inc.) as tracer spheres in our experiment. Using fluorescence microscopy instead of bright field aided in image processing since particle images did not have dark rings which tends to lead to mis-identification of particles. The field aperture is adjusted to give us a large depth of field. A CCD camera, similar to the one used in the previous set of experiments (see Chapter 4) was used to record the images at video rates. We also confirmed our observations, by using the faster imaging capabilities of the confocal head on the Leica (Noran Oz). Images recorded at 120Hz yielded results similar to those recorded at video rates. We typically digitize the entire video frame, (a sample image is shown in Fig. 6.1) since we need to track all the particles in the field of view. Sufficient statistics can be obtained by digitizing and analyzing ~ 4000 frames which requires a gigabyte of storage space.

Image processing techniques used to locate the centers of each bead are similar to those used in the equilibrium interaction measurements (Chapter 4). Locating the centers of the spheres when particles are well separated is easier than in the case of the two sphere measurements, since particles rarely come within a radii of each other

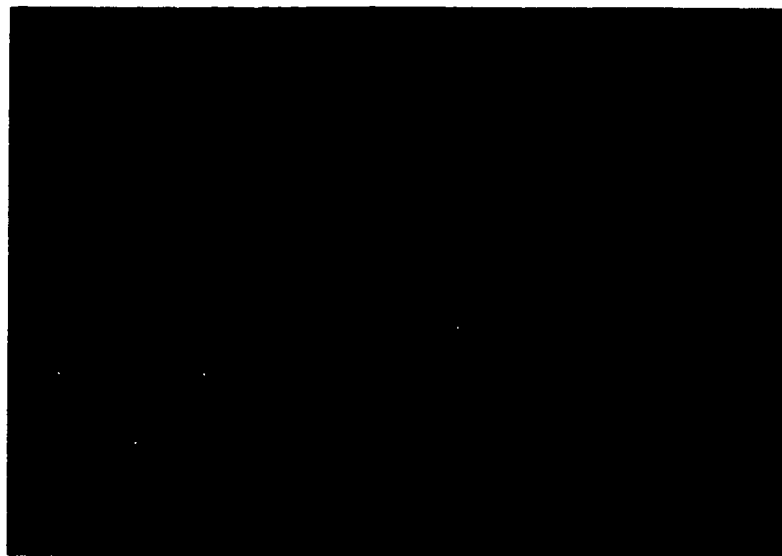


Figure 6.1: A fluorescence image of one micron PS particles in DNA solution. The bright spots represent the particles.

and we no longer need to correct for overlap of images. Once again we used IDL as our image analysis platform to remove long wavelength features and calculate particle locations using the algorithm described in Chapter 4, Section 4.5. The processing is automated after the parameters used to locate particles is visually optimized. An image with the centroid locations is shown in Fig. 6.2.

In the process of calculating the positions of the spheres, we also calculate moments of the brightness distribution of each particle. These distributions help us distinguish particles of interest from noise, aggregates, and other unwanted features since monodisperse spheres tend to form clusters with a well defined signature. An example of this clustering effect is shown in Fig. 6.3 where the first moment of the brightness distribution, i.e. the intensity, and the second moment, the radius of gy-

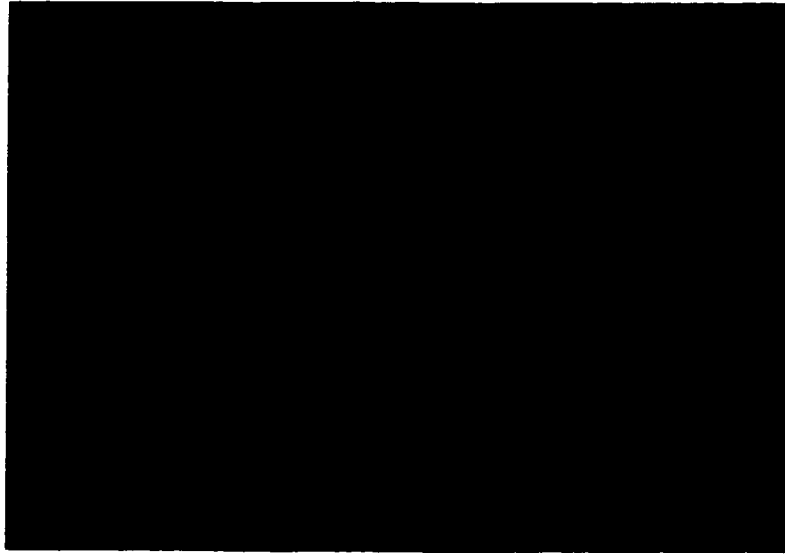


Figure 6.2: We use the feature location algorithm to locate the centers of the particles (see Appendix C). The locations found by using appropriate parameters are overlaid on the original image and are shown as black dots on the above micrograph.

ration, is plotted against each other. We see that distribution has a wide range of intensities with the brightest features being identified with the particles lying in the focal plane. Since particles can wander in and out of focus in either of the two vertical directions, each of which has its own distinct spherical aberration characteristics, the distribution splits into two arms. Feature identifications associated with noise usually appear at low intensities and are randomly distributed whereas aggregates, can usually be distinguished by their larger radii of gyration. Thus we see that the clustering of monodisperse spherical particles makes them easily distinguishable from background noise and allows us to eliminate spurious particles.

Once we have successfully located the particles of interest we need to follow the time evolution of their positions to determine their dynamics. To follow the trajec-

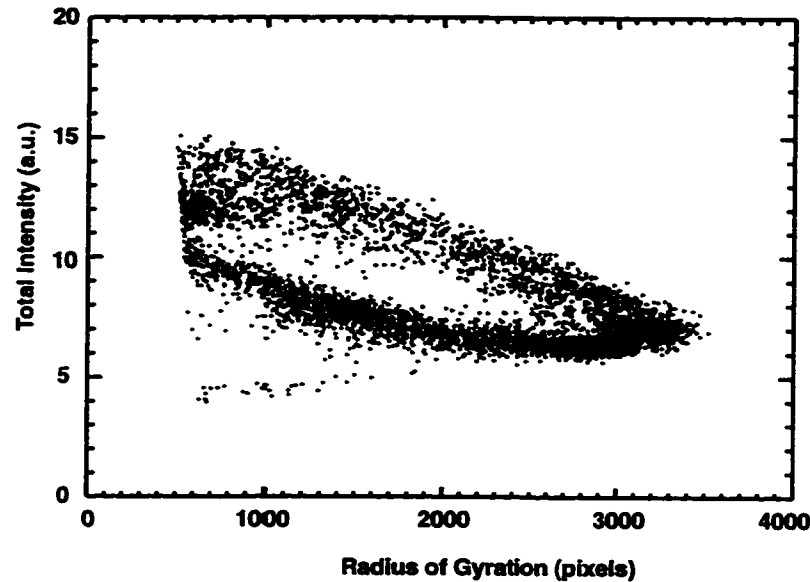


Figure 6.3: The mean intensity of the brightness distribution is plotted against the radius of gyration of the same distribution. The vertical axis is in pixels and the horizontal axis is in arbitrary units. The two arms of the distribution arise due to anisotropy in the spherical aberration in the two vertical directions.

tory of the particles in time the features in each frame need to be identified with corresponding particle locations in the next frame. This is done using a real-time tracking program which requires user input on several physical parameters to limit computational complexity. For instance, a user specified distance restricts the range in which possible features are identified. This length scale corresponds to the physical distance a particle is expected to diffuse between video frames. To avoid multiple labeling this distance must be smaller than the mean particle spacing. The tracking program also allows for particles to leave the field of view and reappear. Once again the user determines the length scale for which the particle identity is retained. If a particle appears within the specified distance and time step then the trajectory is

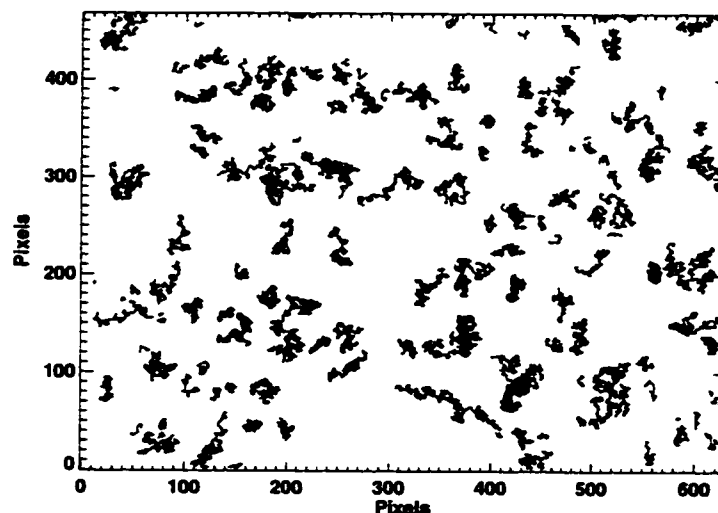


Figure 6.4: The trajectories of particles are followed by a real time tracking program. The above graph shows the tracks that were identified for a 1 micron sphere in buffer over 960 frames for a total of 30 seconds.

continued. On the other hand if particles appear at locations that did not originally contain a feature, they are added to the data set. Additional cuts for noise reduction can be specified by eliminating trajectories that exist for only a few frames, since noise features are most likely to appear and disappear between frames. Particle trajectories for a $1.1\mu\text{m}$ sphere in water are shown in Fig. 6.4.

Once we have successfully tracked the particles, we look at the probability distributions for the displacements in different time steps, and use the variance of this distribution to calculate the mean square displacements. Since our images are two dimensional we can only calculate the mean-square displacements for the x and the y directions. However we can still extract a diffusion coefficient for the particle since the diffusion in each direction is independent of the other two directions, i.e

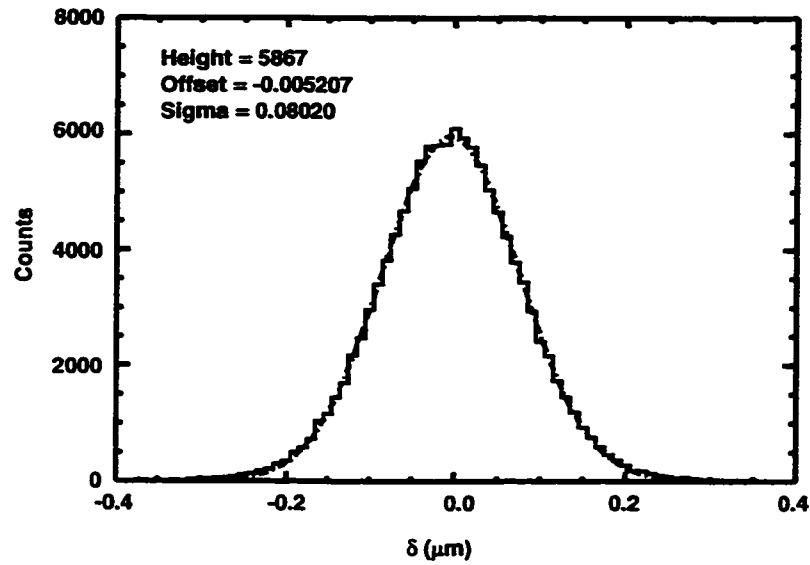


Figure 6.5: The probability distribution for the measured displacements after one time step. We see that the mean lies very close to zero, which implies that there are no long time drifts. The overlaid fit (shown by dashed lines) is a Gaussian whose variance is related to the diffusion coefficient through $\sigma = 2D$.

$\langle x^2 \rangle = \langle y^2 \rangle = \langle z^2 \rangle = 2Dt$. We fit the measured distributions to a Gaussian which helps eliminate spurious contributions that have survived our previous cuts. For example features that are highly diffusive increase contributions to the tails of the distribution, and features that are not moving at all contribute to the peak height. This process does not eliminate any physics as most distributions are very close to Gaussian. Fig. 6.5 shows a typical histogram with an overlaid Gaussian fit, and the subsequent figure, Fig. 6.6, shows the time dependence of the mean square displacements. A straight line fit to the latter curve yields diffusion coefficients.

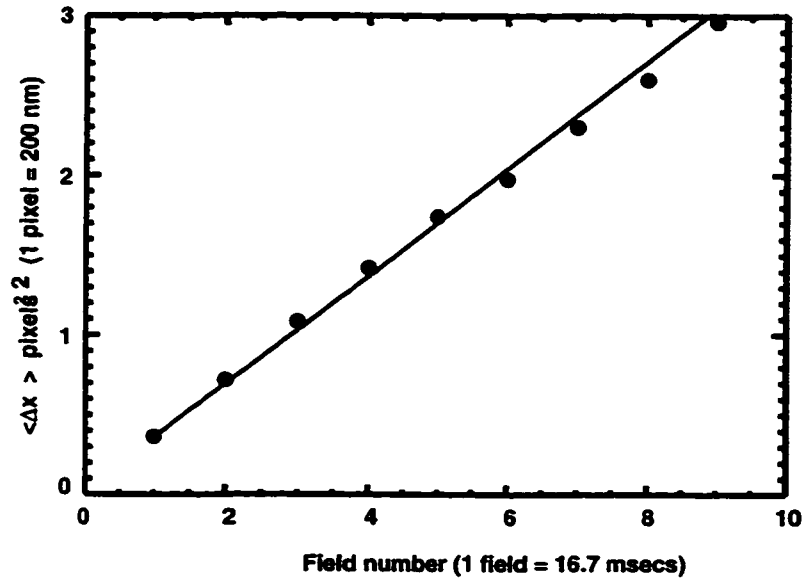


Figure 6.6: Mean square displacement curves shown for a 1 micron bead in a buffer solution. The slope of the straight line fit measures the diffusion coefficient.

6.3 Results

We are interested in exploring the changes in the diffusion coefficient as we vary the ratio of the size of the probe particle, to the characteristic entanglement length. For our purposes we can achieve this effect in two different ways. By changing the background DNA concentration we can effectively change the correlation length which in turn determines the mean spacing between entanglements. We can determine the exact size of the entanglement length from our equilibrium measurements in DNA solutions where we found that the correlation length scales with concentration as $c^{-1/2}$. Alternatively, we can keep the DNA concentration fixed and vary the size of the probe sphere. We explore both these approaches using multi-particle tracking

techniques.

6.3.1 Fixed Colloid Size

With a fixed colloid size, $a = 1.1\mu\text{m}$, we vary the DNA concentration from 0 to $300\mu\text{g/ml}$. The measured mean square displacements are shown in Fig. 6.8. As expected we see a decrease in the slope of the curves as the DNA concentration is increased. Since the solution gets visibly more viscous it is not surprising that the particles move slower. On examining the mean square displacements carefully, we also observe that $\langle \Delta x^2 \rangle$ does not scale linearly with time as the concentration is increased. This sub-diffusive behavior is shown more clearly in Fig. 6.9 which shows the mean square displacements for a two micron bead in concentrated DNA, where the effect is more pronounced. We find for concentrations lower than $100\mu\text{g/ml}$, the measured particle motion is diffusive in the entire time domain explored (16.7msecs -2 mins). However, as the concentration is increased beyond $100\mu\text{g/ml}$ the exponents at short time scales (≤ 1 sec), fall below unity.

To understand the origin of these effects we look briefly at the dynamics of polymers in solution. The myriad conformations available to a polymer gives rise to several different time scales that determine its motion. One such time scale is defined as the reptation time. This concept was developed by DeGennes [16] and exploits the idea that polymer motion is restricted by tube like constraints formed by surrounding

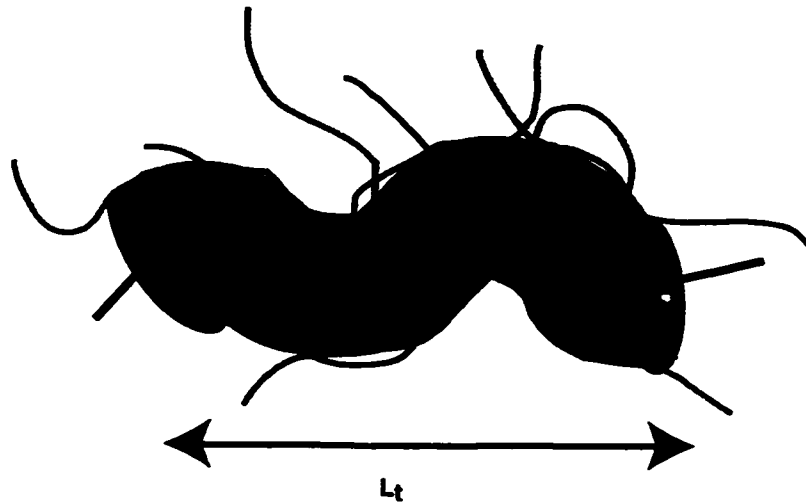


Figure 6.7: A polymer chain entrapped in a tube formed by the surrounding entangled polymer solution. The length of the tube is given by L_t and the time taken to diffuse the length of the tube is called the reptation time.

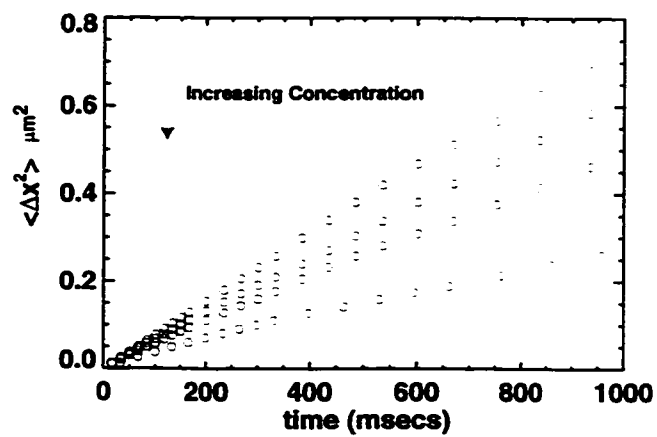


Figure 6.8: The measured mean square displacements for a $1\mu\text{m}$ sphere at different DNA concentrations ($10\mu\text{g/ml}$, $50\mu\text{g/ml}$, $100\mu\text{g/ml}$ and $300\mu\text{g/ml}$).

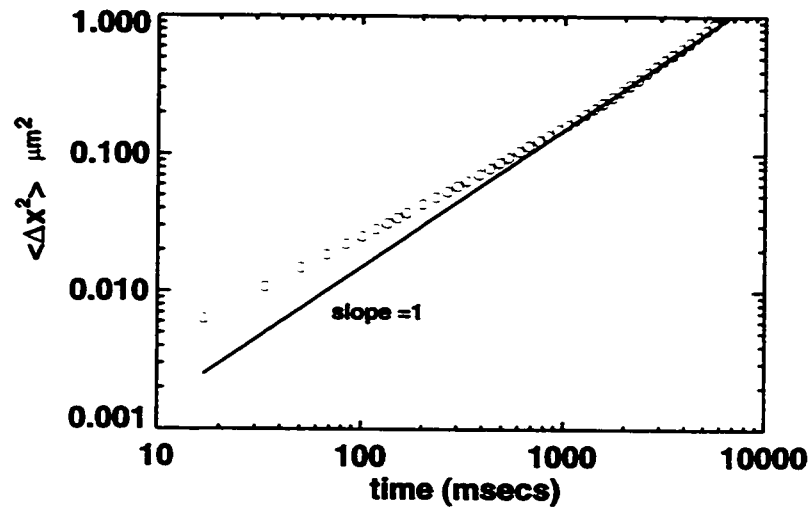


Figure 6.9: The measured mean square displacement for a $2\mu\text{m}$ bead in concentrated DNA solution ($300\mu\text{g/ml}$).

polymers (see Fig. 6.7). The time taken by a polymer to diffuse through this ‘tube’ is termed a reptation time, τ^* , and scales with the length of the tube, $L_t \sim Nl^2/\xi$ and the transverse diffusion time, $D_t \sim k_B T \xi / (\eta_{\text{Solvent}} N l^2)$, as $\tau^* \sim L_t^2 / D_t$. Since both L_t (which scales as $\sim c^{1/2}$) and D_t (which scales as $\sim c$) change with the number of entanglements, the reptation time for semi-flexible polymers scales as $\tau^* \sim c^{3/2}$. Polymer motion is found to be diffusive at time scales that are longer than τ^* but at shorter times, re-arrangement dynamics of links and link connectivity give rise to sub-diffusive behavior. Since the reptation time increases with concentration, in the highly concentrated DNA solutions, τ^* lies within our measured time window. This is suggested by the motion of the beads; we see a sub-diffusive regime at short times which gives way to the diffusive regions at longer times (see Fig. 6.9). The time scales (30msecs - 1s) compare well with other measurements of the tube renewal times for

λ -DNA [86, 100], further supporting this argument.

To extract diffusion coefficients, we focus our attention on the long time regimes, where $\langle \Delta x(t)^2 \rangle \sim t$. The results of straight line fits to these regions is shown in Fig. 6.10. We normalize the measured values by our mean square displacement measurements of the particles in pure solvent in order to eliminate systematic errors that might arise due to variations in particle size, temperature etc.. If we assume a Stokesian relationship between the measured diffusion coefficient and the viscosity, i.e. $D = k_B T / (6\pi\eta a)$, our measurements show an increase in viscosity with an increase in concentration.

The concentration dependence of viscosities in polymer solutions are hard to model theoretically. An empirical model that has been used to describe the bulk viscosity of the polymer solution is the Huggins equation [101]. Here the viscosity increase with concentration is given by

$$\eta/\eta_0 = 1 + [\eta]c + k_H[\eta]^2c^2 + \dots \quad (6.9)$$

where η_0 is the viscosity of the solvent, $[\eta]$ is the intrinsic viscosity of the DNA solution and k_H is the Huggins parameter. Equation 6.9 is similar to the hard sphere viscosity, where $\eta/\eta_0 = 1 + 2.5\phi$ [16], where ϕ is the polymer volume fraction. The differences arise due to the deformability of the polymer coil which is accounted for by the intrinsic viscosity, $[\eta] \propto R_g^3$. The Huggins parameter in Eq. 6.9 accounts for polymer-polymer interactions. For λ -DNA, viscometric techniques have measured

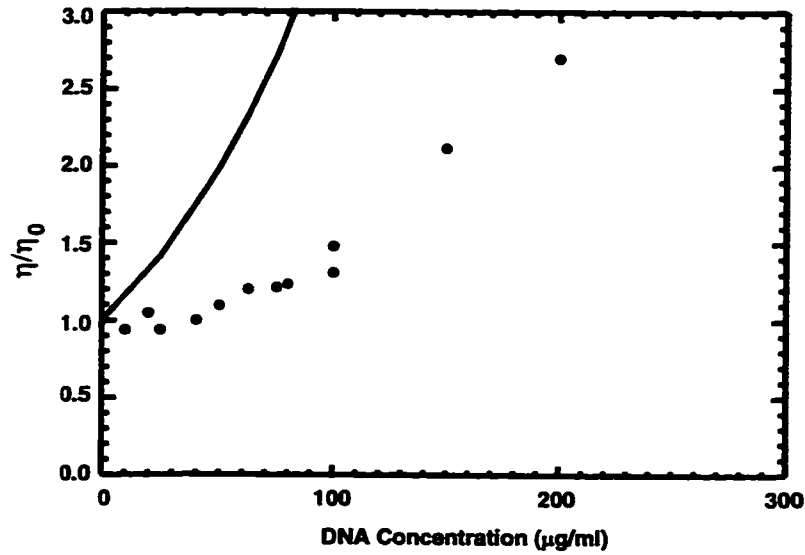


Figure 6.10: The increase in normalized viscosities with concentration is shown as filled plot symbols. The solid line shows the values that would result if the Huggins model with the previously measured parameters is used.

$[\eta] = 1.32 \times 10^{-2} \text{ ml}/\mu\text{g}$ [20] and k_H is theoretically calculated to be around 0.75 [101].

The data is not well described by Eq. 6.9 using the parameters above. The measured viscosity increase is much slower than what would have been expected (see Fig. 6.10).

To understand these discrepancies let us examine the Stokes-Einstein relationship in detail. The diffusion coefficient of a freely diffusing particle, is given by $D = k_B T / 6\pi\eta a$, where a is the effective radius of the particle. For example, a can either be the hard sphere radius of the particle or the hydrodynamic radius as is the case for a polymer coil. In a simple solvent the ratio of the diffusion constant of a hard sphere, D , to its diffusion constant in water, D_0 (at the same temperature), is equal to the inverse of the viscosities, i.e. $D/D_0 = \eta_0/\eta$. However in a complex fluid the hard sphere radius of the particle might be altered due to interactions with the

background fluid. For example, adsorption of polymers from the background fluid could lead to a higher effective radius which could change as the background polymer concentration is altered. In such scenarios a generalized equation for the ratio of the diffusion coefficients can be written as

$$\frac{D}{D_0} = \frac{a\eta_S}{\eta_P(c)R_{\text{eff}}(a, \xi, \Delta\eta)} \quad (6.10)$$

where $\eta_P(c)$ is the concentration dependent polymer viscosity and $R_{\text{eff}}(a, \xi, \Delta\eta)$ represents the effective hydrodynamic size of the bead. The functional form of R_{eff} is not only controlled by the hard sphere size but may also depend on the correlation length (which is concentration dependent) of the polymer solution and the surrounding viscosity. In a simple viscous fluid, R_{eff} should reduce to the hard sphere radius, a . However if interactions between the polymer and the bead were present this assumption would breakdown; then our experiment would probe the complex ratio $\eta_S/\eta(c)_P R_{\text{eff}}(a, \xi, \Delta\eta)$. The discrepancies between Stokes-Einstein predictions and our measured values suggest that the local environment around the bead is modified. The lower viscosity values could arise due to reduced polymer concentrations around the bead. We explore these issues further in the next section.

6.3.2 Fixed DNA Concentration

We repeat the above experiments, but this time we keep the concentration of the background fixed, and look at the diffusion constant as we change the size of the probe

DNA Concentration	0.3 μm	0.6 μm	1.1 μm	2.0 μm
No DNA	1.66 \pm 0.05	0.8 \pm 0.05	0.47 \pm 0.05	0.25 \pm 0.02
30 $\mu\text{g/ml}$	1.5 \pm 0.2	0.6 \pm 0.1	0.38 \pm 0.05	0.20 \pm 0.05
100 $\mu\text{g/ml}$	1.47 \pm 0.03	0.49 \pm 0.02	0.28 \pm 0.1	0.15 \pm 0.1
300 $\mu\text{g/ml}$	0.92 \pm 0.02	0.35 \pm 0.05	0.15 \pm 0.1	0.08 \pm 0.02

Table 6.1: Measured diffusion coefficients of different sized beads at different background concentrations.

beads. We use four different sized colloidal spheres (0.3 μm , 0.6 μm , 1.1 μm and 2.0 μm) to measure diffusion coefficients in different DNA concentrations of 30 $\mu\text{g/ml}$, 100 $\mu\text{g/ml}$ and 300 $\mu\text{g/ml}$. Once again we observe a decrease in the ratio, D_0/D with increasing bead size (see Table 6.1). This is inconsistent with the fact that the background concentration is fixed, and our colloidal spheres are measuring a bulk viscosity. Our data indicate that the smallest spheres measure viscosities that are close to the solvent viscosity. As the sphere size increases, the effective viscosity starts to deviate strongly from the buffer measurements.

These results clearly show that the probe sphere is not measuring the bulk viscosity, and its size is playing a significant role in the value obtained. To understand the effects of the probe size, we plot the normalized diffusion coefficients, D_0/D , against the critical ratio a/ξ . In order to do so we need to know both the correlation length as well as the size of the bead. The correlation lengths used are obtained from the fits

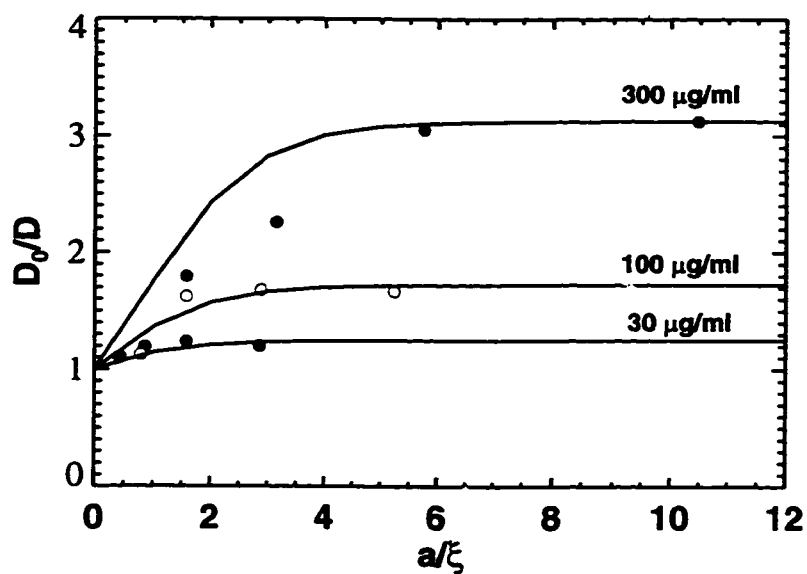


Figure 6.11: The change in the relative viscosity plotted against the critical ratio a/ξ as the bead size is changed. The solid spheres represent measurements made at a fixed DNA concentration of $300\mu\text{g/ml}$, the open circles present measurements made at $100\mu\text{g/ml}$ and the grey circles are data taken at $30\mu\text{g/ml}$. The predictions of the theory (see text) are shown as solid lines.

to the interaction energies presented in the previous chapter. The second parameter that we need to know accurately is the size of the bead. From static light scattering experiments (this was carried out in the D₂O Tris Buffer on the goniometer in the Weitz lab) we measure particle sizes of all the beads used. As we see in Fig. 6.11 at ratios for which the bead size is comparable to the correlation length, the diffusion coefficient of the probe bead is close to solvent values. As the critical ratio a/ξ increases the measured diffusion coefficient plateaus at different values for the three different DNA concentrations. To understand this behavior we explore the factors that could control the diffusion of beads in complex fluids.

A theoretical model for the scaling of the friction coefficient for beads in a polymer solution has been suggested by DeGennes and his co-workers [16, 97] to be

$$D/D_0 \sim \left(1 - \frac{\eta_0}{\eta_{bulk}}\right)e^{-a/(\xi)} + \frac{\eta_{bulk}}{\eta_0} \quad (6.11)$$

where η_0 is solvent viscosity and a/ξ is the critical ratio. The concentration dependence of the correlation length determines the nature of the stretched exponential. When the size of the probe bead exceeds the size of the mesh size the measured viscosity approaches the bulk value, η_{bulk} . On the other hand when $a \ll \xi$, then the measured viscosity approaches the solvent viscosity. Equation. 6.11 qualitatively reproduces our results (see Fig. 6.11), however the decrease of the function at low, a/ξ ratios is not reproduced. The measured ratios appear to decay faster, indicating that the properties of the surrounding medium are closer to that of the solvent.

We re-examine our data by considering Eq.6.10 carefully. By keeping the background DNA concentration fixed in our experiments we directly probe the effective hydrodynamic radius, $R_{\text{eff}}(a, \xi, \Delta\eta)$ since $\eta_P(c)$ is a constant for all sphere sizes. We see that the effective hydrodynamic radius steadily increases from its solvent value to a maximum, $R_{\text{eff}}^{\text{MAX}}(a, \xi, \Delta\eta)$. This maximum value increases with polymer concentration, suggesting that the plateau level is related to the bulk viscosity. In addition R_{eff} levels off at different values of a/ξ for different polymer concentrations indicating that the contrast between the bulk polymer viscosity and the solvent viscosity plays an important role.

To understand this behavior we look more closely at the interactions between the beads and the polymer solution. From the two-bead interaction measurements we know that each bead is surrounded by a depletion cavity whose size is given by $\sim \pi\xi/2$. This region is depleted of polymer coils, making the immediate environment around a bead more ‘solvent like’, which would support the lower viscosities measured. In addition the size of this region is controlled by the background DNA concentration. Thus at a fixed DNA concentration the depletion cavity around each bead has the same size. Evidence for this effect was found by looking at interaction potentials with different sized spheres (see Section.5.5 in Chapter 5). To understand the motion of the beads in the depletion cavity we need to examine the hydrodynamic interactions between the sphere and the surrounding polymer medium which does depend on the

size of the bead.

The velocity field created by a moving sphere in a Newtonian fluid decays as a/r [102]. When the particles are enclosed in cavities, the flow field is disrupted due to the presence of the exterior medium which can create complicated back flows. In our experiment the flow generated by the motion of the particle propagates through the depletion cavity till it interacts with the background polymer solution. Since the magnitude of the flow field is determined by the size of the bead, larger beads have velocity fields that are longer range than those of the smaller spheres. Interactions between this velocity field and the neighboring polymer solution could lead to modifications in the motion of the particle. This effect would be more pronounced for the larger beads since the disturbances are more likely to penetrate the polymer solution (see Fig. 6.12). In addition the boundary conditions presented by the depletion cavity are non-trivial. Higher bulk polymer concentrations are more likely to present larger perturbations to the flow field. This would then make the motion of the bead strongly dependent on the viscosity mismatch between the depleted region and the bulk. These issues suggest that the role of the depletion cavity plays a significant role in determining the hydrodynamic coupling between the bead and the polymer solution.

Particle-tracking experiments allow us to explore different regimes of diffusion in colloid-polymer solutions. We directly measure the diffusion coefficient of a bead and

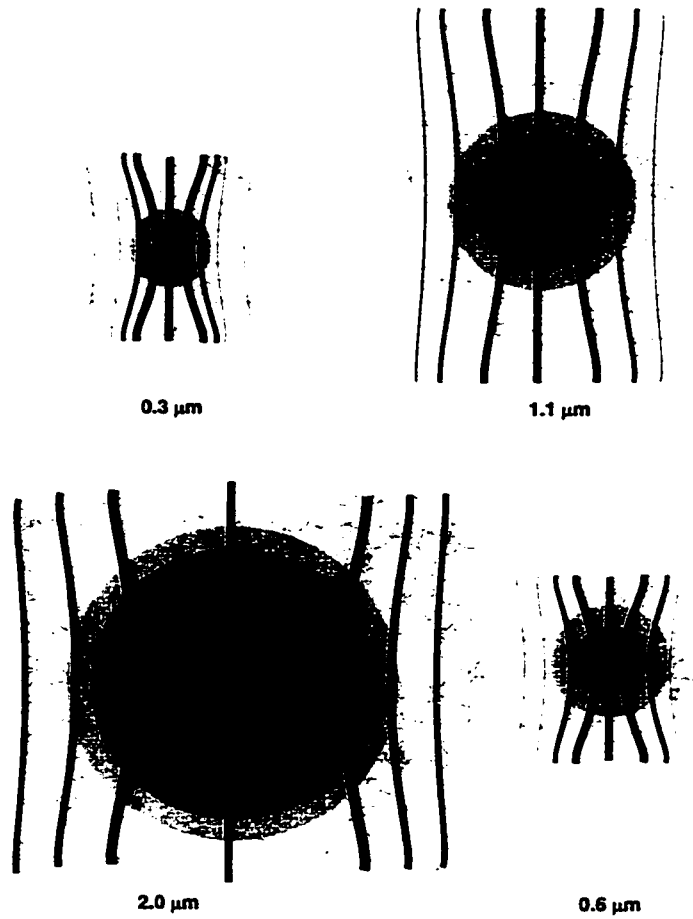


Figure 6.12: A cartoon showing the velocity fields created by a moving sphere which depend on the size of the sphere. The light gray region surrounding each sphere represents the depletion region that surrounds each bead. The velocity fields are shown as dark lines, the width of which represents the strength.

see how it changes with polymer concentration. The measured viscosities are found to deviate strongly from the expected bulk polymer viscosities. Further investigations in which we keep the background viscosity fixed, allow us to directly measure the functional form of the effective radius that controls the bead motion. We find that the function deviates strongly from the measured hydrodynamic radius and is dependent on the ratio of the bead size to the correlation length. From these measurements it is possible to identify regions which are insensitive to bead size and could offer information about the surrounding medium. We suggest a qualitative model that could account for the observed behavior based on hydrodynamic interactions between the beads and the polymer solution outside the depletion cavity. Further theoretical investigations are needed to confirm these predictions.

6.4 Coupled Diffusion in Polymer Solutions

So far our discussions have been limited to a single sphere suspended in a fluid. However the dynamics of the system changes in crowded colloidal systems due to interparticle hydrodynamic effects. Technologically important processes like sedimentation and aggregation are largely determined by the hydrodynamic interactions between the colloidal spheres. These interactions are mediated by disturbances in the fluid due to motion of the particles. For example a point sphere moving through a fluid generates a velocity field which in turn causes motion of the surrounding spheres.

In this section we explore the simple case of hydrodynamic interactions between two spheres in polymer solutions.

In order to understand the hydrodynamic interactions it is necessary to understand the flow field generated by a moving sphere [35, 102]. The starting point for most hydrodynamic calculations is the Navier-Stokes equation. The viscous drag force, \mathbf{F} , felt by an isolated sphere moving at constant velocity \mathbf{V}_0 , in an incompressible fluid is found from the relation

$$\mathbf{V}_0 = -\mathbf{M} \cdot \mathbf{F} \quad (6.12)$$

where \mathbf{M} is the mobility coefficient. For a single isolated rigid sphere of size a , $\mathbf{M} = \hat{\mathbf{I}}/(6\pi\eta a)$ where η represents the viscosity of the solution and $\hat{\mathbf{I}}$ is the identity matrix. The velocity field generated by this moving sphere can be calculated in a two step process. A simple calculation for a point particle moving at constant velocity, \mathbf{V}_0 , yields a flow field, $\mathbf{u}(\mathbf{r})$ that is given as

$$\mathbf{u}(\mathbf{r}) = \mathbf{T}(\mathbf{r}) \cdot \mathbf{F} = 6\pi\eta\mathbf{T}(\mathbf{r}) \cdot \mathbf{V}_0. \quad (6.13)$$

Here $\mathbf{T}(\mathbf{r})$ is the Oseen tensor that describes the velocity field at a displacement \mathbf{r} from the source of the disturbance. For a point source in a simple solvent the velocity field only depends on one vector, \mathbf{r} and the Oseen tensor has the form, $\mathbf{T}(\mathbf{r}) = (1/(8\pi\eta r))(\hat{\mathbf{I}} + \hat{\mathbf{r}}\hat{\mathbf{r}})$. The calculation can be extended to a finite sphere of size

a , by Taylor expanding the velocity field around the center of the sphere [35] to yield

$$\mathbf{u}(\mathbf{r}) = 6\pi\eta a \mathbf{V}_0 \cdot \left(1 + \frac{1}{6}a^2 \nabla^2\right) \mathbf{T}(\mathbf{r}) \quad (6.14)$$

Substituting the form of the Oseen tensor and taking the appropriate derivatives yields a velocity field that is given by

$$\mathbf{u}(\mathbf{r}) = \frac{3a}{4r} \left(1 + \frac{a^2}{3r^2}\right) \mathbf{V}_0 \hat{\mathbf{I}} + \frac{3a}{4r} \left(1 - \frac{a^2}{r^2}\right) \hat{\mathbf{r}} \cdot \mathbf{V}_0 \hat{\mathbf{r}}. \quad (6.15)$$

We see that at close range, $r \sim a$ the fluid moves at the same velocity \mathbf{V}_0 as the particle, and far away, i.e. $r \gg a$ it goes to zero. However the effect is still long range as the leading order term falls off as $1/r$.

In crowded colloidal suspensions the long range flow field created by one moving sphere affects the motion of the other spheres. For the simple case in which there are only two spheres, the velocity field generated by the first sphere causes the second sphere to move. The particle velocity of an identical second sphere, $\mathbf{V}_2(\mathbf{r})$ can be calculated by Faxen's law to be

$$\mathbf{V}_2(\mathbf{r}) = \mathbf{u}(\mathbf{r}) + \frac{a^2}{6} \nabla^2 \mathbf{u}(\mathbf{r}) \quad (6.16)$$

where $\mathbf{u}(\mathbf{r})$ is the velocity field generated by the first sphere and is given by Eq. 6.15. This motion in turn affects the motion of the first sphere and higher order effects can be calculated iteratively.

The presence of the second particle breaks the spherical symmetry of the system and the mobility matrix in Stoke's Law (Eq. 6.2) is no longer diagonal. For the two

Diagonal Elements	$M_{11} = M_{22} = 1/(6\pi\eta a)\hat{\mathbf{I}}$
Off-Diagonal Elements	$M_{12} = M_{21} = 1/(6\pi\eta a)(\frac{3a}{4r}\hat{\mathbf{I}} + \frac{3a}{4r}\hat{\mathbf{r}}\hat{\mathbf{r}}) + \vartheta(\frac{a^3}{r^3})$

Table 6.2: Mobility Matrix for Two Spheres in a Solvent

sphere system the viscous drag on each particle, i is now given by a matrix equation

$$\mathbf{V}_i = - \sum_j \mathbf{M}_{ij} \mathbf{F}_j \quad (6.17)$$

where the four mobility coefficients, \mathbf{M}_{ij} quantify the hydrodynamic interactions. Solutions for the two sphere system in a solvent background have been explicitly calculated by Batchelor [103] and the $1/r$ dependence of the relative diffusion coefficient has also been experimentally observed [104]. Both theoretical predictions as well as experimental observations reveal that the relative mobilities of the two particles are suppressed and the center of mass motion is enhanced. The origins of these effects lie in the fact that it is harder to squeeze out the liquid between the two spheres than it is for the fluid entrained by one sphere to pull along the second sphere. A summary of the results for the different mobility coefficients in a pure solvent can be found in Table. 6.2.

Having revisited the tools needed to understand hydrodynamic interactions between two spheres in a solvent we turn to the problem in which the background is replaced by a polymer solution. Unlike a pure solvent where the hydrodynamic interaction is long range ($\sim 1/r$) in a polymer solution this effect is predicted to be screened

by the polymers. A qualitative understanding for this can be obtained by comparing the viscosities of a solvent with that of a semi-dilute polymer solution which generally tends to be higher. Since the velocity field generated by a point displacement is proportional to $1/\eta r$, a larger viscosity causes the field to die off faster. The typical length scale associated with the decay is called the hydrodynamic screening length, ξ_H and is proportional to the static correlation length [105] discussed in Chapter 2. Quantitatively these differences have been explored in a mean field treatment of the Navier-Stokes equation in which the background polymer solution is modeled as an effective medium [106, 107, 108]. The contributions to the flow field due to the finite size of the polymer coils and the changes that occur due to instantaneous rearrangements of these coils are ignored. Instead, the background polymer is treated as an effective medium and their average effect is included in the calculation. We explore the hydrodynamic interactions between two spheres in a polymer solution.

6.5 Two-Sphere Measurements

Our multi-particle tracking experiments demonstrated that the region surrounding the probe sphere strongly dominates the dynamics. In this section we use a second bead and look at the hydrodynamic interactions between the two beads to get a better understanding of this region. In order to measure the hydrodynamic interaction. Once again we utilize the optical line tweezer to spatially confine the particles, so that we

may study their displacements at close range.

6.5.1 Diffusion in an Optical Trap

Measuring diffusion constants in an optical potential raises a range of issues. In order to dispense with some of these problems, we closely examine the diffusion of a single sphere in the trap and compare it with multi-particle tracking results. Since the particle is bound in an optical potential the motion of the bead is no longer freely diffusing. We can calculate the probability distribution by using the Langevin approach. With the addition of a parabolic potential Eq. 6.1 gets modified to

$$m \frac{d^2 x}{dt^2} = -\zeta \frac{dx}{dt} + f(t) - kx \quad (6.18)$$

where k is the spring constant associated with the optical potential. If we ignore inertial effects, i.e. $\frac{d^2 x}{dt^2} \rightarrow 0$, the probability distribution for particle displacements, $P(x, t)$, that results from the equation of motion is given by [19]

$$P(x, t) = \left[\frac{2\pi k_B T}{k} (1 - e^{-2t/\tau}) \right]^{-1/2} \exp \left[-\frac{k(x - x_0 e^{-t/\tau})^2}{2k_B T (1 - e^{-2t/\tau})} \right] \quad (6.19)$$

where, $\tau = \zeta/k$ and x_0 is the mean position of the particle. In the small time limit, i.e. $t \ll \tau$, Eq. 6.19 reduces to a Gaussian distribution indicating that the particle does not 'feel' the parabolic optical potential. We have used a single sphere to map out the shape of the typical optical potential. From these measured potentials (see Fig.5.3, we find that $k \sim 0.5k_B T/\mu\text{m}^2$, the friction coefficient $\zeta = 6\pi\eta_0 a = (0.45\mu\text{m}^2/\text{s})/k_B T$,

and thus $\tau = 200ms$. For all the diffusion constants reported in this section, the measured times ranged from 16.7ms to 70ms.

Additionally we found the trapping to be optimal at a short distance from the coverslip wall. This will lead to hydrodynamic coupling between the bead and the chamber wall that will affect the measured diffusion constant. The correction to the single particle long time diffusion coefficient due to the presence of the wall is given by [104]

$$D = D_0 \left[1 - \frac{9a}{16x_1} - \frac{9a}{16x_2} \right] \quad (6.20)$$

where x_1 and x_2 are the distances from both the enclosing walls. For our measurements the distances are $x_1 \sim 100\mu\text{m}$ and $x_2 = 3\mu\text{m}$. We measure the diffusion coefficient of a single sphere by trapping it in our line trap and following its motion. These measurements are made at two different depths, $3\mu\text{m}$ and $7\mu\text{m}$ and the diffusion coefficients are measured to be $0.35\mu\text{m}^2/s$ and $0.37\mu\text{m}^2/s$ respectively. Using the appropriate correction factor for both the wall distances we find that the values for D_0 that we extract are $0.389 \pm 0.01\mu\text{m}/s^2$ and $0.394 \pm 0.01\mu\text{m}/s^2$. These compare well, within error bars, and are close to the theoretically calculated values indicating that we can extract unperturbed diffusion coefficients from the optical trap.

When considering the effect of the wall on the motion of two spheres, we need to consider the relative motion and the center of mass motion separately. When the two spheres are moving in the same direction, i.e. the motion of the center of mass,

they create flow fields that are similar to that of a single sphere and thus we would expect their diffusivities to be affected similarly. When the two spheres are moving against each other, i.e. relative motion, then their flow fields partially cancel each other out thus reducing the coupling to the wall [104]. In addition, we also need to consider the effects of the wall in the presence of polymers. The coupling with the wall is expected to be long range, $1/r$, in the pure buffer solution. With the addition of polymer to the solution the flow fields are exponentially screened and one would expect the coupling to the wall to be reduced. Thus with increasing polymer solution the effects of the wall on the particle motion should be negligible.

6.5.2 Experimental Results

Having considered the limitations of the optical trap on one particle motion we now look at the the diffusive motion of two particles at close range. The introduction of a second bead introduces additional forces into the problem. In the limit in which optical forces can be ignored, the complete Langevin equation (again ignoring inertial effects) in center of mass coordinates can be written as

$$\zeta \frac{dr}{dt} = f(t) - \frac{\partial U_{depletion}}{\partial r} \quad (6.21)$$

where $\frac{\partial U_{depletion}}{\partial r}$ is the depletion force. The effects of the depletion well can be highlighted by looking at Fig. 6.14. This figure displays a naive plot in which the diffusion coefficients have been extracted using similar means as was employed for single bead

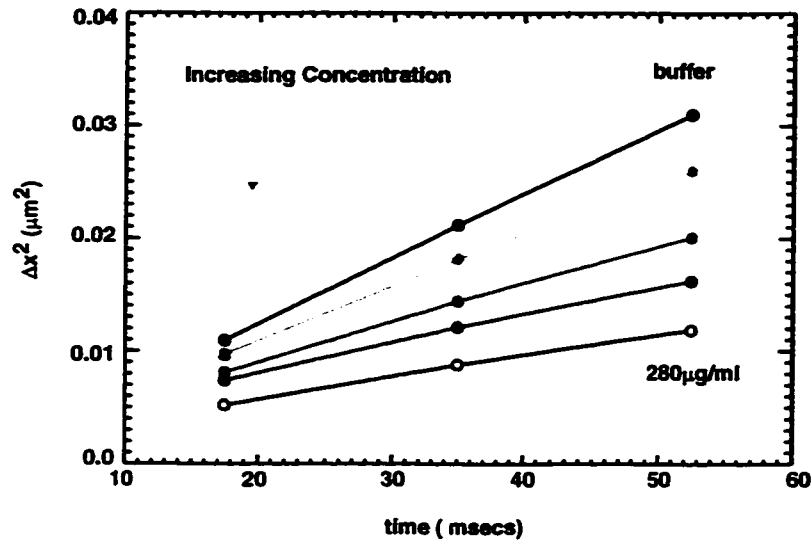


Figure 6.13: The mean square displacements for the relative coordinate at different DNA concentrations.

measurements. Two particles are trapped in the line tweezer and their motion is followed for 30 minutes. Once again the centroid locations are calculated. The data is partitioned according to the initial separation of the two particles, and the time evolution of the mean square displacement within each segment was used to calculate diffusion coefficients (see Fig. 6.13). This technique is marred by two problems. First, the data at small separations is not diffusive since the particle motion is partially constrained by the depletion well. In addition the short-time behavior of the most concentrated solutions appear sub-diffusive due to polymer entanglement effects much like the effects observed in multi-particle tracking. In spite of these limitations the data provides qualitative information on the effects of the depletion cavity. At small separations the relative particle motion barely changes and this is reflected

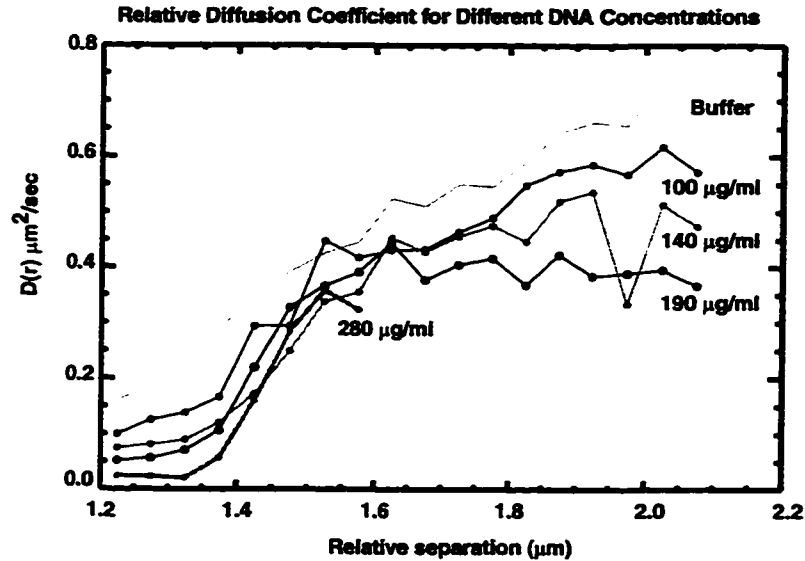


Figure 6.14: The relative diffusion coefficients at different bead separations for different concentrations of DNA.

in the low value of the *effective* diffusion coefficient. At separations beyond which depletion effects are no longer felt, the measured values demonstrate the differences that arise due to the presence of polymers. If we examine the extracted diffusion coefficients (see Fig. 6.14), at long range, i.e. at separations greater than $1.8\mu\text{m}$, we see that the buffer diffusion coefficient values continue to increase whereas the values in the polymeric solutions level out, suggesting that the motion of the particles is greatly altered in DNA solutions.

We now return to Eq. 6.21 and re-analyze our data to remove these artifacts and extract mobility coefficients. In order to calculate the mobility of the particles we need to know the force exerted by the depletion interaction as well as the relative velocity of the particles. Both pieces of information are readily available from our data.

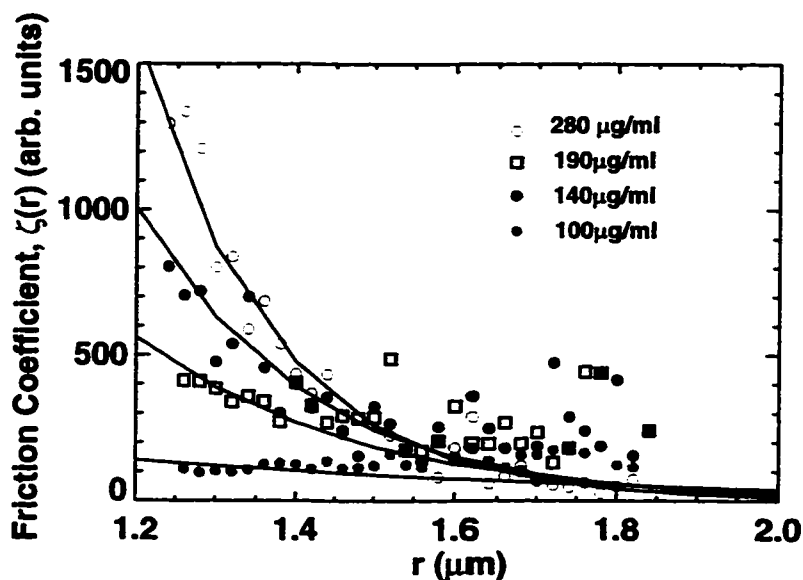


Figure 6.15: The friction coefficient $\zeta(r) = (-\partial U_{depletion}/\partial r) / \langle v(r) \rangle$ measured at different DNA concentrations.

The depletion forces are obtained from the measurement of the interaction energies presented in the last chapter. The average relative velocities can be calculated from the time dependent positions of the particles. Using these results as well as the fact that fluctuating thermal forces average to zero, the mobility coefficient ($= 1/\text{friction coefficient}$) in Eq.6.29 can be written as

$$M(r) = 1/\zeta(r) = v(r)/(-\partial U_{depletion}/\partial r) \quad (6.22)$$

The measured results are shown in Fig. 6.15. Once again the data was segmented according to initial particle separations and the average velocities were computed within each segment. Fits to the raw potentials measured by the means described in Chapter 5 are used to calculate the force, $\partial U(r)/\partial r$. We see that the friction coefficients

are increased at close separations and decrease as the relative separation between the spheres increase. This effect is enhanced at higher polymer concentrations. This is similar to the observations in pure solvents, however the mobility coefficients appear to have a characteristic decay length in the polymer solutions.

We attempt to fit the data with a screened mobility coefficient. In an pure solvent we expect that the mobility coefficient would fall off as $1/r$, however in a polymer solution we might expect the range to be decreased due to screening effects. we might expect the mobility coefficient to have a slightly modified form (from the solvent result) and be given by

$$M(r) = 1/\zeta(r) = 1 - \frac{C}{r} e^{-\frac{(a-r)}{\xi_H}}. \quad (6.23)$$

where a is the diameter of the bead, ξ_H is the characteristic decay length, and C is a multiplicative constant. A fit to the above equation with two free parameters. the hydrodynamic correlation length, ξ_H and the multiplicative constant, is shown as solid black lines in Fig. 6.15. The fit parameters obtained for ξ_H compare well with the correlation length of the background DNA solution. We find that $\xi = (1.5 \pm 0.4)\xi_H$. These measurements demonstrate that the screening concepts proposed for hydrodynamic interactions in polymeric solutions plays an important role in mobility coefficients for two beads.

6.6 Conclusions

We have successfully probed the dynamical properties of colloidal spheres in DNA solutions. Our experiments with a single sphere in a background of DNA, reveal the subtleties of particle diffusion in complex fluids. We find that the particle size plays an important role in determining the viscosities measured. We directly measure the functional form of the effective hydrodynamic radius, that describes the motion of different sized beads. Our results suggest that smaller beads are less affected by the surrounding polymer network than larger beads. This qualitatively agrees with theoretical predictions, but further theoretical work is needed to account for the subtleties of the diffusive behavior. We also look at close range bead dynamics to study the effects of hydrodynamic screening. The measured mobilities are found to follow the predicted exponential decays expected within a mean field theory.

The complexities of colloidal dynamics in polymer solutions are distinctly highlighted in our measurements. We have used a system in which we carefully characterized the physical properties, to study the dynamics. We find that with the detailed knowledge of the entanglement lengths and interactions we are able to extract the dynamical behavior and suggest qualitative models to describe the behavior. There is no doubt that further investigations are needed to completely understand the complex dynamics. Most importantly these experiments open up possibilities for future investigations, both theoretically as well as experimentally.

Chapter 7

Conclusions and Future Work

In this thesis we have shown how colloidal spheres can be used as gentle probes of complex fluids. In particular we have explored the energetics, structure and the dynamics of a model polymer, DNA, using the Brownian motion of the colloidal spheres. The observed microscopic interactions ultimately affect the structural and dynamical properties of bulk polymer solutions. The techniques developed in this thesis can be extended to explore both microscopic phenomena of fundamental interest, as well as study interactions arising in real world systems.

Specifically, by confining two spheres on a line optical tweezer and following their motion with digital video microscopy we directly probed the interaction between two colloidal beads in a polymeric DNA solution. We have presented the first simultaneous measurements of the range and the depth of the polymer depletion potential. Moreover we were able to measure the functional form of this interaction in both the dilute regime (that has been theoretically modeled already) and the semi-dilute

polymer solution which is less well understood. Our measurements show that appropriately scaled hard sphere depletion models can still be applied to the entangled semi-dilute polymer solutions. Thus the notion of describing the entangled polymer regime as a close packed system of 'blobs' clearly manifests itself in the depletion world!

In addition to testing depletion predictions, our experiments also provide a clean test of the calculated state diagram for polymer solutions. Calculations show that the introduction of a persistence length into the description of the polymer leads to new phases in the polymer state diagram. These effects are manifest more strongly in cases such as DNA, where the persistence length is large compared to the polymer chain diameter. Our observations provide the first measurements of the transition from the dilute regime to the weakly fluctuating semi-dilute regime where the physics is dominated by pair-wise contacts between links. Thus this technique provides an effective way of probing the fluctuation spectrum that exists in different polymer solutions.

Besides exploring fundamental issues, these experiments also measure polymer properties that are of relevance to the practical user. Our measurements were carried out in a regime where the size of the polymer and the colloid were comparable. Issues arising when the ratio of the sizes of the two suspension components (i.e the particle and the polymer) is close to unity are of technological interest; in this regime aggre-

gation in suspensions is minimized. We are also able to quantitatively characterize the second virial coefficient which determines polymer solution properties, such as solvent quality and size. Our apparatus measures polymer osmotic pressures with sub-Pascal resolution, which exceeds the sensitivity of traditional osmometers.

The dynamical issues explored in this thesis highlight the effects of microscopic interactions on rheological properties. Thus simple analyses using Stokes-Einstein predictions do not predict the rheological properties of the background material. Our measurements highlight the importance of hydrodynamic coupling of the beads to the background material. These issues need to be explored in detail to develop models that would adequately account for such hydrodynamic interactions. We also examined the hydrodynamic coupling between two particles in the presence of a polymer background. The effects of hydrodynamic screening can be clearly seen in the measured mobility coefficients.

These experiments represent a foray into the polymer-colloid world and opens up a variety of opportunities for future investigation. The use of bio-materials to explore fundamental concepts in polymer physics, offers a vast resource for the physicist. The tools and materials developed in biochemistry and microbiology can be used to manipulate polymers which can be used to study fundamental physics and at the same time develop a better understanding of cellular environments. For example, the numerous restriction enzymes, polymerases, etc. that can be found for different DNA

sequences allow for easy manipulation of the polymer.

Our experiments using salt demonstrate that simple changes in chemical environments lead to large changes in polymer structure. This allows us to explore depletion in systems where the polymer is more rod-like in addition to being able to access the intermediate regimes. For example reducing the length of the DNA in low salt solutions could allow us to reach the rod like limit and understand the subtleties of this regime. Moreover DNA in living organisms usually exists as plasmids, which are then digested to produce linear double strands. With the help of enzymes it should be possible to ligate the ends of the DNA to reproduce a plasmid. This is an interesting area in polymer physics since topological constraints give rise to new and interesting energetic effects in entropic systems. This area has been poorly explored since synthetic ring polymers are hard to manufacture. Depletion studies in such systems could elucidate polymer properties, and we are ideally poised to do so with these techniques.

The breadth of possibilities for exploration of fundamental physics with DNA does not stop there. Biochemists have successfully attached biotin to one end of DNA. Biotin forms one component of a lock and key molecule, the other part of which (Streptavidin) can be easily coated onto colloidal particles. With this mechanism it is possible to covalently bind DNA to a colloidal particle to form a polymer brush layer with a long length scale. Studying interactions between polymer brushes

on curved surfaces would allow us to mimic and understand conditions that help stabilize colloidal particles. In addition polymers on curved surfaces have interesting conformational properties. For instance close to the bead surface monomer density is high but decreases further out. Thus correlation lengths at close range would be different than those further from the surface. Using the line tweezer set-up it should be possible to probe these different polymer configurations and measure oscillations in the interactions that arise due to varying 'blob' size.

Apart from probing fundamental problems our technique can also be extended to understand real world problems. Polydisperse polymer solutions, branched polymer solutions etc., can all be investigated with this technique. For example herring sperm DNA is an interesting polydisperse system that can be investigate to study issues in depletion due to polydisperse polymers. On the other hand we can use the optical trap as a point tweezer to study kinetics of biologically important molecules. Binding chemistry can be used to attach complementary proteins (such as the selectins that are important in white blood cell adsorption) on two different surfaces, i.e. the coverslip wall and the colloidal bead. The optical trap can be used to position the probe sphere at different distances and monitoring the motion of the bead in different chemical environments should allow us to calculate kinetic rates for reactions. Moreover to determine the the effects of polymer entanglements on these rates, the smaller molecules of interest can be attached to DNA and/or suspended in glycerol to reduce

the time scales to lie within our measurement capabilities.

We see that the present experiments have only introduced what can be measured with this technique. There are exciting possibilities, especially when the systems under investigation that can be used to bridge the biochemical and physics world.

Appendix A

The Second Virial Coefficient

The virial expansion is often used to describe simple physical systems. This series usually corrects for the effects of interactions in a system that is otherwise described as non-interacting. The starting point for these calculations can be found in several texts [29]. We revisit the calculation of the second virial coefficient which is used for the polymer systems described in this thesis.

The Hamiltonian for a system of independent particles which interact with each other through an interaction potential u_{ij} , such as the one shown in Fig.2.3 (Chapter 2), can be written as

$$H = \sum_{i=1}^{i=N} p_i^2/2m + \sum_{i<j} u_{ij} \quad (i, j = 1, 2, \dots, N) \quad (\text{A.1})$$

where p_i is the momentum of each particle. The corresponding partition function in a given volume, V and at temperature, T , is given as

$$Q_N(V, T) = \frac{1}{N!} \int d^{3N} p d^{3N} x e^{-H/k_B T} = \frac{1}{N!} \left(\frac{2\pi m k_B T}{h} \right)^{3N/2} Z_N \quad (\text{A.2})$$

where

$$Z_N = \int \prod_{i < j} (1 + f_{ij}) d^3 x_1 \dots d^3 x_N. \quad (\text{A.3})$$

Here we have defined $f_{ij} \equiv e^{-k_B T / u_{ij}} - 1$ which is usually referred to as the Mayer function. We see that as the interaction energy vanishes the partition function Q_N reduces to the simple free particle result. To include the effects of interactions we can expand Z_N in a series

$$Z_N = \int (1 + \sum f_{ij} + \sum f_{ij} f_{kl} + \dots) d^3 x_1 \dots d^3 x_N. \quad (\text{A.4})$$

The different terms, $f_{ij} f_{kl}$, $f_{ij} f_{kl} f_{mn}$ etc. represent the clusters in an N-particle system that provides corrections to the non-interacting result. The second virial coefficient, B , is described as the two-point interaction and is given by the term f_{12} . This can be written out explicitly as

$$B = \frac{h^{3/2}}{2(2\pi m k_B T)^{3/2} V} \int f_{12} d^3 x_1 d^3 x_2. \quad (\text{A.5})$$

If we use the fact that the interaction depends only on the separation between particles, $r = x_1 - x_2$ then the above equation can be rewritten as

$$\begin{aligned} B &= \frac{2\pi h^{3/2}}{(2\pi m k_B T)^{3/2}} \int f(r) r^2 dr \\ &= \frac{2\pi h^{3/2}}{(2\pi m k_B T)^{3/2}} \int (e^{-u_r / k_B T} - 1) r^2 dr \end{aligned} \quad (\text{A.6})$$

The above result can be used for deriving polymer interactions, (as is done in Chapter 2, Section 2.2), with $u(r)$ representing the link interaction potential.

Appendix B

Free Energy Minimization

In this appendix we discuss the minimization of the free energy of a polymer system in the random phase approximation [17, 16]. We also discuss the minimization considerations when two point particles are inserted in a polymer solution.

From Chapter 2 we saw that the free energy can be written as

$$F = F(c) + \frac{Tl^2}{24c} \int d^3r \frac{(\delta c(r))^2}{\xi^2} + (\nabla \delta c(r))^2 \quad (\text{B.1})$$

where $F(c)$ was the homogeneous free energy of the system and the last two terms result from the expansion around this minimum state. In the above equation, l represents the link size, and $\delta c(r)$ represents the deviations in the concentration from the mean bulk concentration, c . The simplest solution in which the free energy is minimized is when $\delta c(r) = 0$. However, to calculate the correlation between concentration fluctuations we must look at the higher order terms in the expansion of the free energy. We must find the minimum under the additional condition in which a link is held fixed at $r = 0$. To find the new minimum state we look at the last two

terms in Eq. B.1 and look for solutions that will minimize the contribution. This is given by

$$\frac{Tl^2}{24c} \int d^3r \frac{(\delta c(r))^2}{\xi^2} + (\nabla \delta c(r))^2 = 0 \quad (\text{B.2})$$

Integrating the last term by parts and using the constraint that the link is fixed at $x = 0$ results in

$$\int d^3r (\nabla \delta c(r))^2 = (\delta c(r)) \nabla \delta c(r) \Big|_{x=0}^{x=\infty} - \int d^3r \delta c(r) (\nabla^2 \delta c(r)) \quad (\text{B.3})$$

When evaluated at the two limits the first term on the right hand-side is zero, which lets us rewrite the sum of the two terms under the integral in Eq. B.2 as

$$\nabla^2 \delta c - (1/\xi^2) \delta c = 0. \quad (\text{B.4})$$

The solution to this equation is often referred to as the Ornstein-Zernicke formula.

The introduction of two point particles in the polymer solution alters the free energy of the system. The free energy associated with each particle is given by Eq. 2.40 and has to be added to Eq. B.1. In addition the insertion of the particles leads to perturbations in concentration that also contribute to the free energy. This was given in Eq. 3.6. Thus the total free energy can be written as

$$\begin{aligned} F = 2F(c) + \frac{2Tl^2}{24c} \int d^3r \frac{(\delta c(r))^2}{\xi^2} + \delta c(r) (\nabla^2 \delta c(r)) \\ + \int \delta c(r) u(r - r_1) d^3r + \int \delta c(r) u(r - r_2) d^3r \end{aligned} \quad (\text{B.5})$$

Once again the sum of the last four terms has to vanish in order to minimize the free energy.

$$\int d^3r \left[\frac{(\delta c(r))^2}{\xi^2} - (\delta c(r) \nabla^2 \delta(c(r)) + \frac{12c}{k_B T l^2} \delta c(r) u(r - r_1) + \delta c(r) u(r - r_2)) \right] = 0 \quad (\text{B.6})$$

We can cancel $\delta c(r)$ through-out the equation and rewrite it as

$$\nabla^2 \delta c - \frac{\delta c}{\xi^2} = \frac{12c}{k_B T l^2} [u(x - r_1) + u(x - r_2)] \quad (\text{B.7})$$

The above equation is similar to the Ornstein-Zernicke equation except for the fact that the two point particles act as source terms.

Appendix C

List of IDL Routines

The digitized images were analyzed using routines written in IDL. A typical session used to analyze a set of images which contain, two beads is presented below.

A typical batchfile for an image taken in bright-field with a 100X lens and 1.6 tube lens is given by

```
cd,"~verma/data/filled3/buff20"  
  
b = flatten('flat6911','dark7027')  
  
e_xys,'buff*',extent=15,nballs=2,back = b,/replace  
  
e_dbase,'buff*','../data\_buff20',nballs=2
```

This batchfile produces a data file that contains the x and y co-ordinates of each particle, the radius of gyration, the total integrated brightness, and the time code associated with each position. The potential is then calculated by using the command,

```
pot=eqr('data_buff20',binsize=0.02)
```

or

```
pot=n_eqr('data_*',binsize=0.02)
```

The first command takes a data file and calculates a potential from the coordinates. The second command takes all the files in a directory that are labelled, 'data....', and produces potentials that have been binned similarly. This is essential for subtraction techniques. The command `n_eqr` produces multiple files (the number depends on the nos. of files in the directory) which are labelled. For example if there are 3 files then the value of the potential in the third file can be accessed by `pot(1, *, 2)`. Usually the second command was run on a buffer data set and a DNA data set. The output was read into separate two dimensional arrays, which I will call 'buff' and 'dna'. To subtract the buffer value from the dna measurements we used the routine,

```
result=sbt(buff,1.25,dna,0,0)
```

or

```
result=sbt2(buff,1.25,dna,0,0)
```

This routine takes the buffer potential, 'buff', a hard-sphere radius, a sample potential, 'dna', and offsets. The first routine fits a third order polynomial to the buffer potential, whereas the second routine uses a quadratic. The fits are subtracted from the sample potential and the routine returns the subtracted result. The result is a two dimensional array that contains the separation between the spheres and the magnitude of the potential.

The output of the subtraction routine can be fed into a fitting routine that can either fit to the AO model, the mean-field model or the correlation hole picture. These are accessed by

```
fit=aofit(result,startvalue,stopvalue,range,pressure,hard sphere  
radius,vert. offst)
```

The inputs are the array containing the potential, the range of to be fit which is specified by startvalue and stopvalue, initial guesses for the range and the pressure, and a number for the hard sphere diameter and the potential offset.

Bibliography

- [1] J. E. Mark, *Physical Properties of Polymers Handbook* (AIP Press, Woodbury, New York, 1996).
- [2] H. Staudinger, *Über Polymerisation.*, Ber. Dtsch. Chem. Ges. **53**, 1073 (1920).
- [3] A. J. Milling, *Depletion and Structuring of Sodium Poly(styrenesulfonate) at the Silica-Water Interface*, J. Phys. Chem. **100**, 8986 (1996).
- [4] A. Milling and S. Biggs, *Direct Measurement of the Depletion Force Using an Atomic Force Microscope*, J. Colloid Interface Sci. **170**, 604 (1995).
- [5] A. J. Milling and B. Vincent, *Depletion Forces between Silica Surfaces in Solutions of poly(acrylic acid)*, J. Chem. Soc. Faraday Trans. **93**, 3179 (1997).
- [6] M. Ruths, H. Yoshizawa, L. J. Fetters, and J. N. Isrealachvili, *Depletion Attraction versus Steric Repulsion in a System of Weakly Adsorbing Polymer - Effects of Concentration and Adsorption Conditions*, Macromolecules **29**, 7193 (1996).

- [7] F. N. P. Kélicheff and P. Richetti, *Measurement of Depletion Interaction in Semi-dilute Solutions of Worm-like Surfactant Aggregates*, J. Phys. II France **4**, 735 (1994).
- [8] D. Rudhardt, C. Bechinger, , and P. Leiderer, *Direct Measurement of Depletion Potentials in Mixtures of Colloids and Nonionic Polymers*, Phys. Rev. Lett. **81**, 1330 (1998).
- [9] Y. N. Ohshima, H. Sakagami, A. Tokoyoda, T. Igarashi, K. B. Shintaku. S. Toride, H. Sekino, K. Kabuto, and I. Nishio, *Direct Measurement of Infinitesimal Depletion Force in a Colloid-Polymer Mixture by Laser Radiation Pressure*, Phys. Rev. Lett. **78**, 3963 (1997).
- [10] R. Verma, J. C. Crocker, T. C. Lubensky, and A. G. Yodh, *Entropic Colloidal Interactions in Concentrated DNA Solutions*, Phys. Rev. Lett **81**, 4004 (1998).
- [11] A. F. Santos, N. Murthy, P. S. Stayton, O. W. Press, D. Tirrell, and A. S. Hoffman, *Design of Polymers to Increase the Efficiency of Endosomal Release of Drugs*, J. Invest. Med. **46**, 91A (1998).
- [12] C. Bustamante, *Mechanical Manipulation of Single DNA molecules*, Biophysical Journal **70**, MAMS2 (1996).
- [13] Z. Dogic and S. Fraden, *Smectic Phase in a Colloidal Suspension of Semiflexible Virus Particles*, Phys. Rev. Lett **78**, 2417 (1997).

- [14] P. J. Flory, *Statistical Mechanics of Chain Molecules* (Interscience, New York, 1969).
- [15] P. J. Flory, *Principles of Polymer Chemistry* (Cornell University Press, Ithaca, 1979).
- [16] P.-G. de Gennes, *Scaling Concepts in Polymer Physics* (Cornell University Press, Ithaca, 1996).
- [17] A. Y. Grosberg and A. R. Khokhlov, *Statistical Physics of Macromolecules* (AIP Press, New York, 1994).
- [18] W. Burchard and K. Huber, *Theory of Macromolecular Rings* (John Wiley, New York, 1996).
- [19] M. Doi and S. F. Edwards, *The Theory of Polymer Dynamics* (Clarendon Press, Oxford, 1995).
- [20] J. R. Dawson and J. A. Harpst, *Light Scattering and Hydrodynamic Properties of Linear and Circular Bacteriophage Lambda DNA*, *Biopolymers* **10**, 2499 (1971).
- [21] A. V. Arutyunyan, M. A. Ivanova, D. I. Kurlyand, and V. A. Noskin, *Study of Conformational and Dynamic changes in Phage Lambda DNA by Dynamic Light Scattering.*, *Molecular Biology* **27**, 705 (1993).

- [22] H. T. Goinga and R. Pecora, *Dynamics of Low-Molecular Weight DNA Fragments in Dilute and Semi-dilute Solutions*, *Macromolecules* **24**, 6128 (1991).
- [23] J. P. Cotton, B. Farnoux, and G. Jannink, *Neutron Diffraction in Dilute and Semidilute Polymer Solutions*, *J. Chem. Phys.* **57**, 290 (1972).
- [24] M. Daoud, J. P. Cotton, B. Farnoux, G. Jannink, G. Sarma, H. Benoit, R. Duplessi, C. Picot, , and P. G. de Gennes, *Solutions of Flexible Polymers. Neutron Experiments and Interpretation*, *Macromolecules* **8**, 804 (1975).
- [25] X. Ye, T. Narayanan, P. Tong, and J. S. Huang, *Neutron Scattering Study of Depletion Interactions in a Colloid-Polymer Mixture*, *Phys. Rev. Lett.* **76**, 4640 (1996).
- [26] J. L. Xia, P. L. Dubin, S. Edwards, and H. Havel, *Dilute-Solution Properties of Poly(dimethyldiallylammonium chloride) in Aqueous Sodium-Chloride Solutions*, *J. Poly. Sci., Poly. Phys. Ed.* **33**, 1117 (1995).
- [27] D. S. McKenzie, *Polymers and Scaling*, *Phys. Rep* **27C**, 35 (1976).
- [28] J. C. L. Guillou and J. Zinn-Justin, *Critical Exponents for the n-Vector Model in Three Dimensions from Field Theory*, *Phys. Rev. Lett.* **39**, 95 (1977).
- [29] R. K. Pathria, *Statistical Mechanics* (Elsevier, Tarrytown, New York, 1972).

- [30] S. F. Edwards, *The Theory of Polymer Solutions at Intermediate Concentrations*, Proc. Phys. Soc. 265 (1966).
- [31] S. F. Edwards, *Molecular Fluids* (Gordon and Breach, New York, 1976).
- [32] J. des Cloiseaux, *The Lagrangian Theory of Polymer Solutions at Intermediate Concentrations*, J. Phys. **36**, 281 (1975).
- [33] D. W. Schaefer, J. F. Joanny, and P. Pincus, *Dynamics of Semi-Flexible Polymers in Solution*, Macromolecules **13**, 1280 (1990).
- [34] T. M. Birshtein, *Diagram of State for a Solution of Semi-rigid Macromolecules*, Poly. Sci., USSR **24**, 2416 (1982).
- [35] W. B. Russel, D. A. Saville, and W. R. Schowalter, *Colloidal Dispersions* (Cambridge, New York, 1989).
- [36] P. D. Kaplan, J. L. Rourke, A. G. Yodh, and D. J. Pine, *Entropically Driven Phase Separation in Binary Colloidal Mixtures*, Phys. Rev. Lett. **72**, 582 (1994).
- [37] A. P. Gast, C. K. Hall, and W. B. Russel, *Polymer Induced Phase Separations in Non-aqueous Colloidal Suspensions*, J. Colloid Interface Sci. **96**, 251 (1983).
- [38] S. Asakura and F. Oosawa, *Interaction between Particles Suspended in Solutions of Macromolecules*, J. Poly. Sci. **33**, 183 (1958).

- [39] S. Asakura and F. Oosawa, *On Interaction Between Two Bodies Immersed in a Solution of Macromolecules*, J. Chem. Phys. **22**, 1255 (1954).
- [40] J. F. Joanny, L. Liebler, and P. G. DeGennes, *Effects of Polymer Solutions on Colloid Stability*, J. Polymer Sci. **17**, 1073 (1979).
- [41] H. N. W. Lekkerkerker, W. C.-K. Poon, P. N. Pusey, A. Stroobants, and P. B. Warren, *Phase Behaviour of Colloid-Polymer Mixtures*, Europhys. Lett. **20**, 559 (1992).
- [42] W. C. K. Poon, J. S. Selfe, M. B. Robertson, S. M. Ilett, A. D. Pirie, and P. N. Pusey, *An Experimental Study of a Model Colloid-Polymer Mixture*, J. Phys. II **3**, 1075 (1993).
- [43] S. M. Ilett, A. Orrock, W. C. K. Poon, and P. N. Pusey, *Phase Behavior of a Model Colloid-Polymer Mixture*, Phys. Rev. E **51**, 1344 (1995).
- [44] A. Vrij, *Polymers at Interfaces and the Interactions in Colloidal Suspensions*, Pure and Applied Chem. **48**, 471 (1976).
- [45] J. C. Crocker, A. D. Dinsmore, J. A. Matteo, and A. G. Yodh, *Entropic Attraction and Repulsion in Binary Colloids Probed with a Line Optical Tweezer*, (to be published) .

- [46] P. Attard, *Spherically Inhomogeneous Fluids. II. Hard-sphere Solute in a Hard-sphere Solvent*, J. Chem. Phys. **91**, 3083 (1989).
- [47] P. Manoj, A. D. Watson, and D. H. et. al., *Characterization of a Depletion-Flocculated Polydisperse Emulsion II. Steady-state Rheological Investigations*, J. Colloid Interface Sci. **207**, 294 (1998).
- [48] J. Janzen and D. E. Brooks, *Do Plasma-Proteins Adsorb to Red-cells*, Clinical Hemorheology **9**, 695 (1989).
- [49] A. D. Dinsmore, D. T. Wong, P. Nelson, and A. G. Yodh, *Hard Spheres in Vesicles: Curvature-Induced Forces and Particle-Induced Curvature*, Phys. Rev. Lett. **80**, 409 (1998).
- [50] E. Evans and D. Needham, *Physical Properties of Surfactant Bilayer Membranes: Thermal Transitions, Elasticity, Rigidity, Cohesion, and Colloid Interactions*, J. Phys. Chem. **91**, 4219 (1987).
- [51] A. P. Chatterjee and K. S. Schweizer, *Correlation Effects in Dilute Particle-Polymer Mixtures*, J. Chem. Phys. **109**, 10477 (1998).
- [52] T. Odijk, *Depletion Around a Protein Sphere Interacting with a Semidilute Polymer Solution*, Langmuir **13**, 3579 (1997).

- [53] T. Odijk, *Many-body Depletion Interactions among Protein Spheres in a Semidilute Polymer Solution*, J. Chem. Phys. **106**, 3402 (1997).
- [54] H. M. Schaink and J. A. M. Smit, *Mean Field Calculation of Polymer Segment Depletion and Depletion Induced Demixing in Ternary Systems of Globular Proteins and Flexible Polymers in a Common Solvent*, J. Chem. Phys. **107**, 1004 (1997).
- [55] E. Eisenriegler, A. Hanke, and S. Dietrich, *Polymers Interacting with Spherical and Rodlike Particles*, Phys. Rev. E **54**, 1134 (1996).
- [56] P. G. de Gennes and R. Lucas, *Physique Statistique – Suspensions Colloïdales dans une Solution de Polymers*, C. R. Acad. Sc. Paris **288**, 359 (1979).
- [57] R. P. Sear, *Entropy-Driven Phase Separation in Mixtures of Small Colloidal Particles and Semidilute Polymers*, Phys. Rev. E **56**, 4463 (1997).
- [58] P. Richmond and M. Lal, *A Theoretical Treatment of Entropic Repulsions by Polymers*, Chem. Phys. Lett **24**, 594 (1974).
- [59] A. P. Chatterjee and K. S. Schweizer, *Microscopic Theory of Polymer-Mediated Interactions between Spherical Particles*, J. Chem. Phys. **109**, 10464 (1998).
- [60] E. J. Meijer and D. Frenkel, *Colloids Dispersed in Polymer Solutions. A Computer Simulation Study*, J. Chem. Phys. **100**, 6873 (1994).

- [61] Y. Mao, M. E. Cates, and H. N. W. Lekkerkerker, *Theory of the Depletion Force Due to Rodlike Polymers*, J. Chem. Phys. **106**, 3721 (1997).
- [62] M. Triantafillou and R. D. Kamien, *Polymer Shape Anisotropy and the Depletion Interaction*, (to be published) .
- [63] B. V. Derjaguin, *Friction and Adhesion. IV. The Theory of Adhesion of Small Particles*, Kolloid-Z Z. Polym. **69**, 155 (1934).
- [64] M. K. Georges, R. P. N. Veregin, and P. M. K. et. al., *Narrow Molecular-Weight Resins by a Free-Radical Polymerization Process*, Macromolecules **26**, 2987 (1993).
- [65] J. Rudnick and G. Caspari, *The Asphericity of r Random Walks*, J. Phys. A: Math. Gen. **19**, L191 (1986).
- [66] M. J. Snowden, S. M. Clegg, and P. A. Williams, *Flocculation of Silica Particles by Adsorbing and Non-adsorbing Polymers*, J. Chem. Soc. Faraday **17**, 1073 (1991).
- [67] A. D. Nikolov and D. T. Wasan, *Dispersion Stability due to Structural Contributions to the Particle Interaction as Probed by Thin Liquid-Film Dynamics*, Langmuir **8**, 2985 (1992).

- [68] J. Y. Walz, *Effect of Polydispersity on the Depletion Interaction between colloidal particles*, J. Colloid Interface Sci. **178**, 505 (1996).
- [69] Y. Mao, M. E. Cates, and H. N. W. Lekkerkerker, *Depletion Force in Colloidal Systems*, Physica A **222**, 10 (1995).
- [70] L. P. Faucheux and A. J. Libchaber, *Confined Brownian motion*, Phys. Rev. E **49**, 5158 (1994).
- [71] S. Inoue, *Video Microscopy* (Plenum Press, New York, 1986).
- [72] A. Ashkin, *Acceleration and Trapping of Particles by Radiation Pressure*, Phys. Rev. Lett. **24**, 156 (1970).
- [73] A. Ashkin, J. M. Dziedzic, J. E. Bjorkholm, and S. Chu, *Observation of a Single-beam Gradient Force Optical Trap for Dielectric Particles*, Opt. Lett. **11**, 288 (1986).
- [74] L. P. Faucheux, G. Stolovitzky, and A. J. Libchaber, *Periodic Forcing of a Brownian Particle*, Phys. Rev. E **51**, 5239 (1995).
- [75] H. He, N. R. Heckenberg, and H. Rubinsztein-Dunlop, *Optical Particle Trapping with Higher-order Doughnut Beams Produced Using High Efficiency Computer Generated Holograms.*, J. Mod. Opt. **42**, 217 (1995).

- [76] N. B. Simpson, L. Allen, and M. J. Padgett, *Optical Tweezers and Optical Spanners with Laguerre-Gaussian Modes*, J. Mod. Opt. **43**, 2485 (1996).
- [77] K. T. Gahagan and G. A. Swartzlander Jr., *Optical Vortex Trapping of Particles*, Opt. Lett. **21**, 827 (1996).
- [78] E. R. Lyons and G. J. Sonek, *Confinement and Bistability in a Tapered Hemispherically Lensed Optical Fiber Trap*, Appl. Phys. Lett. **66**, 584 (1995).
- [79] K. Svoboda and S. M. Block, *Biological Applications of Optical Forces*, Annu. Rev. Biophys. Biomol. Struct. **23**, 247 (1994).
- [80] D. Grier, *Optical Tweezers in Colloid and Interface Science*, Curr. Opinion in Colloid and Interface Science **2**, 264 (1997).
- [81] K. F. Ren, G. Gréhan, and G. Gouesbet, *Prediction of Reverse Radiation Pressure by Generalized Lorenz-Mie theory*, Appl. Opt. **35**, 2702 (1996).
- [82] T. Wohland, A. Rosin, and E. H. K. Stelzer, *Theoretical Determination of the Influence of the Polarization on Forces Exerted by Optical Tweezers*, Optik **102**, 181 (1996).
- [83] C. D'Helon, E. W. Dearden, N. R. Heckenberg, and H. Rubinsztein-Dunlop, *Measurement of the Optical Force and Trapping Range of a Single-beam Gradient Optical Trap for Micron-Sized Latex Spheres*, J. Mod. Opt. **41**, 595 (1994).

- [84] A. D. Dinsmore, *Entropic Attractions in Colloidal Solutions*, Ph.D. thesis, University of Pennsylvania, 1997.
- [85] J. Crocker and D. Grier, *Methods of Digital Video Microscopy for Colloidal Studies*, *J. Coll. Int. Sci.* **179**, 298 (1996).
- [86] T. T. Perkins, D. E. Smith, and S. Chu, *Direct Observation of Tube-Like Motion of a Single Polymer Chain*, *Science* **264**, 819 (1994).
- [87] S. Gurrieri, K. S. Wells, I. D. Johnson, and C. Bustamante, *Direct Visualization of Individual DNA Molecules by Fluorescence Microscopy: Characterization of the Factors Affecting Signal/Background and Optimization of Imaging Conditions Using YOYO*, *Analy. Biochem.* **279**, 44 (1997).
- [88] T. W. Houseal, C. Bustamante, R. F. Stump, and M. F. Maestre, *Real-time Imaging of Single DNA molecules with Fluorescence Microscopy*, *Biophys. J.* **56**, 507 (1989).
- [89] N. Pernodet and B. Tinland, *Dynamics of Colloid-Polymer Mixtures*, *Biopoly.* **42**, 705 (1997).
- [90] X. Ye, T. Narayanan, P. T. J. S. Huang, M. Y. Lin, B. L. Carvalho, and L. J. Fetters, *Depletion Interactions in Colloid-Polymer Mixtures*, *Phys. Rev. E* **54**, 6500 (1996).

- [91] T. G. Mason and D. A. Weitz, *Optical Measurements of Frequency-Dependent Linear Viscoelastic Moduli of Complex Fluids*, Phys. Rev. Lett. **74**, 1250 (1995).
- [92] C. N. Onyememezu, D. Gold, M. Roman, and W. G. Miller, *Diffusion of Polystyrene Latex Spheres in Linear Polystyrene Nonaqueous Solutions*, Macromolecules **26**, 3833 (1993).
- [93] P. Tong, X. Ye, B. J. Ackerson, and L. J. Fetters, *Transport of Probe Particles in Semidilute Polymer Solutions*, Macromolecules **31**, 5785 (1998).
- [94] E. C. Cooper, P. Johnson, and A. M. Donald, *Probe Diffusion in Polymer Solutions in the Dilute/Semi-dilute Crossover Regime: 1. Poly(ethylene oxide)*, Polymer **32**, 2815 (1991).
- [95] K. A. Streletzky and G. D. J. Phillies, *Translational Diffusion of Small and Large Mesoscopic Probes in Hydroxypropylcellulose-Water in the Solutionlike Regime*, J. Chem. Phys. **108**, 2975 (1998).
- [96] G. D. J. Phillies and D. Clomenil, *Probe Diffusion in Polymer Solutions under Θ and Good Conditions*, Macromolecules **26**, 167 (1993).
- [97] D. Langevin and F. Rondelez, *Sedimentation of Large Colloidal Particles through Semi-Dilute Polymer Solutions*, Polymer **19**, 875 (1978).

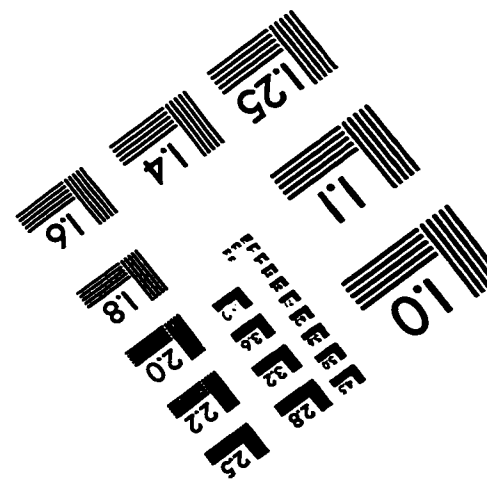
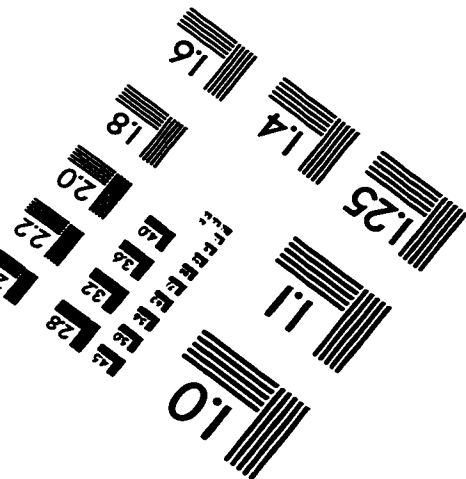
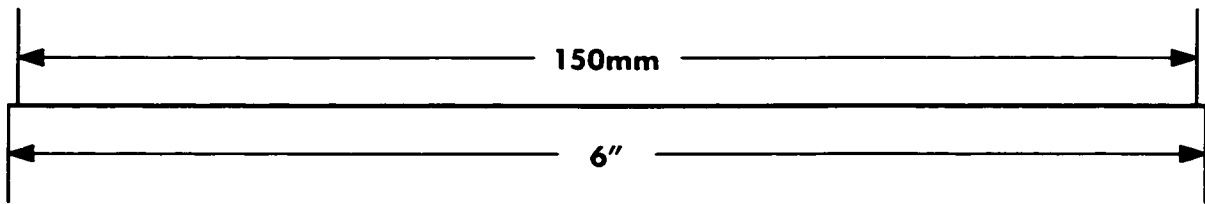
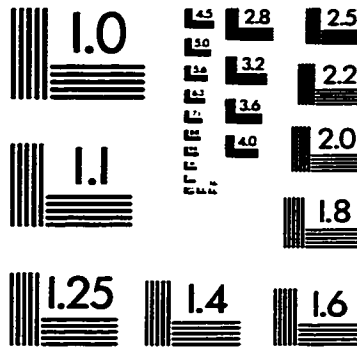
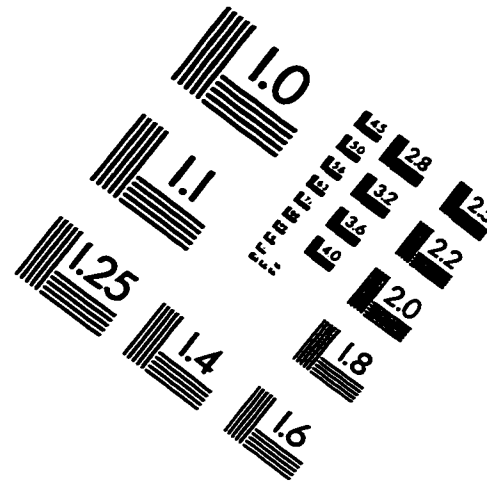
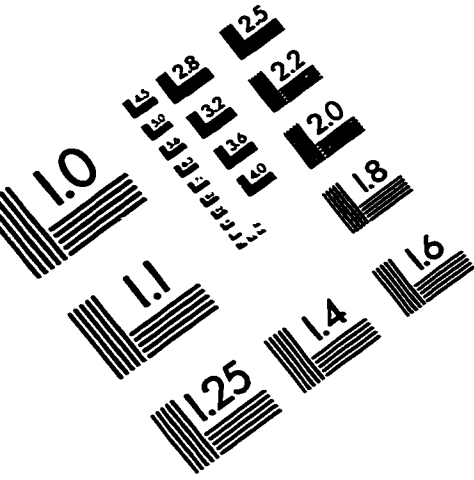
- [98] P. Tong, X. Ye, B. J. Ackerson, and L. J. Fetters, *Sedimentation of Colloidal Particles through a Polymer Solution*, Phys. Rev. Lett. **79**, 2363 (1997).
- [99] M. W. Evans, *Dynamical Processes in Condensed Matter* (John Wiley, New York, 1985).
- [100] D. E. Smith, T. T. Perkins, and S. Chu, *Self-Diffusion of an Entangled DNA Molecule by Reptation*, Phys. Rev. Lett. **75**, 4146 (1995).
- [101] M. Muthukumar and K. F. Freed, *Huggins Coefficient for Polymer Solutions with Excluded Volume*, Macromolecules **10**, 899 (1977).
- [102] G. K. Batchelor, *An Introduction to Fluid Dynamics* (Cambridge, New York, 1992).
- [103] G. K. Batchelor, *Brownian Diffusion of Particles with Hydrodynamic Interaction*, Journal of Fluid Mechanics **74**, 1 (1976).
- [104] J. C. Crocker, *Probing Colloidal Interactions with Digital Video Microscopy and Blinking Optical Tweezers*, Ph.D. thesis, University of Chicago, 1996.
- [105] M. Muthukumar and S. F. Edwards, *Screening Concepts in Polymer Solution Dynamics*, Polymer **23**, 345 (1982).
- [106] A. R. Altenberger, M. Tirrell, and J. S. Dahler, *Hydrodynamic Screening and*

Particle Dynamics in Porous Media, Semidilute Polymer Solutions and Polymer Gels, J. Chem. Phys. **84**, 5122 (1986).

[107] K. F. Freed and M. Muthukumar, *On the Stokes Problem for a Suspension of Spheres at Finite Concentrations*, J Chem. Phys. **68**, 2088 (1977).

[108] S. A. Adelman, *Hydrodynamic Screening and Viscous Drag at Infinite Concentration*, J. Chem. Phys. **68**, 49 (1978).

IMAGE EVALUATION TEST TARGET (QA-3)



APPLIED IMAGE, Inc
1653 East Main Street
Rochester, NY 14609 USA
Phone: 716/482-0300
Fax: 716/288-5989

© 1993, Applied Image, Inc., All Rights Reserved